Nanoscale topography and wear of ceramic interfaces and their effect on macroscale friction

Hsia, F.-C.

Publication date
2023

Document Version
Final published version

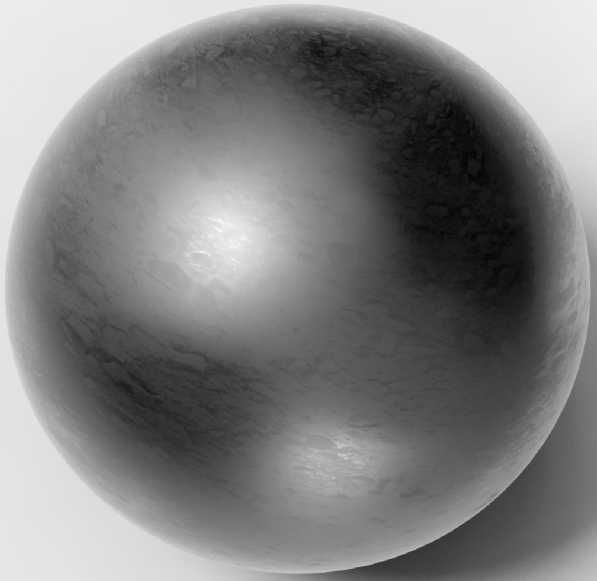

Nanoscale Topography and Wear of Ceramic Interfaces and their effect on Macroscale Friction Feng-Chun Hsia 2023

Nanoscale Topography and Wear of Ceramic Interfaces and their effect on Macroscale Friction

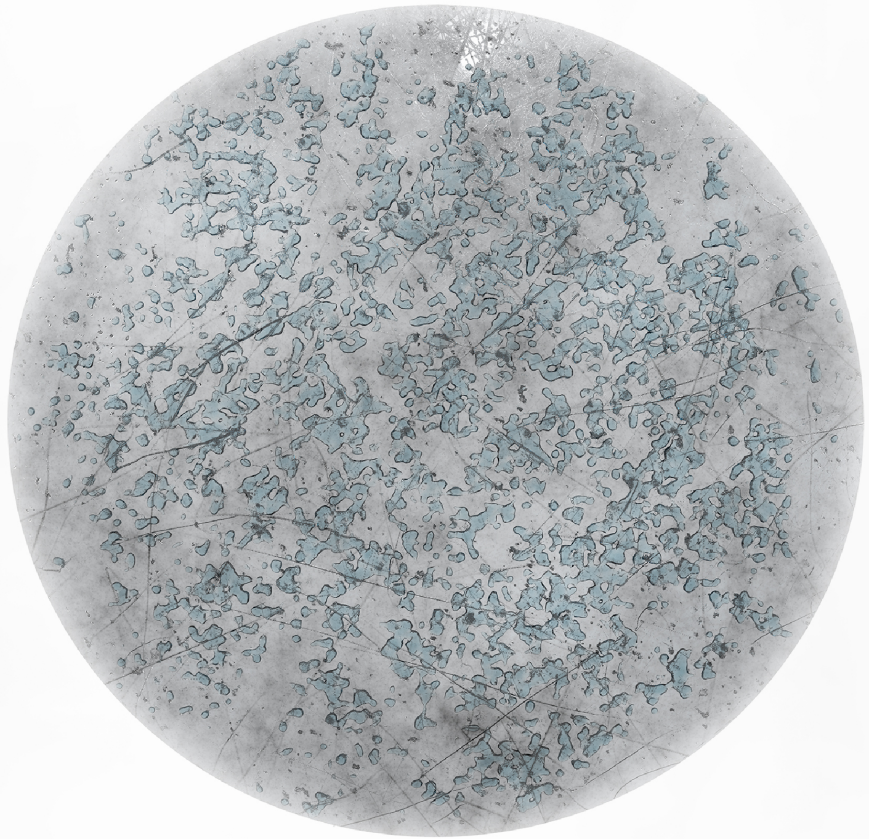

Feng-Chun Hsia

Nanoscale Topography and Wear of Ceramic Interfaces and their effect on Macroscale Friction

Feng-Chun Hsia

Nanoscale Topography and Wear of Ceramic Interfaces and their effect on Macroscale Friction

ACADEMISCH PROEFSCHRIFT

ter verkrijging van de graad van doctor
aan de Universiteit van Amsterdam
op gezag van de Rector Magnificus
prof. dr. ir. P.P.C.C. Verbeek
ten overstaan van een door het College voor Promoties ingestelde commissie,
in het openbaar te verdedigen in de Agnietenkapel
op vrijdag 6 oktober 2023, te 13.00 uur

door Feng-Chun Hsia
geboren te Taipei City

PROMOTIECOMMISSIE

Promotores:	prof. dr. D. Bonn	Universiteit van Amsterdam
	prof. dr. J.W.M. Frenken	Universiteit van Amsterdam
Copromotores:	dr. B.A. Weber	ARCNL
	prof. dr. S.E. Franklin	ARCNL
Overige leden:	prof. dr. M.B. de Rooij	University of Twente
	dr. S. Janssens	ASML
	prof. dr. A.M. Brouwer	Universiteit van Amsterdam
	prof. dr. N.F. Shahidzadeh	Universiteit van Amsterdam
	dr. R. Bliem	Universiteit van Amsterdam

Faculteit der Natuurwetenschappen, Wiskunde en Informatica


The work described in this thesis was carried out at the Advanced Research Center for Nanolithography (ARCNL), a public-private partnership between the University of Amsterdam (UvA), the Vrije Universiteit Amsterdam (VU), the Dutch Research Council (NWO) and the semiconductor equipment manufacturer ASML.

ISBN: 978-94-6419-884-3

Cover design: Henk-Jan Boluijt & Feng-Chun Hsia
Electronic version of this thesis can be found at `https://dare.uva.nl`

The author can be reached at: fengchunhsia@gmail.com

Contents

CHAPTER 1

Introduction

1.1 What makes friction important?

While walking in the rain, on a sandy road or while skating on ice, we can feel that surfaces are slippery and intuitively slow down our pace to prevent falling down. In winter, we rub our hands to get warmer. These behaviors suggest that we have naturally learned how to manage frictional forces to avoid injures in our everyday life. However, mastering friction does not merely help us to protect ourselves, it also improves the quality of our living environments and facilitates the development of technology. In the Middle Paleolithic around 2 million years ago, our ancestors were using friction to make fire [1]. The use of fire signifies a big step in human history.

Friction has also played a crucial role in advances in civil engineering. In ancient Egypt, Egyptians were pulling sledges to transport the huge stones for building pyramids as well as giant statues [2]. To slide their sledges more easily, the ancient Egyptians poured a lubricant in front of the sledge (Figure 1.1a): likely water to wet the sand and make the sledge-on-sand interface more slippery [3]. In the far East, ice was adopted as a lubricant to transport heavy objects for civil engineering purposes. For the construction of the Forbidden City, in 15^{th} century China, stones that weighed over a hundred tons were transported with a sliding sledge on an artificial ice path over a distance of 70 km (Figure 1.1b) [4]. While a team of men hauled the sledge with a huge stone on it, water was poured on the ice path to ease the sliding. Interestingly, the use of rotary wheels was already discovered by these ancient civilizations. For example, the war chariot in ancient Egypt or the south-pointing chariot in ancient China both made use of wheels for transport. However, the limited load capacity of the wheel made it unreliable for the transport of heavy objects. Nonetheless, the development and application of rotary objects, such as

wheels and bearings, nowadays makes transportation faster and smoother than ever before.

In many applications, such as the ones described above, the main goal is to minimize the friction that resists the relative motion of objects. Lubricants, wheels and bearings are widely used on bikes, motors and vehicles as well as in industrial applications, such as heavy equipment in construction and manufacturing and positioning systems. However, about 23% of the world's total energy consumption is used to overcome friction (20%) and to repair and replace components that have been worn as a result of friction (3%), as estimated by Holmberg and Erdemir in 2017 [5]. This large amount of energy consumption shows how great the impact of friction and wear on the economy and environment is. Up to 18–40% of the energy consumption due to friction and wear can be saved by implementing the latest advanced materials and engineering designs [6]. Better understanding and manipulation of friction are therefore crucial in improving our economy and environment.

(a)

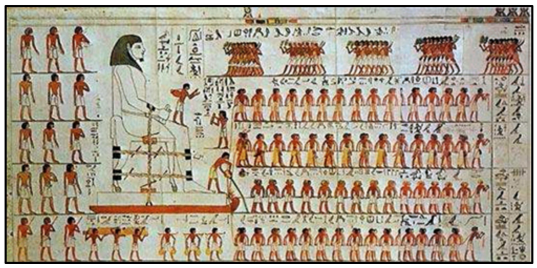

(b)

Figure 1.1: The transportation of giant stones in ancient civilizations. (a) The wall painting on the tomb of Djehutihotep illustrates that about 3900 years ago Ancient Egyptians poured water in front of moving sledges for the transport of giant statues. (image credit: El Bersheh: The tomb of Tehuti-Hetep [7]) (b) The Large Stone Carving is located between two paths of stone stairs towards the back side of the current Hall of Preserving Harmony (Baohe Dian). The Stone Carving, which is the heaviest stone ($\sim$300 tons when it was initially transported) in the Forbidden City, is designed as a path only for the emperor. (picture taken from The Palace Museum, `www.dpm.org.cn`)

1.2 Studies of sliding friction in relation to contact mechanics at macroscopic interfaces

1.2.1 Understanding friction

500 years ago, Leonardo da Vinci (1452–1519) designed a series of experiments to systematically investigate friction. In da Vinci's experiments, wooden blocks of different sizes were pulled in various orientations over a horizontal plane using a string (Figure 1.2). In his notebook, da Vinci stated 'la confregazione si fa di duplicate fatica induplicato peso': the friction is doubled by doubling the weight, and the area of apparent contact shows no influence on friction. The material hardness and surface roughness were included as variables in da Vinci's sliding experiments. da Vinci observed that the resistance against sliding movement is greater when the sliding surfaces are hard and rough but lower when the surfaces are rough and soft. In later studies, da Vinci mentioned that smoother surfaces generate less friction. The observations from Leonardo da Vinci were later confirmed by the French physicist Guillaume Amontons (1663–1705). Amontons designed a flat-on-flat sliding experiment and used two springs, connected to the sliding specimen, to maintain the contact pressure and to measure the force in the tangential direction: the frictional force. In Amontons' experiments, the sliders were made of different sizes and with different materials (including copper, iron, lead and wood) and covered with pork fat as a lubricant. Amontons rediscovered similar friction behavior as da Vinci and his findings are referred to as the first and the second laws of Amontons:

Amontons' first law:
The frictional force is proportional to the normal load.

Amontons' second law:
The frictional force is independent of the area of apparent contact.

Amontons' first law can simply be expressed as:

$$F_{\mathrm{n}} = \mu F_{\mathrm{f}} \tag{1.1}$$

where F_{f} and F_{n} are the frictional and normal force, respectively, and μ is the coefficient of friction. Equation (1.1) implies that the frictional force is independent of the area of apparent contact, which is described by Amontons' second law.

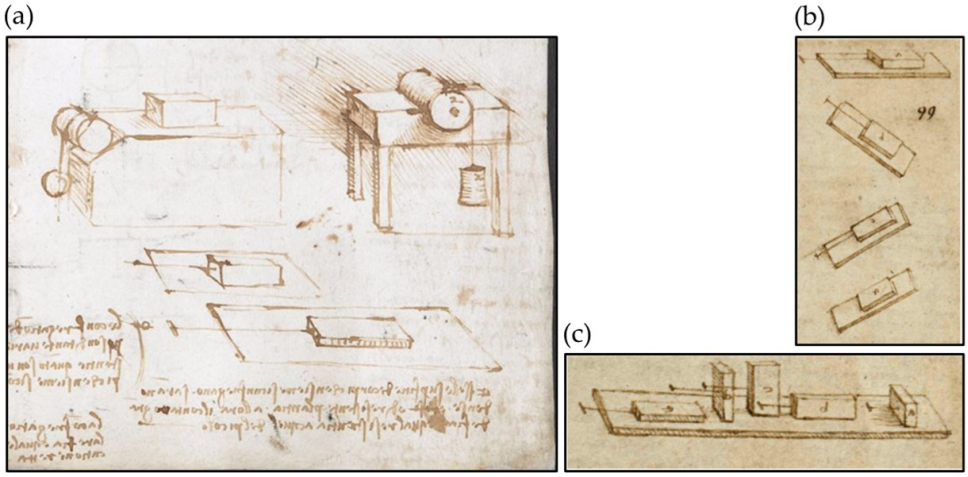

Figure 1.2: Sketches of the friction experiments in Leonardo da Vinci's notebooks: (a) from Codex Arundel, on the bottom, shows different sizes of wooden blocks sliding on a horizontal plane (image taken from the British Library in London `www.journal.sciencemuseum.ac.uk/`), and (b, c) from Codex Atlanticus, show that friction is measured by dragging blocks on a plane with various inclinations or blocks placed in different orientation on a horizontal plane. (images taken from the Biblioteca Ambrosiana in Milan `www.ambrosiana.it`)

Eighty years later, another French physicist, Charles-Augustin Coulomb (1736–1806) carried out more detailed sliding experiments to measure friction and systematically considered various factors, such as sliding velocity, normal load, material elasticity, surface condition (e.g., rough and smooth), area of apparent contact and environmental conditions. He confirmed Amontons' findings and also investigated the relation between frictional force and sliding velocity observing that the kinetic (or dynamic) frictional force shows a relatively weak dependence on sliding velocity. This observation of the relation between kinetic frictional force and sliding velocity is referred to as:

Coulomb's law:
Kinetic friction is independent of sliding velocity.

Amontons' and Coulomb's laws of friction are often summarized as the "laws of dry friction".

Although the findings from Amontons and Coulomb describe the frictional behavior at most dry interfaces, the laws of friction are empirical. In the 20^{th} century,

Australian physicist Frank Philip Bowden (1903–1968) together with British physicist David Tabor (1913–2005) provided mechanical insight into the origin of friction. They presented a theory in which the force required to shear the junctions that form between two metals in contact is:

$$F_{\mathrm{f}} = \tau A_{\mathrm{real}} \tag{1.2}$$

where F_{f} is the adhesive frictional force, τ is the shear strength of the junctions and $A_{\mathrm{real}} (= \sum A_i)$ is the area of real contact: the sum of the contact areas of each junction (A_i) across the interface. The load (F_{n}) applied to the contacting bodies is supported by an area of real contact large enough to prevent the normal stress (σ) from leading to further plastic flow of the contacting materials:

$$F_{\mathrm{n}} = \sigma A_{\mathrm{real}} \tag{1.3}$$

By combining Equation (1.2) and (1.3), the ratio of adhesive frictional force to normal force–the coefficient of friction–is the ratio of the shear strength to the hardness [8]:

$$\mu = \frac{F_{\mathrm{f}}}{F_{\mathrm{n}}} = \frac{\tau}{\sigma} \tag{1.4}$$

Bowden and Tabor expected that the theory also holds for non-metallic contacts. However, the picture sketched by Bowden and Tabor suggests that the adhesive frictional force depends on the area of contact, which contradicts Amontons' second law. This leads to the question of how the frictional force depends on the area of contact. Bowden and Tabor designed an experiment in which they measured the electrical conductance across the interface between two crossed metal cylinders at different applied loads [9]. The underlying assumption was that the conductivity is controlled by the area of contact between the two metal surfaces. Bowden and Tabor showed that the measured electrical conductance increases linearly with applied load. If the surfaces in contact were smooth and deformed elastically, the conductance and the area of real contact were expected to increase with applied load to the power two-thirds. Bowden and Tabor explained that the interface between the metal surfaces consisted of many contact junctions due to the roughness of the surfaces. The contact junctions–or contacting asperities–are primarily plastically deformed. Therefore, the area of real contact is proportional to the applied load, the proportionality constant being the material hardness. John Frederick Archard (1918–1989), a British engineer, proposed a simple multiple-contacts model in which the number of contacts and the area of these contacts between the surfaces increased linearly with applied load [10]. When the contacts are plastically deformed, both

the number of contacts ($N \propto F_n$) and the area of these contacts ($A_{real} \propto F_n$) are proportional to the applied load (F_n).

The relation between friction and area of contact according to Amontons' first law, on the one hand, suggests that the constant of proportionality between frictional force and normal force (Equation (1.1)) can exist as long as the ratio of interfacial shear stress to interfacial normal stress remains constant, not necessarily requiring the interfacial shear stress to be a constant. On the other hand, the Bowden and Tabor picture of adhesive friction (Equation (1.2)) implies that the shear force required to shear the contact junctions is not dependent on the applied load but depends on the area of real contact. The interfacial shear stress is then either set, at any one moment in time, by the shear strength of the softest material, by the adhesion strength of the interfacial junctions or by a combination of the two. This suggests that the interplay between frictional force, normal force and the area of real contact remains unclear. In the late 20th century, scientists proposed that the frictional force can be described as the sum of two terms [11, 12]; load-controlled friction ($F_f = \mu F_n$) and adhesion-controlled friction ($F_f = \tau A_{real}$):

$$F_f = \mu F_n + \tau A_{real} \tag{1.5}$$

In the case of load-controlled friction, the interfacial shear stress increases linearly with the interfacial normal stress: more normal stress leads to more atomic scale interlocking. Thus, the frictional force is independent of the area of contact. In the case of adhesion-controlled friction, the interfacial shear stress is set by the adhesive force of the intermolecular bonds formed across the interface. The adhesion and thus interfacial shear stress are largely unaffected by normal stress. The area of real contact quantifies the total amount of adhesion experienced. Therefore, the adhesive frictional force is proportional to the area of real contact. The two types of friction, load-controlled and adhesion-controlled, are illustrated in Figure 1.3 [11]. The sum of the load-controlled and adhesion-controlled terms suggests that if the surfaces weakly adhere to each other or the interface is under high applied load, the first term (load-controlled friction) dominates over the second term (adhesion-controlled friction), while at interfaces with strong adhesion the second term dominates over the first term.

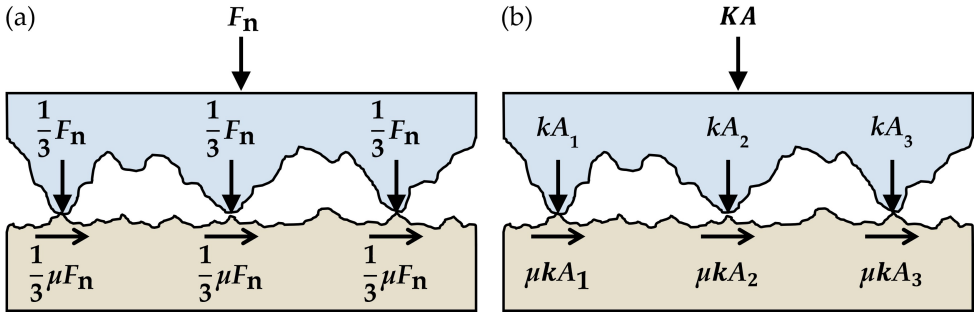

Figure 1.3: Schematic illustration of the load-controlled friction (a) and the adhesion-controlled friction (b). In the load-controlled case (a), the normal load (F_n) is equally distributed to three contact junctions, and the degree of atomic scale interlocking at each contact junction is equally divided: $F_f = \mu F_n = \frac{1}{3}\mu F_n + \frac{1}{3}\mu F_n + \frac{1}{3}\mu F_n$ indicating that friction is independent of the area of contact. In the adhesion-controlled case (b), the intermolecular bonding strength (k) exerted over the cross-sectional area of the contact junction (A) acts as the effective ''internal" load. The total normal force for three contact junctions is $F_n = kA_1 + kA_2 + kA_3$, and the frictional force is $F_f = \mu F_n = \mu k(A_1 + A_2 + A_3)$, which implies that the frictional force is dependent to the area of real contact. (figure reproduced from [11])

1.2.2 The area of real contact between rough surfaces

In the 1930s, Bowden and Tabor measured the electrical conductance between curved metal surfaces at different applied loads [9]. They experimentally and theoretically demonstrated that the area of real contact reflected by the conductance-load curve can be fitted by a plastic contact model derived from the Hertzian theory of contact [13]. They highlighted that the area of real contact is the total cross-sectional area of contact junctions which form between local asperity summits on the surfaces to support the applied load. However, at that moment, Bowden and Tabor could not quantify the number of contact junctions between two surfaces. Nonetheless, they found that the area of real contact is only a small fraction of the area of apparent contact and proportional to the applied load due to plastic deformation.

Two decades later, J. A. Greenwood and J. B. P. Williamson [14] developed an analytical model to describe the contact formation between an elastically deformable rough surface and a rigid flat surface. In the model, there is no adhesion between the surfaces and the height of the asperity summits follows either a Gaussian or an exponential distribution. The apex of each asperity is spherical and has a fixed

radius of curvature. The deformation of each asperity follows the Hertzian theory of contact. In the Greenwood and Williamson (GW) model, the area of real contact is proportional to the applied load ($A_{\text{real}} \propto F_{\text{n}}$), even though an individual Hertzian sphere-on-flat contact follows a sublinear relation between area of contact and applied load ($A_{\text{real}} \propto F_{\text{n}}^{\frac{2}{3}}$). Although the GW model can be considered as the benchmark of multi-asperity contact theories, the model has several shortcomings [15, 16]: (1) the radius of curvature is not well-defined for asperities on real surfaces; (2) the Gaussian distribution of asperity heights is not found on many surfaces; (3) the model breaks down when the area of real contact becomes a significant fraction of the area of apparent contact (higher than 0.01%); (4) the model ignores the interaction between asperities.

To address these limitations, Persson developed an alternative contact theory that incorporates plasticity and considers rough-on-rough contact geometries [17]. In Persson's contact theory, self-affine fractal surfaces are considered and described using the power spectral density. This enables Persson theory to address roughness on various length scales–asperities on top of asperity–and the coupling between these length scales. Although Persson's contact theory and the GW model both predict the area of real contact to be proportional to the normal load, Persson's theory has been shown to be more accurate, especially at higher normal loads [18]. In more recent studies, long-range and short-range adhesive forces, such as capillary adhesion, van der Waals forces and viscoelastic energy dissipation, have been incorporated into Persson's model [19, 20, 21, 22].

1.3 Sliding in vapor environments: the effect of capillary condensation at the interfaces

Animals, such as geckos and bees, are able to climb vertically on a variety of surfaces. This fascinating ability to walk vertically is made possible by (capillary) adhesion exerted at the interface between the feet of these animals and the surfaces they walk on. Surprisingly, the feet of animals that can walk vertically are typically small compared to the body size [23, 24].

To explain the origin of capillary adhesion, we consider a water droplet as an example. When a droplet of water is placed on a flat glass surface, the water droplet naturally takes on a spherical shape. The water molecules on the droplet surface are attracted by neighboring water molecules in the bulk while no attraction is

experienced from the other side–the water-air interface–to balance the attractive cohesive force (Figure 1.3). Hence, the uneven force balance exerted on the surface water molecules creates a tension force–the surface tension–that acts to minimize the water-air interfacial area. The thermodynamic definition of the surface tension indicates that the surface tension (γ) is the work (W) per unit area (A) that needs to be performed against the cohesive forces to pull liquid molecules from the bulk to the surface: $\gamma = \frac{dW}{dA}$. At positively curved water surfaces, minimization of the water-air interfacial area leads to a buildup of pressure inside the droplet. Similarly, the pressure is decreased inside a negatively curved water surface [16]. If a small amount of liquid water, such as the absorbed layer of vapor water on the surface, is present between two contacting or nearly contacting hydrophilic surfaces, the liquid water forms a meniscus–capillary bridge–that has a certain degree of curvature due to surface tension, and generates a capillary pressure or Laplace pressure. A capillary pressure force (or capillary adhesion, F_c) originates from the capillary pressure (P_{cap}) exerted over the area (A_{cap}) wetted by the meniscus that tends to pull two surfaces together: $F_c = P_{cap} \times A_{cap}$. The effect of capillary adhesion in the out-of-plane direction can lead to variance in the tangential force–frictional force–in the in-plane direction. The relation between frictional force and normal force (Equation (1.1)) implies that the capillary adhesive force (F_c) in the normal direction leads to an increase in the frictional force (F_f) in the tangential direction: $F_f = \mu(F_n + F_c)$. The capillary adhesion can be driven by water layers present at free surfaces, however, through capillary condensation additional water can be attracted to interfaces; this is a complex subject especially at sliding interfaces that are not in thermodynamic equilibrium. Parameters such as temperature, relative humidity, surface chemistry, liquid surface tension, viscosity and sliding speed are known to play an important role in capillary adhesion [25, 26, 27, 28, 29, 30].

1.4 A glimpse of this thesis

In this thesis, we investigate the interplay between friction, surface topography, capillary adhesion and third body formation at macroscopic sliding interfaces between ceramic materials. In **Chapter 2**, we describe the experimental techniques and numerical methods that were applied in the research described in **Chapters 3 to 6**. Two types of setups to measure frictional force and methods for the characterization of surface topography before and after sliding are introduced. A fluorescence microscopy-based technique for measurement of the area of real contact at macro-

scopic interfaces is introduced as well as a numerical method for rough surface contact calculations.

In **Chapter 3**, we discuss the impact of third body formation at the contact interface on friction behavior. We perform two different kinds of sliding experiments–repeated and non-repeated reciprocated sliding–and compare the friction and wear behavior of various brittle non-metallic balls on Si wafer surfaces. We observe a general trend in the friction behavior in repeated sliding experiments: after running-in, friction is low and more stable than when sliding in a non-repeated fashion. The mechanisms underlying the running-in behavior are discussed in **Chapter 4**. Through *ex situ* microscopy we show that the formation of a third body at the interface is promoted during repeated sliding and the third body acts as a solid lubricant that stabilizes and reduces the friction. In non-repeated sliding, third body formation is much less evident and friction is increasing with the sliding distance. Moreover, through *in situ* visualization of the interface during sliding experiments, we directly observe the third body formation in repeated sliding but not in non-repeated sliding. To understand the nature of the increase in friction with sliding distance in non-repeated sliding, we measure the width of the wear tracks on the Si wafer and convert this to the size of the area of apparent contact between the ball and the wafer. We find that the growth of the area of apparent contact closely tracks the increase of the frictional force. The continuous increase of the area of apparent contact and friction suggests that the adhesive force at the interface provides an extra normal force which leads to the increase of the frictional force. We propose that at nanometrically smooth sliding interfaces capillary bridges form, thereby pulling the surfaces into closer contact and increasing the friction. A more detailed investigation into the interplay between friction, contact mechanics, surface topography and capillary adhesion is discussed in **Chapters 5 and 6**.

In **Chapter 4**, we discuss the mechanisms of running-in behavior at a SiC ball-on-Si wafer interface. We perform unidirectional sliding experiments to minimize the formation of third bodies at the interfaces. A clear running-in behavior is observed and the surface topography of the SiC ball and Si wafer are characterized before and after sliding. Relatively high friction is measured at the onset of sliding and the friction gradually decreases and stabilizes as the sliding distance increases. We clearly observe ploughing tracks within the initial parts of the wear track on the Si wafer. The effect of ploughing is suppressed as the sliding distance increases. The height profiles measured on the SiC ball show that the high roughness peaks on the ball surface are removed after sliding. Contact calculations based on the elasto-plastic boundary element method (BEM) enable us to track the corresponding

roughness peaks on the SiC ball that plastically deform the Si wafer during contact and lead to ploughing on the wafer at the asperity-level. We conclude that the friction at the onset of sliding is dominated by ploughing, while as the sliding distance increases the high peaks on the SiC surface are gradually removed and the effect of ploughing decreases leading to a reduction of friction.

In **Chapter 5**, we investigate the interplay between capillary adhesion, surface topography and friction at multi-asperity interfaces. We systematically manipulate the surface topography of Si_3N_4 balls and subsequently bring the Si_3N_4 balls into contact with a sapphire wafer. We experimentally measure the area of real contact using a fluorescence microscopy-based contact visualization technique and find a good agreement with the area of real contact calculated using BEM contact calculations. We find that even when the area of real contact is varied by a factor of 4 through manipulation of the surface topography, the coefficient of friction (CoF), which is the proportionality constant between the frictional force and normal force, shows a variation of only $\sim$20% in ambient environments. This variation in CoF as a function of surface topography is absent when the sliding experiments are performed with the contact immersed in water. We attribute the change of the CoF with surface topography to capillary adhesion across 'non-contact' areas at the interfaces: more capillary bridges form at the interface with lower surface roughness. We quantify the capillary adhesion through a combination of BEM contact calculations and the Laplace pressure estimated based on the Kelvin equation. Our capillary adhesion model without adjustable parameters captures the roughness dependent effect of capillary adhesion on friction.

In **Chapter 6**, we manipulate the effect of capillary adhesion on friction by controlling the surface tension of the liquid at the interface. In this Chapter, we focus on Si-on-Si interfaces, which are common in micro- and nano-electromechanical systems (MEMS and NEMS) and semiconductor devices. We quantify capillary adhesion experimentally and theoretically, and characterize the critical distance at which a single capillary bridge can nucleate at a nanoscale Si-on-Si interface in an ambient environment. We repeat similar adhesion measurements at larger Si-on-Si contacts and find that the capillary adhesion exerted at loaded multi-asperity interfaces cannot be detected due to the elastic deformation of the asperities at the interface, this is known as the adhesion paradox [31]. We employ the capillary adhesion model introduced in **Chapter 5** to calculate the capillary adhesion at the loaded interface and find agreement with the capillary adhesion inferred from the difference in frictional force measured in ambient and water immersed conditions. We numerically and experimentally demonstrate that the surface topography has a

great impact on the capillary adhesion at multi-asperity interfaces: smooth surfaces exert larger capillary adhesion than rough surfaces. The observed effect of surface topography on capillary adhesion and friction behavior is in agreement with the results from **Chapter 5**. By replacing water with isopropanol (IPA), we find that the capillary adhesion is decreased due to the lower surface tension of isopropanol. Furthermore, we observe that the friction is lower in IPA immersed conditions than in water immersed conditions, both in the absence of capillary adhesion. This indicates that the friction behavior of the Si-on-Si interfaces is not only controlled by capillary effects but also by boundary lubrication. IPA boundary layers on the Si surfaces lubricate the Si-on-Si interfaces and reduce the friction.

Bibliography

[1] Wil Roebroeks and Paola Villa. On the earliest evidence for habitual use of fire in europe. *Proceedings of the National Academy of Sciences*, 108(13):5209–5214, 2011.

[2] Robert F. Heizer. Ancient heavy transport, methods and achievements. *Science*, 153(3738):821–830, 1966.

[3] Jorge E Fiscina and Christian Wagner. Wet sand flows better than dry sand. *arXiv preprint arXiv:0711.2972*, 2007.

[4] Jiang Li, Haosheng Chen, and Howard A Stone. Ice lubrication for moving heavy stones to the forbidden city in 15th-and 16th-century china. *Proceedings of the National Academy of Sciences*, 110(50):20023–20027, 2013.

[5] Kenneth Holmberg and Ali Erdemir. Influence of tribology on global energy consumption, costs and emissions. *Friction*, 5(3):263–284, 2017.

[6] Kenneth Holmberg and Ali Erdemir. The impact of tribology on energy use and co2 emission globally and in combustion engine and electric cars. *Tribology International*, 135:389–396, 2019.

[7] Percy E Newberry. *The Tomb of Tehuti-Hetep*. Offices of the Egypt Exploration Fund, 1894.

[8] FP Bowden and D Tabor. Mechanism of metallic friction. *Nature*, 150(3798):197–199, 1942.

[9] Frank Philip Bowden and L Leben. The nature of sliding and the analysis of friction. *Proceedings of the Royal Society of London. Series A. Mathematical and Physical Sciences*, 169(938):371–391, 1939.

[10] JeFoa Archard. Contact and rubbing of flat surfaces. *Journal of applied physics*, 24(8):981–988, 1953.

[11] Alan Berman, Carlos Drummond, and Jacob Israelachvili. Amontons' law at the molecular level. *Tribology letters*, 4(2):95–101, 1998.

[12] Gang He, Martin H Müser, and Mark O Robbins. Adsorbed layers and the origin of static friction. *Science*, 284(5420):1650–1652, 1999.

[13] Heinrich Hertz. *Ueber die Berührung fester elastischer Körper*. De Gruyter, 2021.

[14] James A Greenwood and JB Pl Williamson. Contact of nominally flat surfaces. *Proceedings of the royal society of London. Series A. Mathematical and physical sciences*, 295(1442):300–319, 1966.

[15] JA Greenwood and JJ Wu. Surface roughness and contact: an apology. *Meccanica*, 36(6):617–630, 2001.

[16] C Mathew Mate and Robert W Carpick. *Tribology on the small scale: a modern textbook on friction, lubrication, and wear*. Oxford University Press, USA, 2019.

[17] Bo NJ Persson. Theory of rubber friction and contact mechanics. *The Journal of Chemical Physics*, 115(8):3840–3861, 2001.

[18] G Carbone and F Bottiglione. Contact mechanics of rough surfaces: a comparison between theories. *Meccanica*, 46(3):557–565, 2011.

[19] BNJ Persson. Adhesion between an elastic body and a randomly rough hard surface. *The European Physical Journal E*, 8(4):385–401, 2002.

[20] BNJ Persson. Capillary adhesion between elastic solids with randomly rough surfaces. *Journal of Physics: Condensed Matter*, 20(31):315007, 2008.

[21] Lars Pastewka and Mark O Robbins. Contact between rough surfaces and a criterion for macroscopic adhesion. *Proceedings of the National Academy of Sciences*, 111(9):3298–3303, 2014.

[22] B Lorenz, BA Krick, N Mulakaluri, M Smolyakova, S Dieluweit, WG Sawyer, and BNJ Persson. Adhesion: role of bulk viscoelasticity and surface roughness. *Journal of Physics: Condensed Matter*, 25(22):225004, 2013.

[23] Gerrit Huber, Hubert Mantz, Ralph Spolenak, Klaus Mecke, Karin Jacobs, Stanislav N Gorb, and Eduard Arzt. Evidence for capillarity contributions to gecko adhesion from single spatula nanomechanical measurements. *Proceedings of the National Academy of Sciences*, 102(45):16293–16296, 2005.

[24] Sophie Gernay, Walter Federle, Pierre Lambert, and Tristan Gilet. Elasto-capillarity in insect fibrillar adhesion. *Journal of The Royal Society Interface*, 13(121):20160371, 2016.

[25] Elisa Riedo, Francis Lévy, and Harald Brune. Kinetics of capillary condensation in nanoscopic sliding friction. *Physical review letters*, 88(18):185505, 2002.

[26] RC Major, JE Houston, MJ McGrath, JI Siepmann, and X-Y Zhu. Viscous water meniscus under nanoconfinement. *Physical review letters*, 96(17):177803, 2006.

[27] Christian Greiner, Jonathan R Felts, Zhenting Dai, William P King, and Robert W Carpick. Controlling nanoscale friction through the competition between capillary adsorption and thermally activated sliding. *ACS nano*, 6(5):4305–4313, 2012.

[28] Lei Chen, Chen Xiao, Bingjun Yu, Seong H Kim, and Linmao Qian. What governs friction of silicon oxide in humid environment: contact area between solids, water meniscus around the contact, or water layer structure? *Langmuir*, 33(38):9673–9679, 2017.

[29] Seongsoo Kim, Dohyun Kim, Jongwoo Kim, Sangmin An, and Wonho Jhe. Direct evidence for curvature-dependent surface tension in capillary condensation: Kelvin equation at molecular scale. *Physical Review X*, 8(4):041046, 2018.

[30] Kathryn Hasz, Zhijiang Ye, Ashlie Martini, and Robert W Carpick. Experiments and simulations of the humidity dependence of friction between nanoasperities and graphite: The role of interfacial contact quality. *Physical Review Materials*, 2(12):126001, 2018.

[31] A Tiwari, J Wang, and BNJ Persson. Adhesion paradox: Why adhesion is usually not observed for macroscopic solids. *Physical Review E*, 102(4):042803, 2020.

CHAPTER 2

Experimental techniques and numerical methods

In this Chapter we introduce the experimental techniques and numerical methods that are applied in **Chapters 3 to 6**. To understand the friction behavior under various environmental and experimental conditions, frictional force measurements are indispensable. Two different kinds of setups to measure the frictional force are introduced in this Chapter: a Universal Mechanical Tester (UMT) used in **Chapters 3 and 4** and a rheometer-based customized setup employed in **Chapters 3, 5 and 6**. The influence of surface topography on friction, through contact mechanics or wear debris on contacting bodies, is characterized through topography measurements conducted before and after sliding. We briefly illustrate how microscopy techniques are employed to characterize surface morphology at different length scales. Surface characterization is frequently conducted before and after sliding in **Chapters 3 to 6**. Furthermore, a direct observation method with which the area of real contact at the contact interface is visualized *in situ* in **Chapter 5** is described. Finally, we introduce a numerical method for the quantification of contact mechanics at ball-on-flat contact interfaces that is applied in **Chapters 3 to 6**.

2.1 Macroscopic friction measurements

In the frictional force measurements, a millimeter sized sphere is slid against a flat surface while a load is applied. While the sphere is sliding over the flat counter surface, the force that resists the sliding is defined as the frictional force. Below we introduce two types of experimental setups that perform sliding experiments and measure the normal and frictional force at the interface: a commercially available mechanical tester and a rheometer-based customized setup.

2.1.1 Friction measurements with a Universal Mechanical Tester (UMT)

Sphere-on-flat friction experiments are performed using a commercial Universal Mechanical Tester (UMT TriboLab, Bruker). As illustrated in Figure 2.1, a sphere is mounted on a sphere holder connected to a force sensor via a rigid adapter. The DFM-0.5G sensor (Bruker) is used to measure the normal and frictional forces ranging between 0.05–5 N with a resolution 0.25 mN. To perform the sliding, the force sensor is mounted on a positioning system, which conducts linear sliding motion in lateral and vertical directions with sliding speeds between 0.002–10 mm/s, and the positioning resolutions of the system are 0.25 μm and 0.5 μm in the lateral and vertical directions, respectively. Figure 2.2 demonstrates an example of a 3 mm SiC sphere sliding on a 10 mm diameter Si wafer surface at 100 mN applied load.

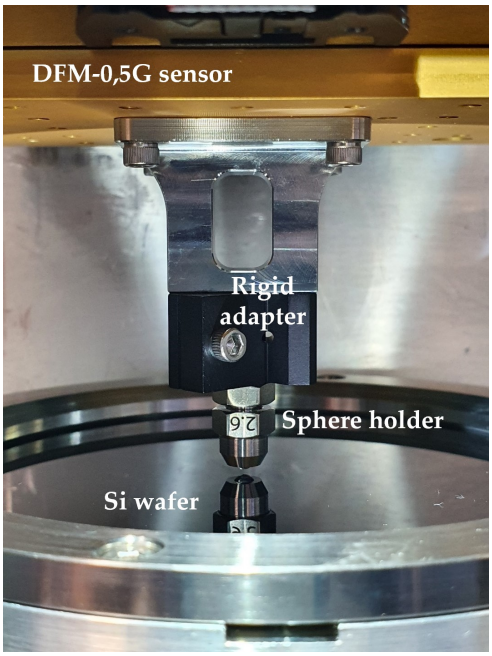

Figure 2.1: A picture of the sphere-on-flat sliding experiment performed by the Universal Mechanical Tester (UMT). A 3 mm SiC sphere is mounted on the sphere holder and indirectly connects to a force sensor via a rigid adapter. The sphere slides over a 100 mm diameter Si wafer fixed on the UMT.

2.1.2 Friction measurements with a rheometer

A commercial dynamic shear rheometer (DSR 301, Anton Paar) is customized to perform circular friction measurements. A schematic description of the setup is shown in Figure 2.3 where a rigid adapter connects the rheometer's geometry and converts the rotational motion of the rheometer to a circular sliding motion. In the sphere-on-flat friction experiments, the rheometer imposes a constant rotational speed driving the circular sliding of a sphere–that is mounted using the adapter–on a flat sample surface. Figure 2.4 demonstrates the frictional force measured at different normal forces in two opposite rotational directions. Friction measurements are performed in both directions to correct for the tilting of the rheometer with respect to the flat substrate.

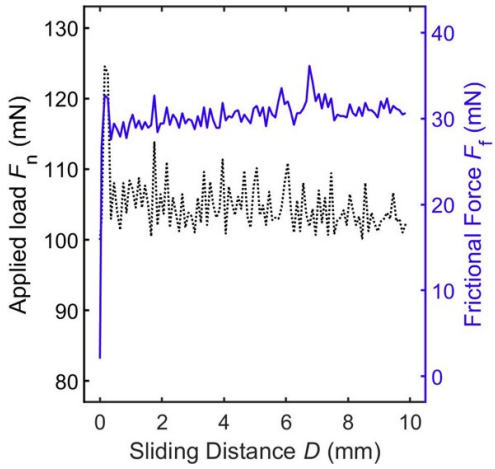

Figure 2.2: The normal and frictional force measured by the Universal Mechanical Tester (UMT) in a SiC sphere-on-Si flat sliding experiment. During sliding, the applied load (F_n) on the sphere is maintained at 100 mN by a rapid feedback loop (black dotted line) and the sliding speed is 0.5 mm/s. The frictional force (blue solid line) is measured parallel to the sliding (lateral) direction. A steep increase of the friction at the onset of sliding within static friction regime indicates the stiffness of the sliding system in the lateral direction, ∼470 N/m.

2.2 Surface Characterization

In **Chapter 1**, we discussed the impact of contact mechanics on friction. One of the important parameters to determine contact mechanics is the surface topography of the contacting bodies. For example, friction often leads to changes in surface topography during sliding, and wear debris as the result of friction can additionally influence the friction. To quantify contact mechanics and to analyze the effect of wear debris, we measure the surface topography of contacting bodies before and after friction experiments. Depending on the objective of the research, we employ two types of imaging techniques to capture the surface topography: atomic force microscopy (AFM) and 3D laser scanning confocal microscopy. The main difference between the two techniques is the resolution: AFM can reveal the smallest features on the surface.

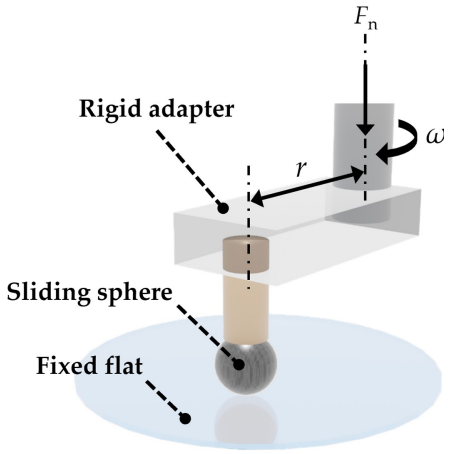

Figure 2.3: A schematic illustration of the frictional force measurement with a customized rheometer-based setup. In the friction experiments, a constant sliding speed is maintained by the rheometer via a stress-controlled feedback loop. The rheometer measures the resistance torque (M) and normal force (F_n) at a constant angular velocity (ω). By knowing the distance (r) between the adapter and the rheometer's geometry, the frictional force (F_f) is calculated as $F_f = \frac{M}{r}$ and the linear sliding speed (v) in the tangent direction of the circular motion is calculated as $v = \omega \times r$.

2.2.1 Atomic force microscopy (AFM)

To investigate the relation between surface topography, capillary adhesion and friction behavior in more detail, we use an atomic force microscope (Dimension Icon, Bruker) to measure the surface profile of the samples before and after friction experiments. The smallest features on the surface that can be resolved by the AFM is set by the size of the AFM tip apex, typical at the range of tens of nanometer. The surface topographies measured by AFM were used to perform contact mechanics calculations to quantify the geometry of the loaded multi-asperity interface in **Chapters 4–6**. In the Tapping mode AFM measurements (Figure 2.5), a nanometrically sharp AFM tip is mounted on one side of the microscopically sized cantilever, and the other side of the cantilever is clamped on the AFM holder that induces oscillation of the cantilever near its resonance frequency at a constant oscillation amplitude. When the oscillating AFM tip interacts with the sample surface, the tip-sample interaction changes the oscillation amplitude. A laser that is reflected off the back side of the cantilever is used to monitor changes in the oscillation amplitude. Such changes in oscillation amplitude trigger the feedback loop to lift or lower the cantilever to maintain a

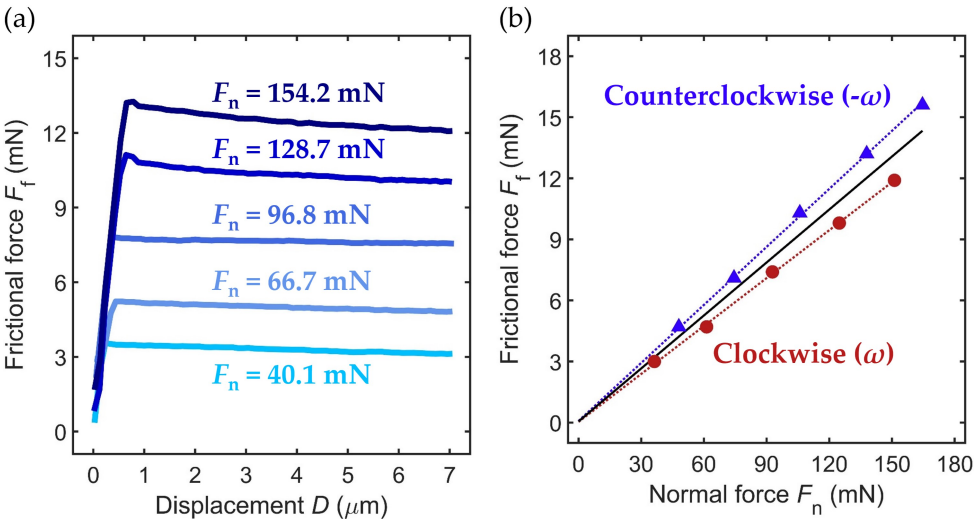

Figure 2.4: Sphere-on-flat sliding experiments with a rheometer-based setup. The frictional force is converted from the measured torque during sliding of a 3.18 mm Si_3N_4 sphere on a sapphire flat. The angular velocity of the rheometer is set to $\omega = 8.3 \times 10^{-5}$ rad/s corresponding to a sliding speed of 1 μm/s. (a) The friction-displacement curve demonstrates the frictional force (F_f) measured at different normal forces (F_n). (b) The average dynamic frictional force as a function of normal force measured in two opposite rotational directions; clockwise (ω, blue triangles) and counterclockwise ($-\omega$ red circles). The average frictional force is proportional to the normal force in both sliding directions. The black solid line interpolates the frictional force measured in two sliding directions.

constant oscillation amplitude. The surface profile is then recorded as the height of the cantilever while scanning on the material surface. Figure 2.6 demonstrates the surface topography of a 3 mm diameter Si sphere. The surface topography is measured using the largest scan size of the AFM Dimension ICON (93 μm $\times$ 93 μm) and the highest number of scan lines (4096) for one imaging frame. Such microscopic surface topography measurements by AFM enable bridging nanoscale surface features to microscopic contact phenomena. For example, by using AFM, the small amount of material removal from the macroscopic sphere surface due to wear can be captured by AFM as shown in Figure 2.7.

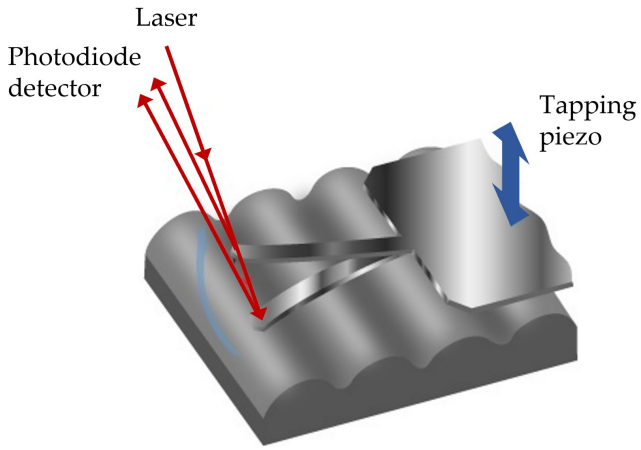

Figure 2.5: Schematic illustration of the Tapping mode used in atomic force microscopy (AFM). In Tapping mode AFM, the cantilever of the AFM probe is resonating at its resonance frequency, and a photodiode detector records the reflected laser. (image credit Bruker Corporation, `http://nanophys.kth.se`)

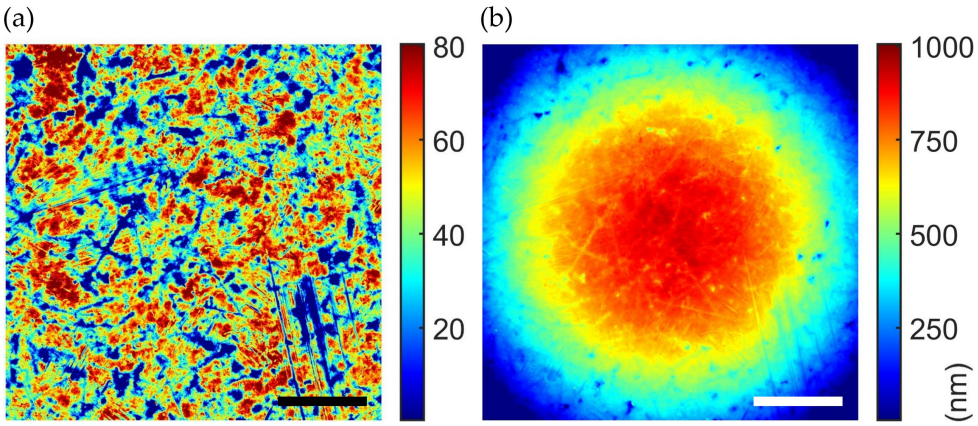

Figure 2.6: Atomic force microscopy (AFM) surface topography measured by Tapping mode. (a) The AFM surface topography of a 3 mm diameter pristine Si sphere; the sphere curvature is subtracted from the image (85 μm $\times$ 85 μm scan area with 4096 scan lines in one imaging frame corresponding to 430.6 nm^2 pixel size). (b) The surface topography of (a) with artificially imposed curvature of 1.5 mm radius. Scale bars, 20 μm.

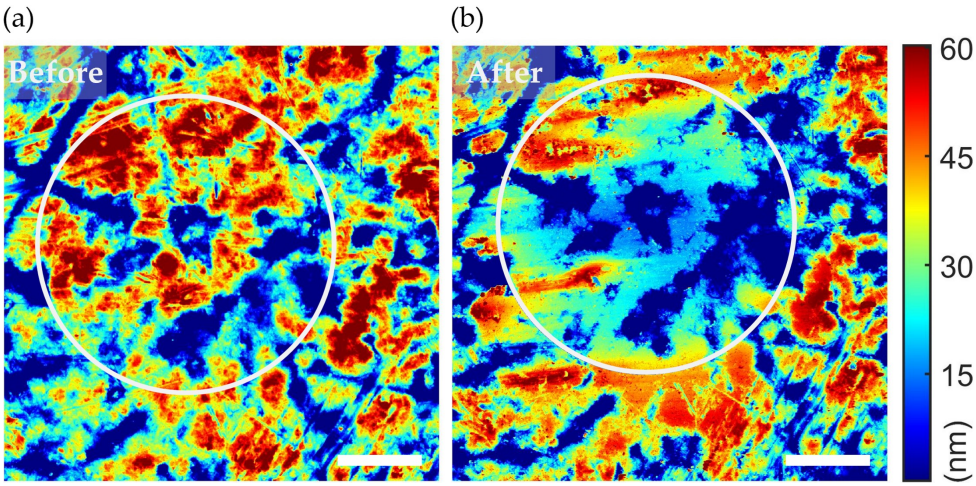

Figure 2.7: The change of the AFM surface topography before and after sliding. The surface topography of a 3 mm pristine Si sphere before (a) and after (b) 190 μm sliding on a Si wafer at a sliding speed of 1 μm/s and an applied load of 40 mN. The material removal on the Si sphere can be quantified by subtracting the surface topography (a) from (b). The volume of the material removed is about $3.3 \times 10^9 \text{nm}^3$. The resolution of the AFM images is the same as in Figure 2.6. Scale bars, μm.

2.2.2 3D laser scanning confocal microscopy

The 3D laser scanning confocal microscope (VK-X1000, Keyence)–or optical profilometer–is fast and efficient in performing non-contact and non-destructive surface topography and color map imaging with nanometer resolution; 0.5 nm in the height (Z axis) and 138 nm in the in-plane (X-Y axis) directions. During the measurement, a 404 nm violet semiconductor laser scans the material surface and measures the intensity of reflected light while varying the focus distance between the lens and the object. Within each pixel in the X-Y plane, the height of the surface is defined as the Z-position at which the highest reflected laser light intensity was observed. The 3D topography thus plotted provides the local surface heights as a function of the X-Y position on the surface. The color map is recorded based on the reflected white light at the focal point. The non-contact and non-destructive imaging technique of the profilometer can for instance be used to characterize the wear debris or the third body formation on a sphere as demonstrated in Figure 2.8.

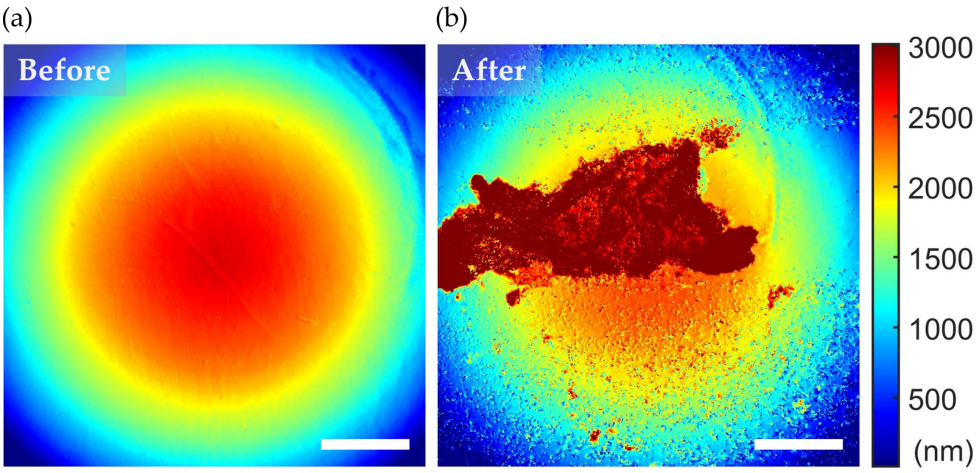

Figure 2.8: Profilometry of the surface topography before and after sliding. The surface topography of a 3.18 mm pristine sapphire hemisphere before (a) and after (b) 6 m repeated reciprocated sliding on a Si wafer at a sliding speed of 0.5 mm/s and an applied load of 100 mN. The formation of a third body is observed on top of the sapphire hemisphere (b). Scale bars, 30 μm.

2.3 Contact mechanics calculations

While a sphere is brought into contact with a flat surface, the roughness peaks–asperities–on the sphere surface support the applied load. The frictional force or resistance against sliding at the interface originates at the area of real contact formed by the contacting asperities. However, it is challenging to measure the area of real contact experimentally because the contact points are hidden from view by the contacting bodies. In **Chapters 3–6**, we carried out numerical contact calculations to quantify the contact mechanics at microscopic multi-asperity interfaces by using a Tribology Simulator that is publicly available at `www.tribology.org`. To perform the contact calculations, the mechanical properties of the sphere and flat materials, including the Young's modulus, Poisson ratio and hardness, are provided as input. Furthermore, the AFM surface topography of both surfaces is input to the Tribology Simulator which can then solve the elasto-plastic equations that describe the deformed interface through a half-space boundary element method [1, 2, 3]. Figure 2.9 demonstrates the calculated area of contact and contact mechanics between a pristine SiC sphere on a Si flat surface without roughness at 100 mN applied load.

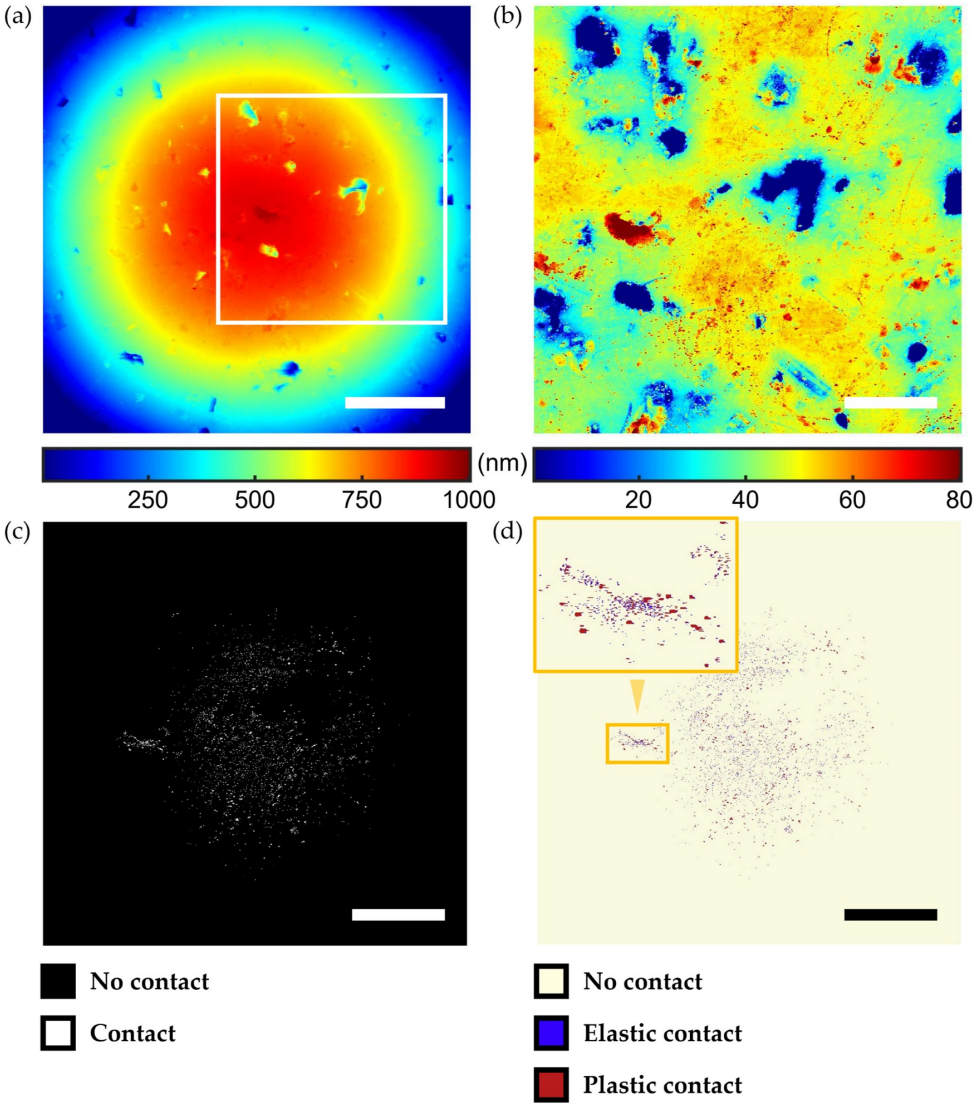

Figure 2.9: The boundary element method (BEM) contact calculation at microscopic multi-asperity interfaces. The BEM contact calculation is carried out to calculate the contact mechanics between a 3 mm diameter pristine SiC sphere on a Si flat surface without roughness. (a) The AFM surface topography of the SiC sphere. The white box indicates the region on the sphere surface that was brought into contact with a flat counter surface during the calculations. The contact region, without curvature of the sphere, is shown in (b). (c) The area of real contact (white patches) at the interface between the SiC sphere and the Si flat at 100 mN load. (d) The calculation predicts that the asperities on the SiC sphere deform the Si substrate elastically (blue patches) or plastically (red patches) at 100 mN load. The resolution of the images is the same as in Figure 2.6. The scale bars for (a) and (b–d) are 20 μm and 10 μm, respectively.

2.4 Fluorescence microscopy-based contact visualization

The main challenge in observing contact phenomena lies in the fact that the contact interface is often hidden from view by the contacting bodies. Many analytical and numerical methods are proposed to calculate contact mechanics [4]. In **Chapter 5**, we introduce an *in situ* contact visualization method to directly observe the area of real contact at the asperity-level. In the visualization measurements, a DSR 301 Anton Paar rheometer is used to perform friction measurements. The rheometer is placed on top of an inverted laser scanning confocal microscope (Axiovert 200M, Zeiss) with an LSM 5 PASCAL (Zeiss) laser scanning module (Figure 2.10). As described in **Chapter 2.1.2**, the rheometer brings a 3.18 mm diameter Si_3N_4 sphere into contact with a sapphire flat through the rigid adapter at different normal forces. A droplet of fluorescent liquid 3,6-bis((2-ethylhexyl)oxy)-1,2,4,5-tetrazine (Figure 2.10) is placed between the sphere and the flat. 514 nm laser light was used to excite the fluorescent molecules. The fluorescence intensity at the interface is imaged using a 63× 1.4 numerical aperture objective (Plan-Apochromat, Zeiss) at a pixel size of ∼3400 nm^2.

To obtain the local gap at the Si_3N_4 sphere-on-sapphire flat interface, we calibrate the relation between fluorescence intensity (I) and local gap (Gap). We place the sphere on the flat and do not apply an external load. Subsequently, the fluorescence intensity profile along two lines (Figure 2.11a) is compared to the gap profile that can be predicted based on the undeformed sphere geometry (Figure 2.11b). From the comparison, a proportionality constant that links intensity to local gap can be extracted. Below we briefly describe how to observe and quantify the area of real contact and the contact stiffness at the interface using the fluorescence intensity imaging. In **Chapter 5**, the experimental parameters used to perform the contact visualization experiments are mentioned in detail.

2.4.1 Area of real contact

Figure 2.12 demonstrates the distribution of fluorescence intensities measured at the Si_3N_4 sphere-on-sapphire flat interface (Figure 2.13a) as a function of gap value. We find a distinct intensity peak at low but non-zero fluorescence intensities (gaps). The peak is at a gap of ∼6 nm, comparable to the size of the fluorescent molecules. To define the area of real contact experimentally, we set an intensity threshold less than or equal to the gap at the peak and consider all pixels with an intensity below this

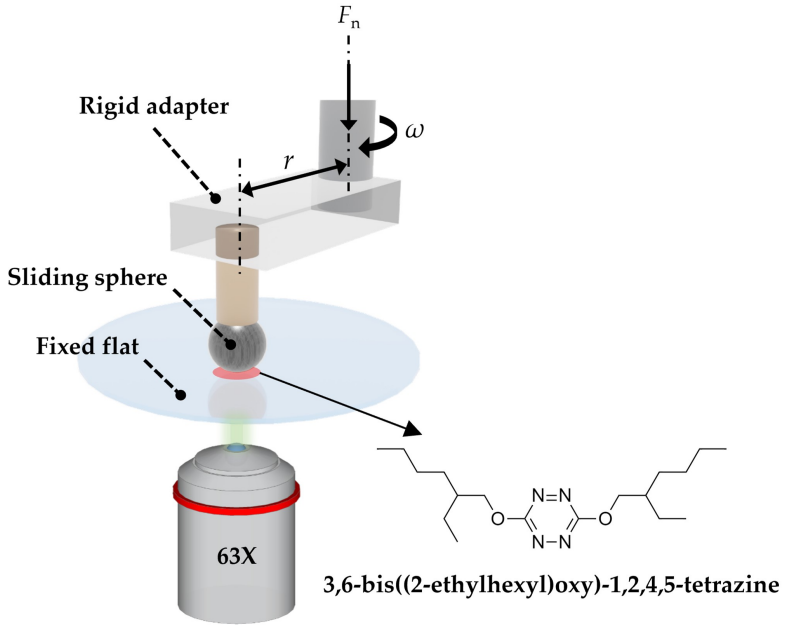

Figure 2.10: A schematic illustration of the experimental setup used for contact visualization and frictional force measurements. The structure of the fluorescent liquid (3,6-bis((2-ethylhexyl)oxy)-1,2,4,5-tetrazine) is shown on the right.

threshold value to belong to the area of real contact as plotted in Figure 2.13b.

2.4.2 Contact stiffness

Normal contact stiffness quantifies the deformation of the asperities in the normal direction as a function of normal load. To measure the local interfacial stiffness, we consider the fluorescence intensities–and thus gaps–measured within a circle at the center of the contact. The circle size is scaled with the Hertzian contact area(Figure 2.14a–e):

$$A_{\text{Hertz}} = \pi\left(\frac{3F_{\text{n}}R}{4E_{\text{eff}}}\right)^{\frac{2}{3}} \tag{2.1}$$

where R ($= 1.59$ mm) is the radius of Si_3N_4 sphere and $E_{\text{eff}} = \left(\frac{1-\nu_1}{E_1} + \frac{1-\nu_2}{E_2}\right)^{-1}$ is the effective modulus of Si_3N_4 (labelled as 1) and sapphire (labelled as 2). The contact stiffness (k) at the multi-asperity interface can then be calculated by using Hook's law (Figure 2.14f): $k = \frac{F_{\text{n}}}{\text{Gap}}$.

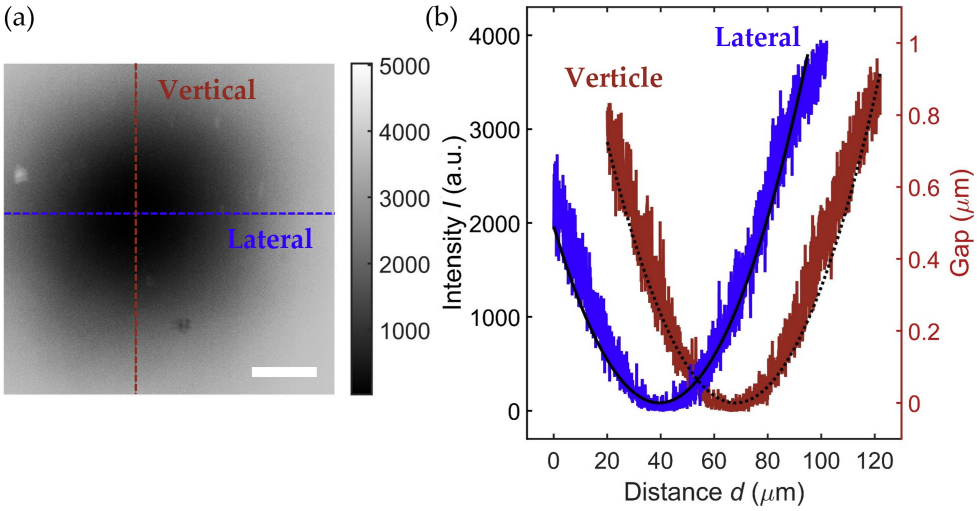

Figure 2.11: The intensity-gap calibration. (a) The fluorescence intensity (I) at the interface between a Si_3N_4 sphere and a sapphire flat. The cross-sectional fluorescence intensity (I) profile taken through the sphere-on-flat contact center in both orthogonal in-plane directions is shown in (b) where the lateral (blue) and vertical (red) curves are manually shifted for clarity. Black solid and dotted lines in (b) show the expected sphere-on-flat gap based on the sphere diameter and on the assumption that there is no roughness and no deformation. Scale bar, 20 μm.

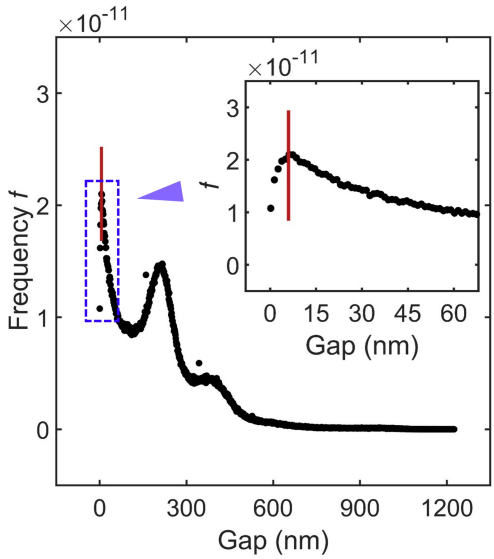

Figure 2.12: Fluorescence intensity distribution as a function of the local gap. The fluorescence intensity shows a clear peak at a gap of ∼6 nm (red line, inset figures) at a normal force of 410 mN. The corresponding gap value at the peak position determines the threshold for the area of real contact in Figure 2.13.

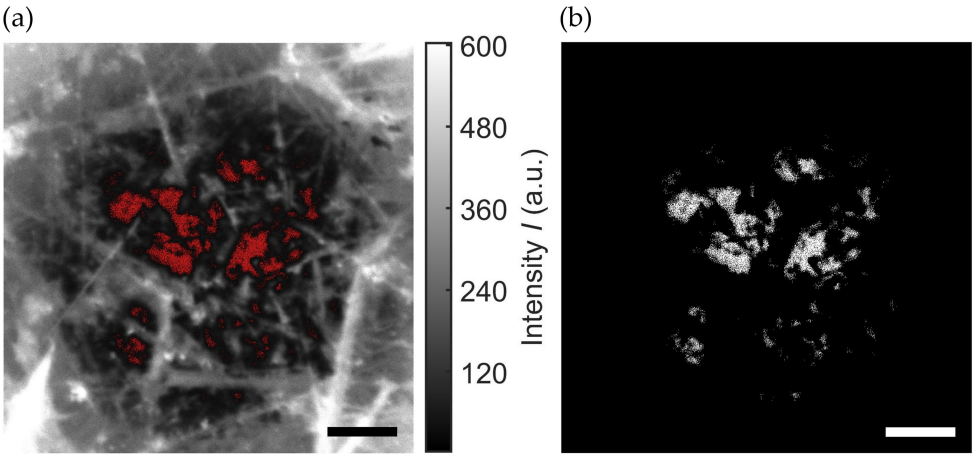

Figure 2.13: Visualization of the contact between a Si_3N_4 sphere and a sapphire flat (a) The fluorescence intensity map at the Si_3N_4 sphere-on-sapphire flat interface. Higher intensity indicates that more fluorescent molecules are filling a larger average gap within a pixel. The red patches correspond to the pixels within which the intensity is smaller than the threshold (Figure 2.12)–average gap is smaller than 6 nm. (b) The area of real contact (white patches) is defined as the red patches in (a). Scale bars, 10 μm.

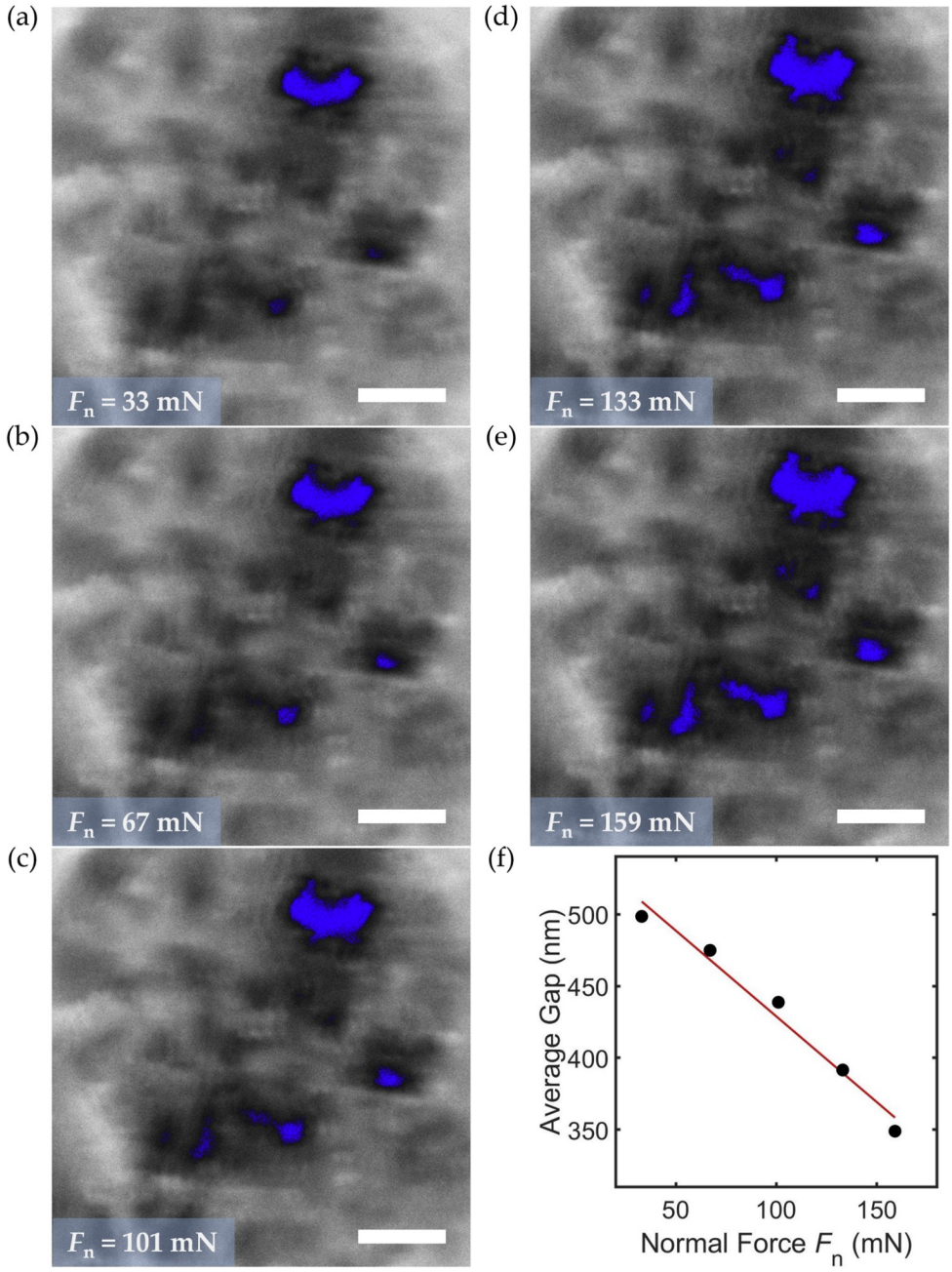

Figure 2.14: Contact stiffness measurements at a Si_3N_4 sphere-on-sapphire flat interface. (a–e) The fluorescence intensity map at different normal force. The area of real contact (blue patches) increases with normal force (F_n). The average gap at the center of the contact is plotted as a function of normal force in (f). The contact stiffness is defined as the slope between the average gap and normal force, $k = 8.4 \times 10^5$ N/m. Scale bars, 20 μm.

Bibliography

[1] IA Polonsky and LM Keer. A numerical method for solving rough contact problems based on the multi-level multi-summation and conjugate gradient techniques. *Wear*, 231(2):206–219, 1999.

[2] Christophe Jacq, Daniel Ne´ lias, Gérard Lormand, and D Girodin. Development of a three-dimensional semi-analytical elastic-plastic contact code. *J. Trib.*, 124(4):653–667, 2002.

[3] Aydar Akchurin, Rob Bosman, Piet M Lugt, and Mark van Drogen. On a model for the prediction of the friction coefficient in mixed lubrication based on a load-sharing concept with measured surface roughness. *Tribology letters*, 59(1):1–11, 2015.

[4] Martin H Müser, Wolf B Dapp, Romain Bugnicourt, Philippe Sainsot, Nicolas Lesaffre, Ton A Lubrecht, Bo NJ Persson, Kathryn Harris, Alexander Bennett, Kyle Schulze, et al. Meeting the contact-mechanics challenge. *Tribology Letters*, 65(4):1–18, 2017.

CHAPTER 3

Wear particle dynamics drive the difference between repeated and non-repeated reciprocated sliding

The dependence of the sliding mode (repeated vs. non-repeated reciprocated sliding) on the friction and wear behavior of ball-on-flat, brittle non-metallic interfaces in ambient air conditions is evaluated. Repeated sliding promotes the formation of a third body (compressed wear particles) that stabilizes the friction. Non-repeated sliding shows reduced evidence of third body formation, and instead a steady increase in friction. The proposed mechanism driving the non-repeated friction behavior is attributed to a gradual reduction in the ball surface roughness, leading to an increased area of real contact and greater capillary bridge forming across non-contact regions of the interface.

3.1 Introduction

Friction and wear are of paramount importance to the performance and lifetime of applications with high economic and societal impact such as engines, wheels and industrial production machines [1]. Estimates show that tribological contacts consume 23% of the world energy budget: 20% is spent on overcoming friction and 3% on repairing or substituting components that have worn as a result of friction [2]. These staggering numbers and the applications that they represent have motivated numerous experiments that aim to understand, manipulate and reduce friction and wear under industrially relevant conditions, mimicking for instance the behavior of combustion engines [3], turbines [4], train wheels [5], robotic grasping [6] and micro- and nanoelectromechanical systems [7]. While some of these applications involve repeated, reciprocated sliding of the same two surfaces against each other, others slide in a non-repeated fashion, meaning that the slider always contacts a fresh, unworn counter surface. Examples of the latter include rolling wheels [8], walking [9], grabbing [10] (grabbing or clamping typically involves slip due to misalignment and curvature of the touching surfaces), cutting [11], read/write cycles of hard drives [12] and even atomic force microscopy imaging [13, 14]. Interestingly, experiments that are designed to reproduce the friction behavior observed in various applications are almost exclusively [15, 16, 17] performed in a repeated fashion [3, 4, 18]–also when the application involves non-repeated sliding [5, 8, 11, 19]. Furthermore, the potential consequences this has for the tribological behavior is often overlooked. Here, we systematically study the friction and wear behavior of various types of nominally dry contacts between brittle non-metallic materials sliding in repeated or non-repeated fashion.

3.2 Experiments

In the ball-on-flat friction experiments (Figure 3.1a inset), sapphire (Al_2O_3), silicon carbide (SiC) and glass balls were slid against Si wafers or glass flats in repeated and non-repeated fashion in ambient air (21–23 °C, 20–60% relative humidity). These two different sliding modes are illustrated in the inset of Figure 3.1a: in non-repeated sliding the ball was lifted after each forward and backward stroke (1 cycle), and placed back into contact with an untouched part of the flat. During repeated sliding the ball was reciprocated at a fixed location on the flat. In both the repeated and the non-repeated experiments, the stroke length (L), normal force (F_n) and sliding speed

(v) were kept constant at 20 mm, 0.1 N and 0.5 mm/s, respectively. These materials and experimental parameters were chosen to resemble the silicon wafer-on-support contacts that limit the positioning accuracy in nanolithography machines [20]. The used materials and their RMS roughness are further described in Table 3.1. The tribological experiments were carried out using a Universal Mechanical Tester (UMT TriboLab, Bruker) that was set to acquire force and position data at a rate of 5 Hz. Each friction experiment consisted of 150 cycles, totaling a sliding distance of 6 m. In the non-repeated experiments, the time required to move the ball between subsequent cycles was approximately 27 s.

To characterize the wear of the sliding bodies, optical focus variation profilometry measurements were performed *ex situ* using a laser scanning confocal microscope (Keyence VK-X1000). Furthermore, the wear scars on the balls and the wear tracks on the Si flats were imaged and analyzed using scanning electron microscopy (SEM, FEI Verios 460) and SEM-integrated energy dispersive X-ray (EDX, Oxford) measurements. The surface topography of the sliding bodies was measured by tapping mode atomic force microscopy (AFM) (Dimension Icon, Bruker) where the nominal tip radius of AFM tips carried out in the measurements was 8 nm.

3.3 Results and discussion

Figure 3.1a shows the evolution of the measured frictional force (F_f) as a function of the sliding distance for the repeated and non-repeated sapphire-on-Si wafer experiments. In the repeated sapphire-on-Si wafer experiments strong fluctuations in friction were initially observed, followed by a more stable frictional force of roughly 50 mN after the first $\sim$0.2 m of sliding (see Figure A.1a). The non-repeated version of the otherwise identical experiment resulted, in the majority of cases, in clearly different friction behavior: the initial friction fluctuations observed during repeated sliding were not present and the frictional force increased gradually with sliding distance. After 6 m of sliding the frictional force had doubled, from $\sim$55 mN to $\sim$110 mN. It should be noted that this behavior was not observed in all experiments; in a few cases we observed running-in behavior followed by a stable frictional force, see Figure A.2. This is discussed later in relation to third body formation. In the SiC-on-Si wafer experiments (Figure 3.1b), the friction behavior is qualitatively similar to that observed in the sapphire-on-Si wafer experiments. In the repeated SiC-on-Si wafer experiment, unstable friction running-in behavior during the first $\sim$0.4 m of sliding is followed by a more stable evolution of the

Table 3.1: Materials data. The RMS roughness was measured using 5 μm $\times$ 5 μm tapping mode AFM measurements at a pixel size of 5 nm.

Material	Type	RMS roughness (nm)
3.18 mm Sapphire ball	Single crystal sapphire	9.0
3mm SiC ball	Direct sintered SiC	48.7
Si-wafer flat (0.5 mm thick)	Boron doped <100>Si with native oxide layer	0.9
4 mm Glass ball	Soda lime glass (Sigmund Lindner)	36.6
Glass flat (1 mm thick)	Extra white soda lime glass (Thermo scientific)	1.0

frictional force. In the non-repeated experiment there is no running-in behavior and the frictional force gradually increases with sliding distance. The relative increase in friction is, however, less pronounced in the SiC-on-Si wafer experiment than the sapphire-on-Si wafer experiment. Furthermore, in the repeated SiC experiment, the friction gradually decreases after the run-in phase (up to ∼0.4 m sliding, Figure A.1b).

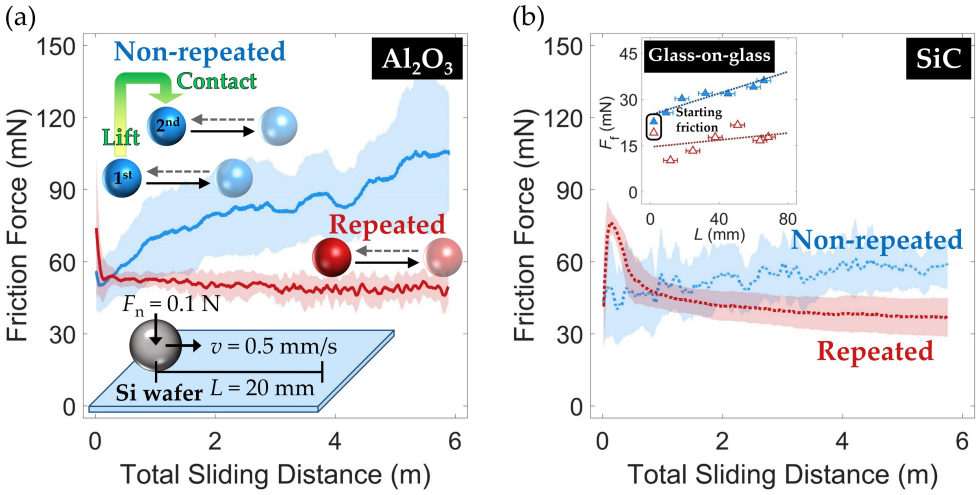

Figure 3.1: Friction measurements during repeated and non-repeated sliding of (a) a sapphire ball on a Si wafer and (b) a SiC ball on a Si wafer. Insets in (a) show schematic illustrations of the sliding mode. The inset in (b) shows glass ball on glass flat friction measurements. The solid lines represent the moving average frictional force, averaged over 2 cycles, and the shaded areas adjacent to this line indicate the standard deviation in the measured frictional forces for a minimum of three identical independent experiments (see also Figure A.3). For the glass-on-glass friction experiments (inset 1b) each data point represents the average frictional force for 4 cycles. All three systems display an increase in the frictional force (F_f) with sliding distance (L) for non-repeated sliding.

To characterize the wear behavior of the studied interfaces, optical profilometry imaging of the contact region of the balls was performed both before and after the friction experiments (Figures 3.2, A.4 and A.5). The quantitative wear results are given in Table 3.2, and a summary of all predominant wear mechanisms can be found in Table A.1.1. The profilometry images clearly demonstrate that a spherical cap is worn off from the sapphire ball during the non-repeated friction experiment, resulting in an average specific wear rate of $K = 6.5 \pm 2.8 \times 10^3$ μm/Nm (based

on a minimum of three independent experiments): $K = \frac{V}{F_n L}$ where V is the wear volume, determined based on the profilometry data. The wear scar on the sapphire ball that has undergone repeated sliding looks very different; a substantial amount of compressed debris–or third body [21]–has accumulated on the region of the ball that was in contact with the wafer. This was reproducible for three independent identical experiments. The third body was loosely attached and could easily be removed from the ball surface by cleaning for 60 min in an ultrasonic bath containing acetone (Figure 3.2c). Removing the third body revealed that the 'repeated' ball had obviously worn less than in the non-repeated experiment: the average wear rate for the sapphire balls during repeated sliding was $K = 1.0 \pm 0.4 \times 10^3$ μm/Nm: an average of six times less than that measured for the non-repeated experiment.

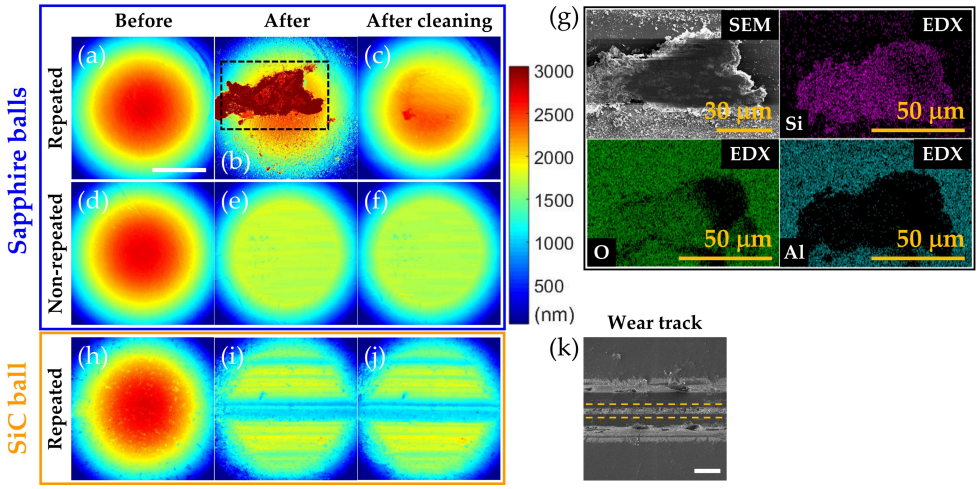

Figure 3.2: *Ex situ* height profiles and surface characterization of sliding bodies. (a), (d), (h) Measured height profile before the friction experiment. (b), (e), (i) Measured height profile after the friction experiment. (c), (f), (j) Measured height profile after ultrasonic cleaning of the ball after the friction experiment. (g) SEM and EDX analyses of the third body on the contact zone of the sapphire ball (from b) after a repeated experiment. The silicon (Si) and oxygen (O) signals originate from the third body in the EDX analysis. Little to no aluminum (Al) can be observed within the third body, as compared to the background which consisted of Al_2O_3 (sapphire). (k) SEM image of the wear track and the Si wafer after the repeated SiC experiment (h–j). The orange dashed lines indicate the area within the wear track with increased silicon oxide content. The topography of the wear track matches that of the worn SiC sphere (see also Figure 3.3). Scale bars, 50 μm.

Table 3.2: Wear observations.

Ball	Flat	Sliding mode	$K_{ball} \times 10^3$ (μm^3/Nm)	Third body location	Third body origin
Sapphire	Si wafer	Repeated	1.0 ± 0.4	Predominantly adhered to ball	Si wafer
		Non-repeated	6.5 ± 2.8	Not observed[†]	
SiC	Si wafer	Repeated	9.7 ± 0.5	Predominantly adhered to Si wafer	Si wafer and SiC fragments
		Non-repeated	7.7 ± 1.3	Small amount[‡] adhered to ball and Si wafer	

[†] Note that, in a few exceptional cases where the relative humidity of the air environment was slightly higher, a small amount of third body formation was observed on the ball; this was much less than in the repeated case.

[‡] Much less than in the repeated case.

To understand the nature of the third body formed on the sapphire ball during the repeated experiment, EDX analysis was performed on the ball from Figure 3.2b (see Figure 3.2g). The measurements indicate that the third body consists mainly of silicon and oxygen and no significant amounts of aluminium, strongly indicating that the third body is wear debris, primarily SiO_x and originating from the Si wafer (Table 3.2). This is supported by SEM-EDX analysis of the Si flat performed after a repeated experiment, which clearly shows that SiO_x debris particles remain next to the wear track but not inside the wear track (Figure A.6d–f). It is unlikely that the SiO_x originates from accumulation of the native oxide, as the calculated volume of the SiO_x in the contact region on the sapphire ball (Figure A.7) was $\sim 470 \times 10^3$ μm^3, which is much greater than the corresponding approximate volume of native oxide on the Si wafer wear track ($20 \times 10^3 \times 60 \times 2 \times 10^{-3}$ [22] $= 2.4 \times 10^3$ μm^3). More SiO_x debris was observed at the ends and either side the wear track (Figure A.6a and c), than in the central region of the flat. The large amount of debris suggests that an abrasive wear mechanism occurred during sliding. It is unclear whether the silicon wear debris found on the contacts becomes oxidized before, during or after attachment to the ball.

While in the SiC-on-Si wafer experiments the friction behavior is qualitatively similar to that observed in the sapphire-on-Si wafer experiments, an important difference is that the third body is predominantly located in the central region on the wear track of the Si wafer (Figure 3.3b and c) rather than the SiC ball after the repeated sliding experiment (Figure 3.2i and j). The third body in this case comprises a ridge of compressed SiO_xC_y debris, likely originating from oxidized Si debris from the wafer and small fragments of SiC from the ball (Table 3.2). Furthermore, the profile of this third body, recorded perpendicular to the sliding direction, perfectly matched that observed on the SiC ball (along the same direction, Figure 3.3d). This strongly suggests that in the repeated sliding SiC-on-Si wafer experiment, the sliding was accommodated at the ball-on-third body interface. This would then also explain why the difference in ball wear between repeated and non-repeated SiC-on-wafer experiments was much smaller than that in the sapphire-on-Si wafer experiments, in which the SiO_x third body adhered to the ball (in repeated experiments). The SiO_x third body may adhere more strongly to the sapphire ball than to the SiC ball because the sapphire ball was much smoother and therefore more susceptible to physical or capillary adhesion [23]. In all non-repeated experiments, we do not observe such dominant SiO_x third bodies within the wear track on the wafer or on the ball, as seen for repeated experiments.

Our *ex situ* observations thus suggest that the observed difference in friction

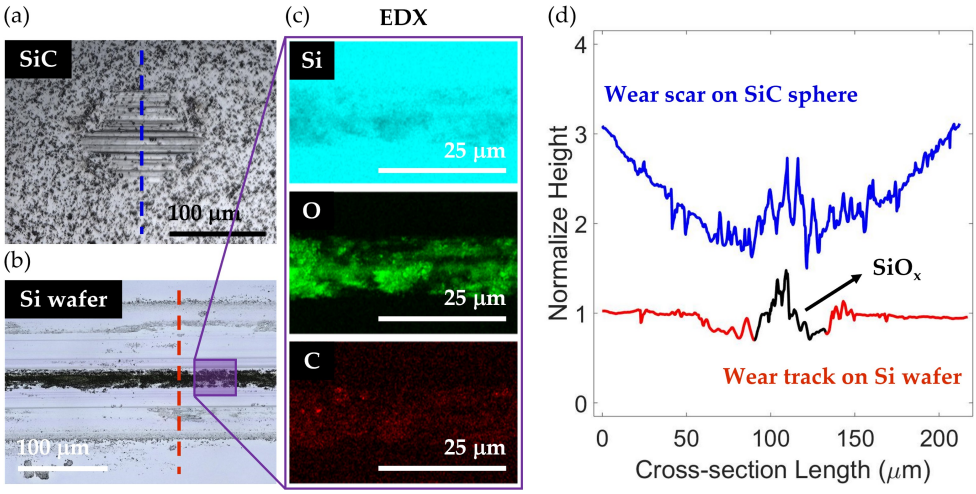

Figure 3.3: Surface characterization for the repeated SiC-on-Si wafer experiment. The optical image of (a) the SiC ball and (b) the corresponding wear track on the Si substrate after a repeated sliding experiment. (c) The EDX analysis demonstrates the formation of SiO_x at the center of the wear track on the wafer, where the results shows less Si signal but a strong O and carbon (C) signal illustrating that C has transferred from the SiC ball to the Si wafer. (d) The height profile taken from the cross-section of (a) and (b) shows that the surface topography of the wear scar and the wear track match, indicating that the sliding motion was likely accommodated at the interface between the ball and the SiO_x.

between repeated and non-repeated sliding is related to the formation (or absence) of a third body at the sliding interface. To test this more directly, the friction experiments were repeated, but with different materials, in a microscopy setup (Figure 3.4a) consisting of a rheometer mounted on top of an inverted microscope. In this setup, a glass ball is fixed off-center to the rheometer tool which can be rotated and moved vertically, enabling measurement of and control over the normal and tangential force exerted at the ball-on-flat interface [24]. As with the UMT experiments, the ball diameter was 4 mm, the normal force was kept at 0.1 N and the sliding speed was 0.5 mm/s. To enable *in situ* visualization of the interface, the repeated and non-repeated experiments were performed with transparent materials: glass balls on glass flats. The microscope illuminates and images the ball-on-flat interface through the transparent flat. In a typical microscopy image of the interface, we observe a black central region enclosed by interference fringes, the first of which corresponds to a gap of 114.5 nm between the ball and the flat [25]. In the central black region the

surfaces have approached to within 114.5 nm, this is the area of apparent contact.

Figure 3.4b–e displays the contact images obtained before and after 40 cycles of repeated or non-repeated sliding. Even though the materials are different, it was observed that the glass-on-glass interfaces behave qualitatively similar to the sapphire or SiC-on-Si wafer interfaces studied above: wear debris is collected at the interface as a third body during repeated sliding (Figure 3.4c), but not–or much less so–during non-repeated sliding (Figure 3.4e). Furthermore, the friction measurements showed that non-repeated sliding results in a clear increase of friction with sliding distance, while repeated sliding does not, or much less so (Figure 3.1b inset). Hence we observe that in three different materials systems the frictional force measured during a repeated sliding experiment stabilizes after a run-in phase, a phenomenon that has also been observed elsewhere [26], while that measured during non-repeated sliding gradually increases with sliding distance. Based on the microscopy and profilometry measurements (Figure 3.4b–k) it can be concluded that, during the run-in phase observed in repeated experiments, debris particles were compressed into a third body that subsequently stabilizes the friction: supplementary videos S1–S3 (see `https://doi.org/10.1016/j.triboint.2019.105983`) show a typical example of the glass-on-glass interface recorded during repeated sliding (S1), non-repeated sliding (S2) and lifting of the sphere (S3) after repeated sliding. It is important to note that while non-repeated sliding suppresses the formation of a third body, we still observed a third body in some non-repeated sapphire-on-Si wafer experiments that were carried out in an air environment with a slightly higher average relative humidity of 45%, compared to other experiments at 34%. For these particular experiments, the friction measurements showed running-in behavior similar to that in the repeated experiments (Figure A.2). As mentioned previously, the exceptionally low roughness of the sapphire balls (Figures 3.5 and A.8) may enable wear debris to adhere to the ball surface through capillary or physical adhesion, even in some of the non-repeated experiments.

Our results thus show that there is much less chance of third body formation at the interface during non-repeated sliding. In this case, it is important to consider the mechanism responsible for the gradual increase in friction observed in such experiments (e.g. Figure 3.1). To address this question, the wear behavior for sapphire-on-Si wafer interfaces was analyzed in more detail.

The effect of the wear should be considered in terms of the continuous change in the real contact pressure and real area of contact occurring at the sliding interface during the wear process, which is difficult to determine experimentally. Ignoring roughness, the change in contact pressure between the start and end of the experi-

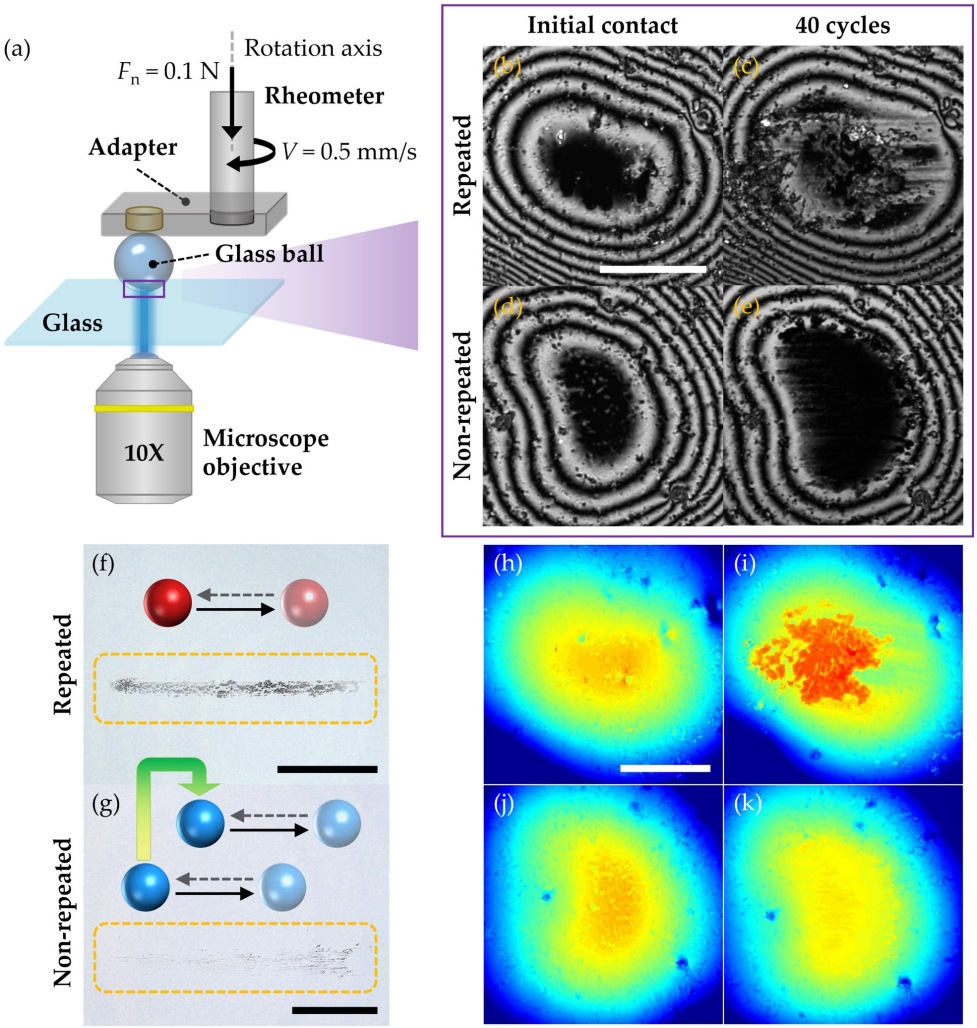

Figure 3.4: Imaging of the interface between a glass ball and a float glass coverslip and *ex situ* optical images and height profiles recorded before and after the friction experiments. (a) Visualization/friction experiments were performed using an inverted confocal laser scanning microscope on top of which a rheometer was mounted. The glass ball is fixed to the rheometer tool at a distance of 12.98 mm from the rotation axis. By imposing an angular velocity of 3.52×10^{-2} rad/s, the ball is forced to slide with a velocity of 0.5 mm/s and makes 1 mm strokes. (b), (d) Initial contact at the interface and (h), (j) height profile of glass ball before sliding. Debris is collected at the interface (c) and is observed on the ball (i) and on the substrate (f) after repeated sliding. After non-repeated sliding, there is no visible debris at the interface (e) or on the ball (k), some debris is left on each of the sliding tracks (g). In both experiments the area of apparent contact increases as a result of the wear. The contact force is 100 mN in all images. White and black scale bars are 50 μm and 100 μm, respectively. The color scale in (h–k) is identical to that used in Figure 3.2.

ment can be estimated by calculating the Hertzian contact stress (P_{Hertz}) at the start and, assuming a fully conforming contact, the contact pressure at the end of the experiment (P_{final}). This gives a change in contact pressure from $P_{\text{Hertz}} = 428$ MPa to $P_{\text{final}} = 11.4$ MPa, where the latter value is based on the area of the flat cap worn off of the ball in Figure 3.5c. Note that the real contact pressure at the start of the experiment is likely to be higher than P_{Hertz} because the ball and wafer roughness is not taken into account. To estimate the effect of roughness, we carry out boundary element model (BEM) calculations [27], which in this case were performed using the Tribology Simulator that is publicly available at `www.tribology.org` and using data from optical profilometry of the ball before and after the sliding experiment. These simulation results are limited by the resolution and quality of the optical profilometry measurements, which were carried out with a resolution of approximately 50 nm in lateral and 20 nm in height directions. The results of the calculated contact gap profiles are shown in the Appendix A Figure A.9a and b and yield real contact pressures of 2.62 GPa and 0.35 GPa for, respectively, the initial contact and after sliding. Although, as expected, these surface pressures are much higher than those calculated without roughness, it is evident that a large decrease in contact pressure occurs. Thus, the real contact pressure and real contact area rapidly change as a result of wear, and the wear rate is unlikely to be constant.

A different way to consider the wear behavior is to estimate the rate of material removal on the atomic scale. For rough surfaces, the maximum contact pressure exerted at the sapphire-on-Si-wafer interface can never exceed the hardness of the Si-wafer: this would cause the wafer to plastically deform such that the area of real contact increases and the contact pressure drops below the hardness again. This means that during the (non-repeated) sapphire-on-Si wafer friction experiments the minimum area of real contact (A_{min}) between the ball and the substrate is:

$$A_{\text{min}} = \frac{F_{\text{n}}}{H} \tag{3.1}$$

where $F_{\text{n}} = 0.1$ N and $H = 5.1$ GPa is the hardness of the boron doped single crystal silicon <100> wafer that we used [28], yielding:

$$A_{\text{min}} = 2 \times 10^{-11}\ \text{m}^2 \approx \frac{2 \times 10^{-11}}{(2 \times 10^{-10})^2} = 5 \times 10^{8}\ \textit{atoms} \tag{3.2}$$

Thus, over the whole area of the contact, at least 5×10^8 *atoms* on the ball surface must touch and slide over the wafer surface at any time, where 2×10^{-10} m is used as an approximate atom-to-atom distance within the ball (note that the goal of this calculation is to provide only order-of-magnitude estimates). Using as an example

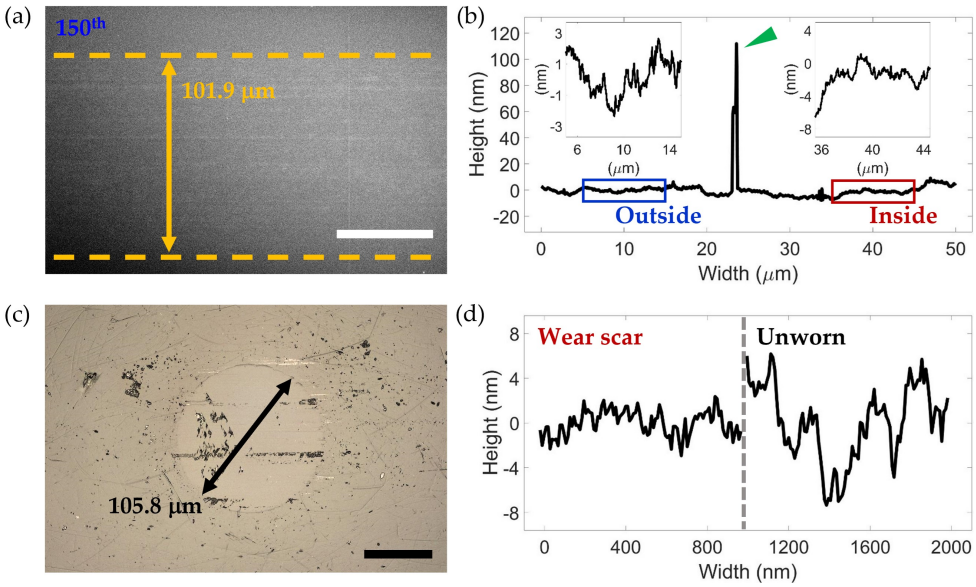

Figure 3.5: The surface topography before and after a non-repeated sapphire-on-Si wafer experiment. (a) SEM image of the last (150^{th}) wear track on the wafer. (b) AFM line scan of the last wear track on the wafer recorded perpendicular to the sliding direction. The green arrow indicates the edge of the wear track at which debris particles were occasionally found. Inset figures show the surface roughness outside and inside the wear track. (c) Microscopy image of the sapphire ball. The width of the wear scar on the ball matches that of the track on the wafer (a). (d) AFM line profiles measured in- and outside the wear scar on the sapphire ball. The roughness of the wear scar ($R_q = 2.6 \pm 0.9$ nm) is significantly smaller than that measured on the unworn sapphire ($R_q = 9.0 \pm 3.3$ nm nm). Scale bars, 50 μm.

the total wear volume of the sapphire ball shown in Figure 3.5c, measured after a sliding distance of 6 m, we can estimate how many atoms on the ball surface are worn off during a non-repeated experiment:

$$\frac{3.9 \times 10^{-15}\ \mathrm{m}^3}{(2 \times 10^{-10}\ \mathrm{m})^3} \approx 5 \times 10^{14}\ atoms \tag{3.3}$$

It follows that on average, atoms on the ball surface that make contact with the substrate slide at least 6 μm before they are worn off:

$$\frac{6\ \mathrm{m} \times 5 \times 10^{8}}{5 \times 10^{14}} = 6\ \mu\mathrm{m} \tag{3.4}$$

We therefore conclude that the ball wear is very mild and the above analysis suggests that this may even occur atom-by-atom [29, 30]: when the ball slides over a distance that is the equivalent of more than tens of thousands of atomic spacings, only a single atomic layer is worn off from the sapphire ball.

The wear tracks that are left on the silicon wafer after the non-repeated experiment were also analyzed using AFM and SEM imaging. Although the very first strokes on the wafer may involve some abrasive wear resulting in scratches on the wafer, no, or very little, evidence of wear was found during the subsequent strokes (Figures 3.5a and 3.6b); the wafer roughness is greater than the height difference measured inside and outside the tracks (Figure 3.5b).

These observations and calculations suggest that adhesive friction, controlled by the area of real contact, is the main friction mechanism in the non-repeated experiment. The wear may however be governed by the tribochemical behavior at the interface [31]. An adhesion friction mechanism is also supported by the observation that for pristine sapphire-on-Si wafer interfaces the frictional force–measured at varying normal forces during 100 μm strokes–is strictly proportional to the normal force (Figure 3.6a), despite the fact that the area of apparent contact does not increase linearly with the normal force for ball-on-flat interfaces [32]. To further study the interplay between this coefficient of friction and the wear that occurs in non-repeated experiments, a sapphire ball was subjected to a milling procedure. The ball was worn by sliding it along a 6 m spiral-shaped track over the wafer at a fixed normal force of 50 mN. This spiral-shaped sliding track ensured that the ball always encountered fresh wafer surface during the whole experiment. Based on the observations above, it is reasonable to assume that this type of sliding avoids the build-up of a third body on the sphere; indeed AFM PeakForce Tapping measurements [33] performed after the milling procedure confirm this (Figure A.10). Repetition of the non-repeated friction experiment after the ball had been worn in this way showed that the coefficient of friction had substantially increased (Figure 3.6a), similar to the behavior observed in the non-repeated sapphire-on-Si wafer experiments (Figure 3.1a). Interestingly, if the surrounding air is replaced with dry nitrogen (N_2), a lower coefficient of friction of $\mu = 0.57$ was measured, a value between that measured before wearing the ball ($\mu = 0.5$) and after milling ($\mu = 0.65$) in ambient conditions.

These experiments can be interpreted as follows: During the milling procedure, and also during non-repeated sliding, the surface roughness on the balls is reduced as a consequence of mild wear (Figure 3.5). This reduced roughness leads to a larger area of real contact and with that a greater adhesive friction and coefficient of friction

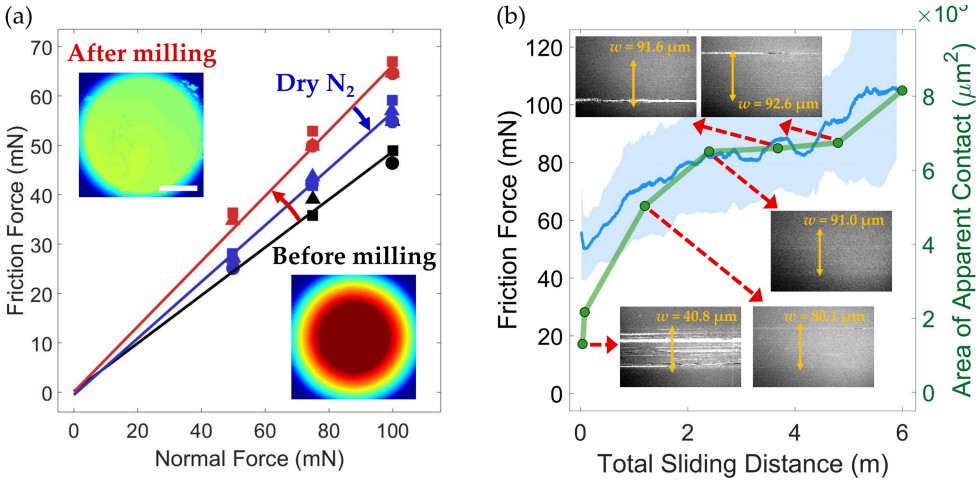

Figure 3.6: The friction at a sapphire-on-Si wafer interface. (a) Friction measurements at varying normal forces were performed in a non-repeated fashion using 100 μm (uni-directional) strokes and a sliding speed of 50 μm/s (black data points). The coefficient of friction increases substantially (red data points) after the ball has been worn (see main text). The coefficient of friction is lower when measured in dry N_2 (blue data points, measured after milling) compared to the ambient measurement. The inset figures show the height profile of the sapphire ball before and after the friction experiments. The color scale is identical to that used in Figure 3.2. Scale bar, 50 μm. (b) The area of apparent contact (A_p) between a sapphire ball and a Si wafer is calculated using the width (w) of the wear tracks on the wafer: $A_p = \pi \times \frac{w^2}{4}$. Inset, SEM images of the various wear tracks.

[34]. Additionally, as the ball becomes smoother, the total area, within which the gap between the ball and the flat is only a few nanometers, becomes larger (Figure 3.5d). Across such nanometric gaps, the water layers that cover most surfaces in ambient conditions can form capillary bridges [35, 36, 37], thereby pulling the surfaces into closer contact and increasing the friction [38]. This capillary effect can however be reversed by changing the atmosphere at the interface to dry N_2, thereby removing the influence of the capillary bridges (Figure 3.6a). Furthermore, since the capillary effect is active at locations across the interface with a finite gap, the friction can be expected to correlate with the area of apparent contact: the larger the area of apparent contact, the larger the area within which the contacting surfaces experience adhesion: adhesion becomes significant and dominates the frictional force when there is high surface conformity and the average gap between the contacting surfaces,

defined as the sum of the RMS roughness of the two surfaces, is less than 10 nm [39]. This is indeed observed; by analyzing the wear tracks on the Si wafer, the area of apparent contact was measured at various stages during the non-repeated sapphire-on-Si wafer experiment. The result is plotted in Figure 3.6b alongside the friction measurements in ambient conditions to show that the gradual growth of the area of apparent contact closely tracks that of the frictional force. This interplay between adhesion and the coefficient of friction will be discussed in more detail in **Chapters 5 and 6**.

3.4 Conclusion

Summarizing, the difference between repeated and non-repeated sliding has been studied systematically for various interfaces between non-metallic brittle materials in ambient air conditions. It has been demonstrated that the sliding mode is a very important parameter: Identical systems were shown to give widely varying friction and wear behavior depending on whether the sliding is repeated or non-repeated; for sapphire-on-Si wafer contacts the sapphire wear changed by a factor 6 and the frictional force varied by a factor 2. In the case of SiC-on-Si wafer, the increase in friction observed during a non-repeated experiment was smaller. It is hypothesized that this difference between sapphire and SiC may be explained by the grain structure of the sintered SiC balls, which is not present in the single crystal sapphire balls; such grain structure may enable the SiC balls to maintain a minimum level of roughness that is larger than that of the wafer. Indeed, the worn SiC surfaces are rougher than the worn sapphire surfaces (Figure A.8). An additional important difference between the sapphire and SiC experiments is that, in repeated experiments, the SiO_x third body forms on the ball when a sapphire ball is used but within the Si-wafer wear track when a SiC ball is used, indicating that the wear debris adheres more readily to sapphire than SiC. This difference between sapphire and SiC may again be caused by the surface roughness; since the sapphire surface is smoother than the SiC surface, debris may adhere more readily to the sapphire through physical or capillary adhesion. In fact, we observe that even in some of the non-repeated sapphire-on-Si wafer experiments wear debris can adhere to the sapphire surface (Figure A.2). Indeed those experiments in which we observed this third body formation and the associated running-in behavior, were performed at a slightly higher relative humidity compared to the otherwise identical experiments in which we did not observe running-in. If capillary adhesion is responsible for the

sticking of the wear debris, this correlation could be expected. However, further research is clearly needed in order to investigate and fully explain this phenomenon. The sliding distance required to achieve stable friction in the repeated experiments was also longer for SiC than for sapphire. This difference may be a consequence of the fact that in the SiC experiment, the SiO_x third body needs to form over the entire 20 mm sliding track on the wafer, while in the sapphire experiment it is sufficient to form this SiO_x body only on top of the ball. Furthermore, because in this SiC experiment the third body is immobilized on the wafer rather than on the ball, the ball can be expected to wear more, as observed (Figure 3.2i). It has thus been shown that while repeated sliding steers all systems toward the formation of a third body that stabilizes the friction–which was observed *in situ* for glass-on-glass interfaces–in non-repeated sliding no evidence for such third body formation is found. In all the studied systems, non-repeated sliding leads to a gradual increase of the coefficient of friction with sliding distance. Based on an in-depth analysis of the sapphire-on-Si wafer system, including wear calculations, AFM, contact pressure calculations and dedicated wear experiments, it is proposed here that the mechanism behind the increase in friction with sliding distance is a gradual loss of slider surface roughness that not only increases the (nominally dry) area of real contact, but also leads to more capillary bridges across the interface and potentially allows van der Waals forces to become significant by decreasing the average gap between the surfaces; all of these effects result in higher friction. This interplay between surface roughness, capillarity and the area of real contact is complex, but likely universal since virtually all surfaces are rough and covered by water layers.

Bibliography

[1] Kenneth Holmberg and Ali Erdemir. Global impact of friction on energy consumption, economy and environment. *Fme Trans*, 43(3):181–5, 2015.

[2] Kenneth Holmberg and Ali Erdemir. Influence of tribology on global energy consumption, costs and emissions. *Friction*, 5(3):263–284, 2017.

[3] Wieslaw Grabon, Waldemar Koszela, Pawel Pawlus, and Slawomir Ochwat. Improving tribological behaviour of piston ring–cylinder liner frictional pair by liner surface texturing. *Tribology International*, 61:102–108, 2013.

[4] A Greco, S Sheng, J Keller, and A Erdemir. Material wear and fatigue in wind turbine systems. *Wear*, 302(1-2):1583–1591, 2013.

[5] WR Tyfour, JH Beynon, and A Kapoor. The steady state wear behaviour of pearlitic rail steel under dry rolling-sliding contact conditions. *Wear*, 180(1-2):79–89, 1995.

[6] Marc R Tremblay and Mark R Cutkosky. Estimating friction using incipient slip sensing during a manipulation task. In *[1993] Proceedings IEEE International Conference on Robotics and Automation*, pages 429–434. IEEE, 1993.

[7] David L Luck, Maarten P de Boer, William R Ashurst, and Michael S Baker. Evidence for pre-sliding tangential deflections in mems friction. In *TRANSDUCERS'03. 12th International Conference on Solid-State Sensors, Actuators and Microsystems. Digest of Technical Papers (Cat. No. 03TH8664)*, volume 1, pages 404–407. IEEE, 2003.

[8] Ezequiel Alberto Gallardo-Hernandez and R Lewis. Twin disc assessment of wheel/rail adhesion. *Wear*, 265(9-10):1309–1316, 2008.

[9] Raoul Grönqvist. Mechanisms of friction and assessment of slip resistance of new and used footwear soles on contaminated floors. *Ergonomics*, 38(2):224–241, 1995.

[10] Ravinder S Dahiya, Giorgio Metta, Maurizio Valle, and Giulio Sandini. Tactile sensing—from humans to humanoids. *IEEE transactions on robotics*, 26(1):1–20, 2009.

[11] C Bonnet, F Valiorgue, J Rech, C Claudin, H Hamdi, JM Bergheau, and P Gilles. Identification of a friction model—application to the context of dry cutting of an aisi 316l austenitic stainless steel with a tin coated carbide tool. *International Journal of Machine Tools and Manufacture*, 48(11):1211–1223, 2008.

[12] Andrei Khurshudov and Robert J Waltman. Tribology challenges of modern magnetic hard disk drives. *Wear*, 251(1-12):1124–1132, 2001.

[13] Umberto Celano, Feng-Chun Hsia, Danielle Vanhaeren, Kristof Paredis, Torbjörn EM Nordling, Josephus G Buijnsters, Thomas Hantschel, and Wilfried Vandervorst. Mesoscopic physical removal of material using sliding nano-diamond contacts. *Scientific reports*, 8(1):1–10, 2018.

[14] NN Gosvami, JA Bares, F Mangolini, AR Konicek, DG Yablon, and RW Carpick. Mechanisms of antiwear tribofilm growth revealed in situ by single-asperity sliding contacts. *Science*, 348(6230):102–106, 2015.

[15] Kevin A Laux and Christian J Schwartz. Influence of linear reciprocating and multi-directional sliding on peek wear performance and transfer film formation. *Wear*, 301(1-2):727–734, 2013.

[16] R Ward. A comparison of reciprocating and continuous sliding wear. *Wear*, 15(6):423–434, 1970.

[17] D Odabaş and Ş Su. A comparison of the reciprocating and continuous two-body abrasive wear behavior of solution-treated and age-hardened 2014 al alloy. *Wear*, 208(1-2):25–35, 1997.

[18] IL Singer, SD Dvorak, KJ Wahl, and TW Scharf. Role of third bodies in friction and wear of protective coatings. *Journal of Vacuum Science & Technology A: Vacuum, Surfaces, and Films*, 21(5):S232–S240, 2003.

[19] In-Ju Kim, Richard Smith, and Hisao Nagata. Microscopic observations of the progressive wear on shoe surfaces that affect the slip resistance characteristics. *International Journal of Industrial Ergonomics*, 28(1):17–29, 2001.

[20] Thomas Poiesz, Satish Achanta, Mehmet Ali Akbas, Pavlo Antonov, Jeroen Bouwknegt, Joost Wilhelmus Maria Frenken, Evelyn Wallis Pacitti, Nicolaas

Ten Kate, Bruce Tirri, Jan Verhoeven, et al. Substrate holder and a method of manufacturing a substrate holder, July 21 2020. US Patent 10,719,019.

[21] Fei Deng, Georgios Tsekenis, and Shmuel M Rubinstein. Simple law for third-body friction. *Physical review letters*, 122(13):135503, 2019.

[22] Harold Kahn, Chris Deeb, Ioannis Chasiotis, and Arthur H Heuer. Anodic oxidation during mems processing of silicon and polysilicon: Native oxides can be thicker than you think. *Journal of microelectromechanical systems*, 14(5):914–923, 2005.

[23] Lars Pastewka and Mark O Robbins. Contact between rough surfaces and a criterion for macroscopic adhesion. *Proceedings of the National Academy of Sciences*, 111(9):3298–3303, 2014.

[24] B Weber, T Suhina, T Junge, L Pastewka, AM Brouwer, and D Bonn. Molecular probes reveal deviations from amontons' law in multi-asperity frictional contacts. *Nature communications*, 9(1):1–7, 2018.

[25] A Jenhins Francis and E WHITE Harvey. Fundamentals of optics. *New York: MacGrow-Hill*, 1976.

[26] Lei Chen, Seong H Kim, Xiaodong Wang, and Linmao Qian. Running-in process of si-sio x/sio 2 pair at nanoscale—sharp drops in friction and wear rate during initial cycles. *Friction*, 1(1):81–91, 2013.

[27] Martin H Müser, Wolf B Dapp, Romain Bugnicourt, Philippe Sainsot, Nicolas Lesaffre, Ton A Lubrecht, Bo NJ Persson, Kathryn Harris, Alexander Bennett, Kyle Schulze, et al. Meeting the contact-mechanics challenge. *Tribology Letters*, 65(4):1–18, 2017.

[28] Bharat Bhushan and Xiaodong Li. Micromechanical and tribological characterization of doped single-crystal silicon and polysilicon films for microelectromechanical systems devices. *Journal of Materials Research*, 12(1):54–63, 1997.

[29] Tevis DB Jacobs and Robert W Carpick. Nanoscale wear as a stress-assisted chemical reaction. *Nature nanotechnology*, 8(2):108–112, 2013.

[30] Jingjing Liu, Yijie Jiang, David S Grierson, Kumar Sridharan, Yuchong Shao, Tevis DB Jacobs, Michael L Falk, Robert W Carpick, and Kevin T Turner. Tribochemical wear of diamond-like carbon-coated atomic force microscope tips. *ACS applied materials & interfaces*, 9(40):35341–35348, 2017.

[31] Lei Chen, Jialin Wen, Peng Zhang, Bingjun Yu, Cheng Chen, Tianbao Ma, Xinchun Lu, Seong H Kim, and Linmao Qian. Nanomanufacturing of silicon surface with a single atomic layer precision via mechanochemical reactions. *Nature communications*, 9(1):1–7, 2018.

[32] Tomislav Suhina, Bart Weber, Chantal E Carpentier, Kinga Lorincz, Peter Schall, Daniel Bonn, and Albert M Brouwer. Fluorescence microscopy visualization of contacts between objects. *Angewandte Chemie*, 127(12):3759–3762, 2015.

[33] H Fischer, H Stadler, and N Erina. Quantitative temperature-depending mapping of mechanical properties of bitumen at the nanoscale using the afm operated with peakforce tappingtm mode. *Journal of microscopy*, 250(3):210–217, 2013.

[34] B Weber, T Suhina, AM Brouwer, and D Bonn. Frictional weakening of slip interfaces. *Science advances*, 5(4):eaav7603, 2019.

[35] David B Asay and Seong H Kim. Evolution of the adsorbed water layer structure on silicon oxide at room temperature. *The Journal of Physical Chemistry B*, 109(35):16760–16763, 2005.

[36] Kathryn Hasz, Zhijiang Ye, Ashlie Martini, and Robert W Carpick. Experiments and simulations of the humidity dependence of friction between nanoasperities and graphite: The role of interfacial contact quality. *Physical Review Materials*, 2(12):126001, 2018.

[37] Lei Chen, Chen Xiao, Bingjun Yu, Seong H Kim, and Linmao Qian. What governs friction of silicon oxide in humid environment: contact area between solids, water meniscus around the contact, or water layer structure? *Langmuir*, 33(38):9673–9679, 2017.

[38] M Bazrafshan, MB de Rooij, and DJ Schipper. Adhesive force model at a rough interface in the presence of thin water films: The role of relative humidity. *International journal of mechanical sciences*, 140:471–485, 2018.

[39] Frank W DelRio, Maarten P de Boer, James A Knapp, E David Reedy, Peggy J Clews, and Martin L Dunn. The role of van der waals forces in adhesion of micromachined surfaces. *Nature materials*, 4(8):629–634, 2005.

CHAPTER 4

Tracing single asperity wear in relation to macroscale friction during running-in

The running-in wear of a multi-asperity silicon carbide sphere-on-silicon flat interface is investigated at the micro- and nanoscale in relation to the friction behavior of an unlubricated macroscale tribological system sliding in a unidirectional mode. Experiments and contact simulations indicated that the macroscale friction behavior during running-in was governed by the wear behavior of roughness asperities on the sphere and their influence on the interfacial contact pressure. Specific ploughing tracks on the flat corresponded to individual asperities on the sphere which, when worn-off, led to lower, more stable friction behavior and mild wear at an atomic attrition-like rate. It was also found that single asperity contact simulations are unable to reliably predict multi-asperity friction and wear behavior for this system.

4.1 Introduction

Friction and wear of macroscopic dry sliding contacts are known to have a substantial detrimental impact upon the global energy consumption, economy and environment [1, 2]. As a consequence, this has sparked significant scientific interest, with the aim to manipulate and reduce friction and wear of materials under conditions of industrial relevance [3, 4, 5, 6]. Friction and wear behavior at the macroscopic length scale is typically influenced by the topography of the contacting surfaces [7]. The real area of contact consists of numerous micro- and nanoscale contacts–the result of contacting asperities–that together with the shear strength occurring at these individual contacts, determines the overall friction. The initial surface topography is known to have its greatest effect at the outset of sliding, during the tribological process known as 'running-in' where plastic deformation or fracture of roughness asperities can occur, rather than during the subsequent period [8]. Advancing the scientific understanding of the mechanisms behind the running-in process can lead to optimisation and stabilisation of the working performance of engineering tribosystems, thus extending their lifetime [9]. Running-in can be considered in terms of a collection of macro-, micro-, and nanoscale processes that occur both simultaneously and sequentially [9]. Since these processes occurring on different length scales are all hidden at the contact interface, they are particularly challenging to access experimentally. It is therefore unsurprising that the running-in process is poorly understood.

In order to simplify the tribological system, fundamental studies into the isolated friction and wear events occurring at a single asperity during the onset of dry sliding have attracted considerable attention, with the intention to collectively transform the outcomes into 'multiasperity' level behavior at the macroscale [7, 8, 9, 10, 11, 12, 13, 14, 15, 16, 17]. Single asperities are known to undergo truncation: relatively sharp fresh, unworn surfaces are reduced to a state of surface conformity at the microscale, as a result of the concentrated stresses occurring at the ends of the highest interacting asperities [8]. The running-in friction behavior of the single asperity tribological systems studied by Bhaskaran et al. [12] and Gotsmann et al. [13] (represented graphically as $\mu \propto \sqrt{x}$, where μ = coefficient of friction and x = sliding distance) were characteristic of a dry sliding system where a small amount of surface contamination, oxide or adsorbed species at the interface is quickly worn away to cause a greater degree of adhesion and a rise in friction [9]. In their investigations, the effect of counter surface wear was minimised, and the asperity wear attributed to atom-by-atom attrition [12, 13]. However, when counter surface wear does occur,

as in the case reported by Schiffmann et al. [15] and Yu et al. [16] for reciprocating dry sliding systems, single asperity friction is initially found to be controlled by the ploughing friction component in the first few sliding cycles; transitioning to a regime whereby the elastic or adhesion friction component increases and eventually dominates as the number of cycles increase. The running-in friction behavior in this instance (represented graphically as $\mu \propto \sqrt{\frac{1}{x}}$, where μ = coefficient of friction and x = sliding distance) is characteristic of initially high contact pressures at the sliding interface inducing a rapid transition to the steady state [9]. Bhushan et al. also reported a transition between single asperity ploughing and adhesion friction; noting that with an increase in plastic deformation (ploughing), a greater value of the total coefficient of friction was observed [17]. The transition from ploughing to adhesion friction was attributed to the wear occurring at the interacting apex of the contact asperities. The unexpected wear mechanisms that occur at hard contact asperities in a hard-soft sliding pair, have been observed for several different contact systems and attributed to both atom-by-atom attrition and fracturing [18, 19, 20].

Despite substantial research effort, it remains unclear exactly how the nano-tribological response of a single asperity during the running-in process would, in reality, translate to that of a more industrially-relevant multi-asperity contact interface. Remarks were made by Yu et al. [21] in relation to the similarities in contact pressure beneath some asperities in a multi-asperity system and that of a single asperity system, resulting in similar counter surface wear behavior. However Qi et al. [22] showed that a glass-on-silica system demonstrated opposing trends for single and multi-asperity contacts in relation to the system friction behavior under humid and dry conditions. The combination of the single asperity perspective with a macroscale multi-asperity tribological system has been reported by Krick et al. [23] and Garabedian et al. [24] where single asperity wear was traced at sub-micrometre resolution utilising white light interferometry, to investigate a reciprocated sliding system. The asperity-scale wear behavior was found to mirror that of macroscale wear, with high wear rates detected during the running-in process, transitioning abruptly to ultra-low wear rates once the system had reached the steady state phase [24]. However, no insights into the relationship between the single asperity wear mechanisms and the running-in friction response of the macroscale system were provided. It is conceivable that simply translating the tribological behavior of single asperity systems into that of a multi-asperity system is not so trivial.

The intention of this work is to highlight the relationship between the wear events occurring at single asperities during the onset of dry sliding and the friction response of a multi-asperity tribological system, with hard-soft sliding pairs where

ploughing by the asperities is likely to occur. Investigations into the running-in wear mechanisms of multiasperity contacts are conducted at the micro- and nanoscale, in relation to the friction behavior of a macroscale tribological system dry sliding in a unidirectional mode. Focus is placed on the study of industrially-relevant silicon carbide and silicon materials that are typically found in micro-/nano-electromechanical systems MEMS/NEMS [25]. Experimental methods and elastic-full plastic contact calculations are utilised [26], which enable the study of multi-asperity contacting interfaces with single asperity detail, as the system transitions through the initial running-in stage. The choice to apply a 'unidirectional' sliding mode, where the silicon carbide sphere always encounters a pristine silicon surface throughout the sliding measurement, aims to trace the evolution of the asperity friction and wear whilst minimising the formation of third bodies. The latter are known to influence the friction and wear behavior of this type of tribological system [27].

4.2 Experiments and calculations

4.2.1 Materials

The two industrially-relevant contact materials selected for study were 3 mm diameter direct sintered silicon carbide (SiC) spheres (Grade 10, DIT Holland) and polished p-type single crystal <100> silicon (Si) wafers (University Wafer) with a native oxide layer. The root mean square roughness measured by AFM (scan size 5 μm $\times$ 5 μm) of the pristine multi-asperity SiC sphere and Si flat surfaces were 48.7 nm and 0.9 nm, respectively [27]. The spheres were cleaned prior to use using acetone and isopropanol (Sigma Aldrich) in an ultrasonic bath for 10 min in each solvent; followed by a deionised water rinse. The same cleaning procedure was used for removal of wear debris as indicated.

4.2.2 Methods

The sphere-on-flat tribological experiments were performed using a universal mechanical tester (UMT Tribolab, Bruker), utilising a 'unidirectional' sliding mode as illustrated in Figure 4.1a. An applied load of 100 mN was chosen, with a sliding speed of 0.5 mm/s, a sliding distance per stroke of 20 mm, and a total sliding distance of 40 mm or 6 m in the case of 'short' or 'long' studies respectively. Experiments were performed in an unregulated ambient environment (20–22 °C; 40–60%

relative humidity). Force and position data were acquired at a rate of 5 Hz. Each 6 m sliding experiment was repeated three times with pristine samples, with data presented as a moving average (over two strokes and for the three independent repeat experiments).

To characterize the wear of the contacts, optical focus variation profilometry measurements were performed *ex situ* using a laser scanning confocal microscope (VK-X1000, Keyence). Similarly, the surface topography of the contacts was measured using atomic force microscopy (AFM) (Dimension Icon, Bruker) implemented in tapping mode, using a Si tip with a radius of approximately 8 nm (RTESPA-300, Bruker). Images were processed using Gwyddion software [28], and MATLAB. All reported route mean square (RMS) roughness values for the Si flat were based on AFM scan sizes of 45 μm $\times$ 2.8 μm (1024 $\times$ 64 pixels); and for the SiC sphere were based on the worn area highlighted in Figure 4.1. The wear tracks on the Si flats were additionally imaged and analysed using scanning electron microscopy (Verios 460, FEI) and integrated energy dispersive X-ray spectroscopy (X-Max EDS, Oxford Instruments).

Contact calculations using the Tribology Simulator that is publicly available at `www.tribology.org`, were employed to estimate the plastic deformation at the SiC sphere-on-Si flat interface. The half-space contact calculations were based on the boundary element method (BEM) [26], whereby the elasto-plastic deformation of asperities at the interface was solved. In the calculation, strain hardening is assumed to be negligible, and the contact pressure is limited by the hardness of the softest contact material; Si in this study (Table 4.1). The contact calculations were carried out at 100 mN, utilising height profiles of the SiC sphere measured by AFM (scan size 85 μm $\times$ 85 μm; 4096 $\times$ 4096 pixels), and the mechanical properties listed in Table 4.1 as input. This AFM scan size was chosen to ensure it was considerably larger than the Hertzian contact diameter of $\sim$20 μm under the conditions used.

Table 4.1: Mechanical properties of contact bodies.

Materials	Young's modulus E (GPa)	Poisson's ratio ν	Hardness H (GPa)
SiC sphere	460	0.21	25
Si flat	130	0.2	10

4.3 Results and discussion

4.3.1 Running-in friction and wear response at the macroscale

Figure 4.1 shows the typical running-in friction and wear outcome for unidirectional sliding of a multi-asperity SiC sphere-on-Si flat system over a total distance of 40 mm, demonstrating evidence of counter surface ploughing and hard contact asperity wear. The friction over the 40 mm sliding distance illustrated in Figure 4.1b, shows initially high and irregular behavior with a coefficient of friction (CoF) peak at 0.63 at the onset of sliding, and a relatively sudden decline to a more stable CoF of 0.31 at ∼15 mm. The friction behavior of the system is directly correlated with the appearance and predominant disappearance of abrasive wear tracks on the Si flat (Figure 4.1c); mirroring the total wear track cross-sectional area measured by AFM of tracks 1 and 2, as a function of sliding distance. The behavior of this multi-asperity system, although more erratic, follows the single asperity running-in friction behavior reported elsewhere, where the running-in stage is represented graphically as $y \propto \frac{1}{x}$, where $y =$ CoF and $x =$ sliding distance [15, 16]. This stage is characterised by high initial contact pressures, counter surface wear, and the total friction response being controlled by a ploughing friction component at the onset of sliding, transitioning to a regime whereby the relative contribution from the elastic or adhesion friction component increases and eventually dominates.

Evidence for high initial contact pressures in the multi-asperity system can be found in Figure 4.1c, depicting the presence of ploughing tracks i.e. counter surface wear on the Si flat, and in Figure 4.1e that shows an AFM micrograph of the flattened topography of the hard SiC sphere after sliding 40 mm, suggesting asperity removal over the course of the sliding experiment. These observations are consistent with the calculated reduction in RMS roughness of both contacts after running-in. According to the Hertzian contact pressure at the pristine SiC sphere-on-Si flat interface (∼0.46 GPa), no ploughing should occur as this value is considerably less than the Si flat hardness (Table 4.1). Conversely, the initial Hertzian contact diameter of ∼20 μm, is in line with the experimental observations. Therefore, since roughness asperities are not taken into account in the Hertzian calculation, it can be expected that the initial ploughing tracks and accompanying high friction response are caused by the very high contact pressures exerted beneath the asperities leading to localised plastic deformation of the Si flat at the SiC asperity contact points. The abrupt friction drop suggests asperity removal on the SiC sphere and, similar to the single asperity running-in case, a transition in the friction and wear mechanism from ploughing

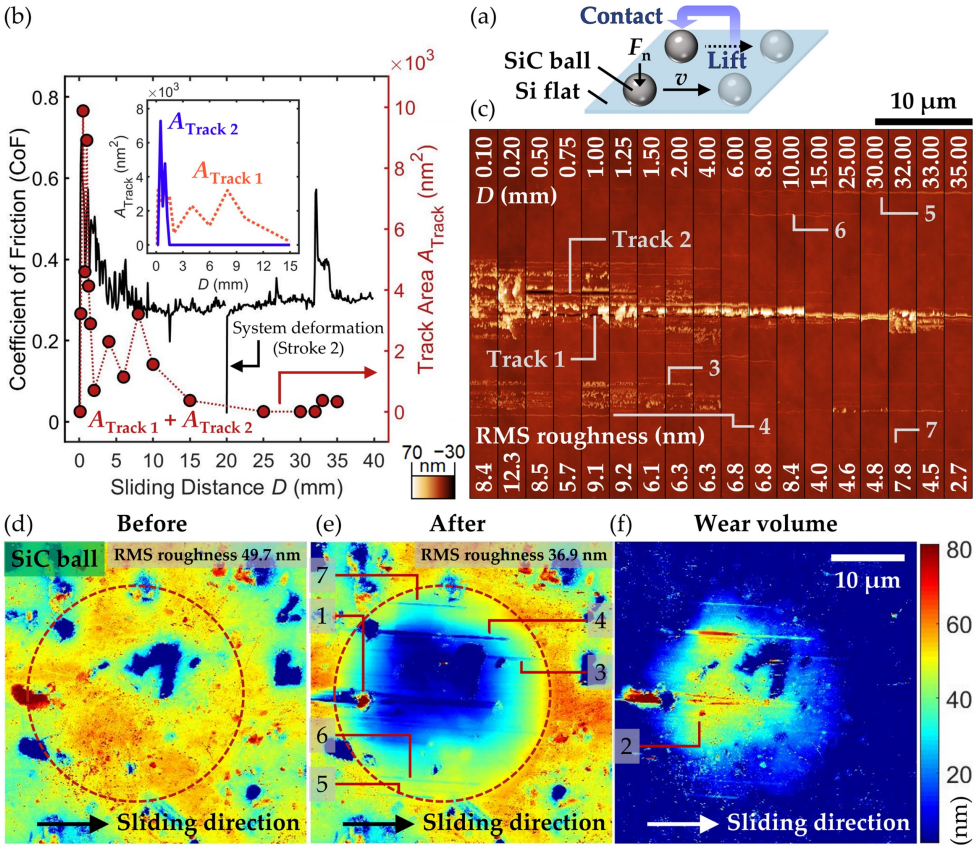

Figure 4.1: Friction and wear analysis for unidirectional sliding of a multi-asperity silicon carbide (SiC) sphere-on-silicon (Si) flat over 40 mm distance: (a) schematic illustration of unidirectional sliding mode. (b) Coefficient of friction (CoF) and total wear track cross-sectional area as a function of sliding distance. Inset figure shows the individual cross-sectional area evolution of wear tracks 1 and 2 as a function of sliding distance. (c) AFM micrographs illustrating the topography of wear tracks on Si flat at set sliding positions. AFM micrographs of SiC sphere (d) prior to sliding, (e) after sliding 40 mm and ultrasonic cleaning. Numbers correspond to possible asperity locations responsible for Si flat wear tracks shown in (c); red circle represents worn area. (f) Wear volume removed (9.48 μm^3) from SiC sphere after 40 mm sliding.

friction and ploughing wear of the Si flat during the running-in process, to adhesion friction and mild wear of both contacts [15]. The evolution of the real interfacial contact pressures of the multi-asperity system will be discussed in more depth later.

Looking in more detail at the ploughing tracks on the Si flat counter surface,

Figure 4.1c shows the AFM micrographs from which the crosssectional areas of tracks 1 and 2 on the Si flat were measured at specific sliding locations. Track 2 can be seen to disappear between 1.25 and 1.5 mm sliding; whilst track 1 still remains after 40 mm. Mounds of Si wear debris (Figure 4.2) can be seen located around (and potentially covering) the ploughing tracks, particularly within the first millimetre of sliding. There also is evidence to suggest increased levels of oxygen in the mounds of Si wear debris, (confirmed from EDS analysis, Figure 4.2e) signifying the presence of SiO_x, as reported previously by Hsia et al. [27]. The precise origin of the SiO_x is not clear from the present study. The SiO_x could occur as a result of mechanochemical activation of the Si in the presence of oxygen and water (ambient conditions), or it could be an accumulation of the native oxide layer from the Si flat at the ploughing track edge, which has been displaced during the sliding experiment.

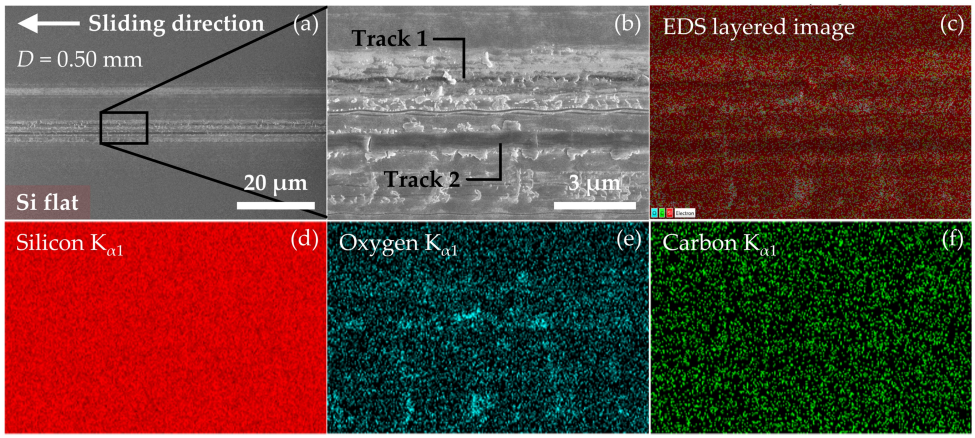

Figure 4.2: SEM micrographs showing (a) width of entire wear track on silicon flat after 0.50 mm sliding; (b) magnified region highlighting wear tracks 1 and 2. Corresponding energy dispersive X-ray spectroscopy of magnified region: (c) layered image displaying the combined Silicon (red), Oxygen (cyan) and Carbon (green) signal; (d) silicon $K_{\alpha 1}$ signal; (e) oxygen $K_{\alpha 1}$ signal; (f) carbon $K_{\alpha 1}$ signal.

4.3.2 Running-in wear response at the asperity-level

In order to provide insight into which asperities on the SiC sphere were responsible for the ploughing tracks found on the Si flat, and into the nature of the wear events occurring at the sliding interface during the running-in process, AFM micrographs detailing the topography the sphere before and after sliding 40 mm were obtained

(Figure 4.1d–f). It is clear that asperities have been removed from the surface of the SiC sphere, evident particularly in Figure 4.1f illustrating the wear volume, which was constructed by calculating the difference between Figure 4.1d and e. The wear rate over the 'short' initial 40 mm sliding distance was calculated to be 2375 $\mu m^3/Nm$. Comparing Figure 4.1c–f, it is possible to identify which asperities on the SiC sphere could be responsible for particular ploughing tracks observed on the Si flat. A dominant asperity located at the trailing edge (the left edge) of the SiC sphere (labelled as 1), is likely responsible for track 1 that remains visible on the Si flat until the end of the 40 mm sliding distance. This asperity appears to evolve from the high feature that lies at the trailing edge of the contact region shown in Figure 4.1d. However, more challenging to locate is the asperity responsible for track 2 shown in Figure 4.1c that ends abruptly after about 1.25 mm sliding. By analysing track distances with respect to one another, and the SiC sphere orientation during sliding, the asperity potentially responsible for creating this track can be found in the SiC wear volume, Figure 4.1f. It is likely that this asperity is not long-lived, given the short wear track it creates on the Si flat and the absence of a clear wear channel on the SiC sphere. Closer inspection of the SiC sphere in fact highlights several wear channels (Figure 4.1e), matching the locations of the four shallower wear tracks on the Si flat: tracks 3–7 (Figure 4.1c). It is plausible that these wear channels on the SiC sphere originate from asperities at the leading edge that have subsequently fractured off and become wear particles trapped at the contact interface between the sphere and the flat, thus interacting with and wearing both surfaces simultaneously along the sliding direction. This sudden fracturing and trapping of asperities could also account for the erratic macroscale friction behavior seen in the first $\sim$7 mm of sliding, after which point the majority of the shallower wear tracks have disappeared.

As the apex of the SiC sphere wears, gradually flattening and thus reducing in height, it is logical to expect that asperities at the very edge of the interface are steadily introduced into the contact area. Evidence for this are tracks 5, 6 and 7 (Figure 4.1c and e), which originate only after several millimetres of sliding. Most prominent is the case of track 7 that appears only during the second sliding stroke. However, the introduction of these asperities into the contact area does not appear to impact the friction response of the macroscale system.

The above experiments and analysis show that the running-in behavior of this multi-asperity system is very similar to the single asperity response [15, 16]. There is evidence of high initial contact pressures and counter surface ploughing, and a transition in the friction and wear mechanism: from the presence of ploughing friction and ploughing wear of the Si flat at the onset of sliding, to a milder wear

of the SiC sphere and a lower, more stable friction response once the majority of asperities have been removed. In order to understand the precise wear mechanisms occurring at the asperities themselves, i.e. whether they fracture off in a brittle manner due to structural defects and the high contact pressure at the onset of sliding, or if they wear in a more gradual fashion such as atom-by-atom attrition [29], further investigation is needed. The presence of wear channels on the SiC sphere as explained above do however suggest that a wear mechanism related to asperity fracturing is more likely during running-in, whereby the fractured asperities could subsequently become third bodies able to interact with both the silicon flat and the SiC sphere.

4.3.3 Running-in contact simulation

To provide additional validation for the proposed relationship between the wear behavior of asperities and the macroscale friction response during running-in, elasto-plastic boundary element method (BEM) calculations were performed using AFM surface topography data in Figure 4.1d and e as input. The intention was to demonstrate the existence of high initial contact pressures, to trace counter surface wear in relation to single asperity ploughing, and to show further evidence for a transition in the friction and wear mechanism after running-in. In general BEM calculations are a reliable method to assess the contact area, according to the 'Contact-Mechanics Challenge' [26]. Figure 4.3 shows the output from BEM calculations of the SiC sphere, illustrating the contact pressure at contacting regions, the area of real contact and average contact pressure prior to and after the running-in period. These calculations reveal that the average contact pressure at the sphere-on-flat interface prior to sliding is high (7.7 GPa)–at least one order of magnitude greater than the Hertzian contact pressure of the system when the surface roughness is not taken into account. In comparison to the sphere condition after running-in, a greater number of contacting asperities prior to sliding exert a contact pressure at the interface high enough to plastically deform the counter surface ($\geq$10 GPa; see Table 4.1 for Si flat hardness). A distinct transition is demonstrated by the BEM calculation, whereby after running-in, the number of contact points (and the area of real contact) has evidently increased (Figure 4.3d and e), yet the contact pressure at the interface has decreased below 10 GPa at almost every contacting position (Figure 4.3b). A notable exception is the dominant asperity located at the trailing edge of the SiC sphere, clearly visible in Figure 4.3b and c exhibiting a contact pressure $\geq$10 GPa. This finding reinforces the experimental observation that this single asperity is likely responsible for counter

surface ploughing track 1, and emphasises the good agreement that exists between experiment and calculation. The high feature in Figure 4.1d that develops into SiC asperity '1' is also visible in Figure 4.3a and d, but with fewer contact points exerting a pressure $\geq$10 GPa, indicating that the feature becomes a more dominant ploughing asperity as the sphere surface evolves. The exact regions of the sphere in Figure 4.3a that exceed a contact pressure of 10 GPa and could therefore contribute to the formation of ploughing tracks 2–7 on the Si flat, are more challenging to trace. However, there appears a good agreement between the density of the high contact pressure points on the SiC sphere and regions of excess wear debris on the counter surface in Figure 4.1c at distance 0.10 mm.

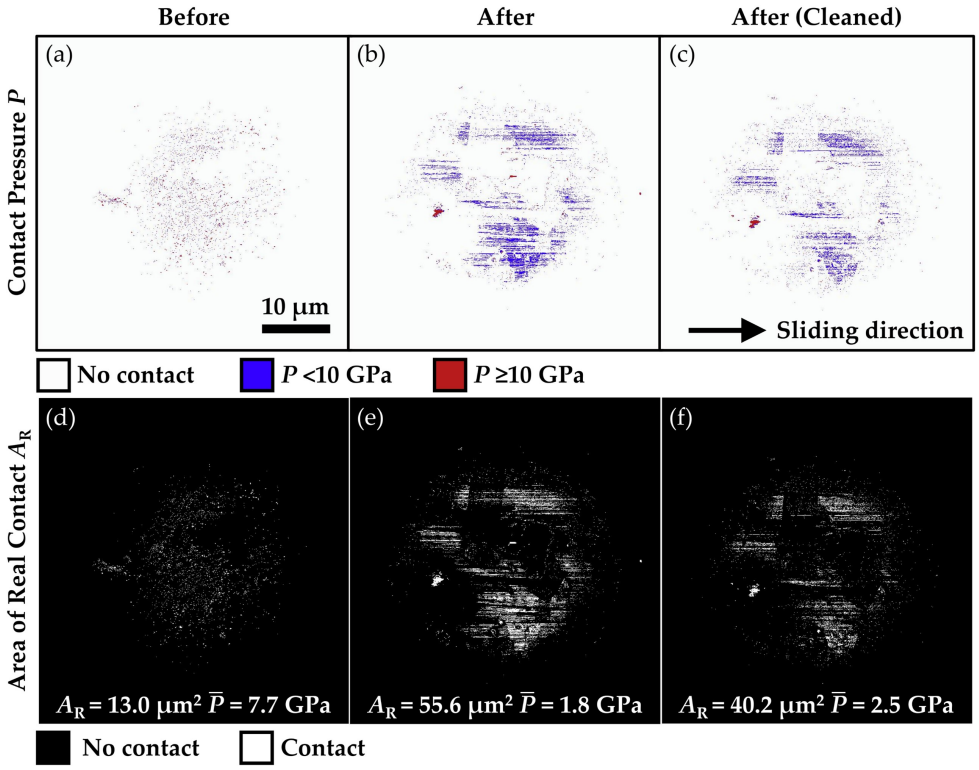

Figure 4.3: Boundary element method (BEM) calculations of silicon carbide sphere prior to sliding; after sliding 40 mm; and after sliding and ultrasonic cleaning to illustrate: (a–c) the contact pressure ($\overline{P}$) at contacting regions on the sphere; (d–f) the area of real contact (A_R) and resulting average contact pressure ($\overline{P}$). In all cases a normal force of 100 mN is applied.

Further utilisation of BEM calculations to trace counter surface wear in relation to single asperity ploughing is displayed in Figure 4.4. It shows SEM and AFM micrographs of the Si flat at the beginning and end of the 40 mm unidirectional sliding experiment, and corresponding BEM calculations (utilising AFM surface topography data in Figure 4.1d and e as input) predicting the numerical values for the plastic deformation depth (d) into the Si flat, resulting from indentation of the asperities on the harder SiC sphere and assuming a plastic yield stress of 10 GPa for the Si flat. Qualitatively, there appears to be a good agreement between the experimentally-derived asperity positions and those predicted by the BEM calculations to show the plastic deformation on the Si flat; with the width of the wear track at the beginning and end of the sliding experiment also matching closely. However, quantitatively, the correspondence between experiment and model is poor, as the raw numerical values for the plastic deformation depth predict initial ploughing tracks approximately 20 nm deep (Figure 4.4c), which clearly were not observed experimentally (Figure 4.4b). Reasons for this discrepancy will be discussed in more detail in the following section.

A further discrepancy between the BEM predictions and the experimental observations is highlighted when the approximate projected ploughing contact area A_{pr} of each asperity in the sliding direction calculated using the BEM (and displayed in Figure 4.4c and f), is used to provide a rough estimate of the expected ploughing force. Ploughing friction F_{pl} for a collection of 'single asperities' can be estimated from the total projected area of contact in the sliding direction with which the asperities plastically penetrate a substrate A_{pr}, multiplied by the hardness of that substrate H_{Si} [30]. The following expression can therefore be used to estimate the CoF due to ploughing at the beginning and end of the 40 mm unidirectional sliding experiment, where F_{n} is the applied normal force of 100 mN:

$$\mathrm{CoF} = \frac{F_{\mathrm{pl}}}{F_{\mathrm{n}}} = \frac{A_{\mathrm{pr}} H_{\mathrm{Si}}}{F_{\mathrm{n}}} \tag{4.1}$$

Using this relationship, the calculated CoF resulting from the plastic deformation of the Si flat is 0.16 at the onset of sliding, decreasing to 0.12 at the end of the 40 mm unidirectional sliding experiment. Quite clearly there is a large discrepancy between the calculated CoF and the experimental observations, indicating that the reality of the multiasperity tribological system is much more complex than that based on ploughing of a collection of individual 'single asperities'.

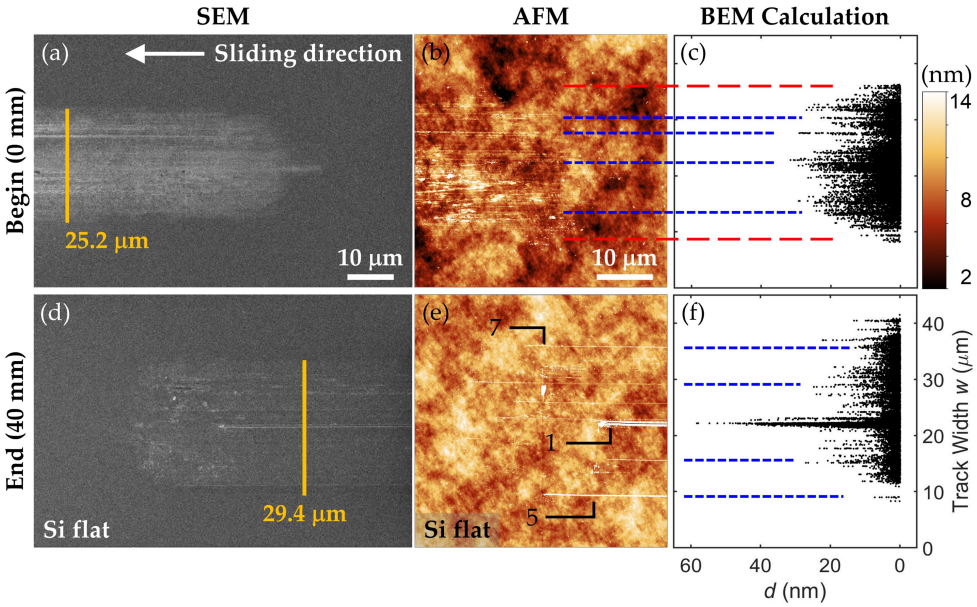

Figure 4.4: Tracing silicon (Si) flat wear in relation to silicon carbide (SiC) sphere asperity ploughing prior to and after sliding 40 mm: (a), (d) SEM micrographs of Si flat wear track; (b), (e) AFM micrographs of Si flat wear track. Numbers correspond to possible SiC asperities shown in Figure 4.1e and f, assigned responsible for resulting Si flat wear tracks. (c), (f) Boundary element method (BEM) calculations of SiC sphere illustrating the plastic deformation depth (d) of asperities into Si flat.

4.3.4 Discrepancy between experiment and contact simulation

In order to interpret the quantitative differences between the BEM (and ploughing friction) calculation and the experimental results, the running-in friction and wear behavior of the system is separated into two stages: (i) Onset of sliding after 0.075 mm (where CoF_{max} occurs); (ii) Post running-in at 40 mm.

Considering stage (i) at the onset of sliding or running-in, where the CoF rises to 0.63 after 0.075 mm in the dynamic friction regime, the CoF ought to be predicted by the BEM calculation as this stage is dominated by ploughing friction. However, the CoF calculated by the BEM (0.12) is notably lower than the experimentally derived value. This discrepancy is attributed to the topographical evolution particularly of the Si flat that cannot be captured by the BEM calculation. The high measured

CoF at the onset of sliding is accredited to ploughing of the expanding Si surface, including the generation, smearing and compression of Si wear debris. In order to verify this reasoning, the ploughing tracks on the Si flat were examined in more detail. SEM and AFM micrographs show that the wear tracks–depicted by regions of light grey and white on the Si flat respectively–are in fact elevated with respect to the background (Figure 4.4a, b, d and e). This may be attributed to the formation of SiO_x from Si that has been displaced within the wear tracks. The Pilling-Bedworth (PB) ratio is the ratio of the volume of an oxide to the volume of the metal from which the oxide forms [31]. For oxidation of Si to SiO_2, the PB ratio is approximately 2 [32], meaning that the volume of SiO_2 is twice that of Si, and so effectively causes the volume of material within the wear track to increase. Such an effect cannot be determined by the BEM calculation and potentially explains why the BEM-predicted ploughing tracks of $\sim$20 nm deep (Figure 4.4c) were not observed experimentally. However, if the ploughing asperities are at the trailing edge of the sphere, as is the case for those responsible for creating tracks 1 and 2 in Figure 4.1, they can generate ploughing tracks that are elevated at the edges but have a centre that is below the background height level of the Si flat. This indicates that with such a 'trailing edge ploughing track', the debris collects next to the track, while other ploughing tracks are potentially covered over. According to the BEM calculations, many of the asperities on the SiC sphere do not result in plastic deformation, but instead exert a contact pressure onto the Si flat that is below the material hardness (Figure 4.3) where asperities elastically deform the Si flat. Such asperities can compress the ploughing debris and displace it back into the ploughing track if they come into contact with a track directly after it is formed. This concept is particularly evident in the magnified SEM image in Figure 4.2b that shows the elevated wear track, compressed debris and the two distinct 'trailing edge ploughing tracks'.

Further evidence for a high CoF arising as a consequence of ploughing the (elevated) Si surface is shown in Figure 4.5. It depicts the friction behavior of double-stroke 'non-repeated' SiC sphere-on-Si flat friction experiments [27], in which each sliding cycle of the sphere consists of one back-and-forth stroke before the sphere is stepped to a fresh area on the Si flat. Figure 4.5 clearly shows that the 'backward' stroke sliding over the previously worn track produces a higher frictional force than the 'forward' stroke. However, this only occurs during the first 20–25 cm of sliding, when ploughing friction is prominent in the backward stroke. This observation therefore suggests that in such experiments, more ploughing occurs during the backward stroke than the forward stroke. This may seem counterintuitive, as one would not expect ploughing tracks created during the forward stroke to be ploughed

again in the backward stroke. However, the observation by SEM and AFM of elevated ploughing tracks suggests that greater ploughing may occur during the backward stroke because the sharpest asperities on the sphere (including asperities that might have otherwise only elastically deformed the flat) will be in contact with this elevated material, thereby penetrating deeper and ploughing over a larger cross section. In fact, it is likely that the aforementioned scenario is already taking place during the forward stroke, when trailing-edge asperities on the SiC sphere slide over the (compressed and elevated) ploughing tracks created by leading-edge asperities. For a single asperity ploughing system, the situation is likely much simpler. The frictional force would tend to decrease with the backward stroke, as the single asperity is unlikely to encounter elevated or compressed material as it retraces the ploughing track created during the forward stroke, therefore experiencing less resistance [15, 16]. As the BEM can only predict the total CoF in the absence of wear debris and expanded material, the calculated result at stage (i) understandably underestimates the experimental result.

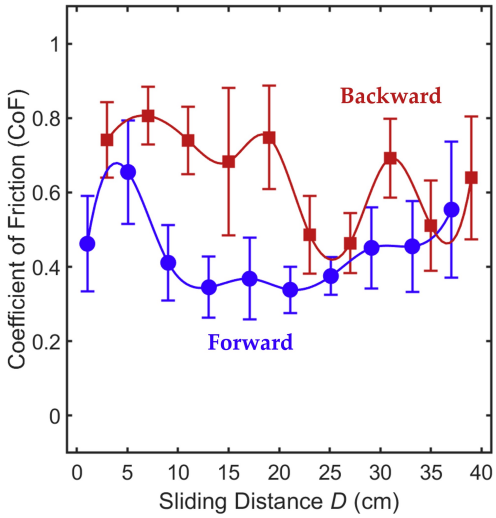

Figure 4.5: Coefficient of friction for double stroke 'non-repeated' experiment of a multi-asperity silicon carbide sphere-on-silicon flat over 40 cm sliding distance. All experimental conditions (excluding the sliding mode) identical to that of unidirectional sliding experiment described in this work [27].

At stage (ii) post running-in at 40 mm, the majority of asperities on the SiC sphere have been removed, and the system has transitioned to one likely dominated by adhesion friction and mild wear of the SiC sphere, where the effect of ploughing as

discussed in stage (i) is largely absent except for that generated by trailing edge SiC asperity '1'. The CoF calculated by the BEM (0.21) for the end of the 40 mm unidirectional sliding experiment similarly significantly underestimates the experimentally determined value (0.31). The BEM calculation cannot account for the possible effect wear particles trapped at the sliding interface may have upon the plastic deformation of the Si flat and resulting frictional forces. As mentioned above, these wear particles likely originate from asperities at the leading edge of the SiC sphere that have fractured off in the initial sliding strokes, becoming trapped at the contact interface and thus interacting with and wearing both surfaces simultaneously. Evidence for the existence of these wear particles can be found in Figure 4.3e and f. The real area of contact on the SiC sphere appears to decrease after cleaning, suggesting that loose and dynamic wear particles were in fact present at the sliding interface. The absence of wear particle dynamic effects is likely to lead to a discrepancy in the calculated CoF, given that the BEM calculations are limited only to one 'snapshot in time'. In addition, the calculated CoF is based only on ploughing friction, and neglects any adhesion friction contribution. The latter is the likely dominating friction mechanism in this regime, originating from smaller interfacial gaps and thus increased area of real contact and lower interfacial contact pressure due to asperity removal, as highlighted by Figure 4.3 [27]. Therefore, as the BEM can only partially predict the total CoF, the calculated result at stage (ii) unsurprisingly underestimates the experimentally derived value.

The details presented here highlight that the friction and wear behavior of a multi-asperity tribological system is much more complex than that of a single asperity system during the running-in process. The BEM can qualitatively predict the locations of the ploughing tracks on the counter surface based upon asperity locations on the sphere, but it cannot predict the degree of plastic deformation of the flat or the resulting frictional force due to ploughing. Further work is required in order to fully understand the reasoning behind this quantitative discrepancy, but qualitatively it is evident that the evolution of the counter-surface material (material expansion, compression, trapped wear debris) plays an important role in the friction response of the multiasperity system. This emphasises the challenges of predicting the friction and wear behavior of multi-asperity systems on the basis of single asperity contact simulations and scaled-up single asperity system behavior.

4.3.5 Evolution of friction and wear response after running-in at the macroscale

To understand how the friction and wear behavior of the multi-asperity SiC-sphere-on-Si flat system evolves after the initial running-in process, a longer unidirectional sliding study over 6 m was conducted. Figure 4.6a shows running-in CoF behavior equivalent to the 40 mm sliding study (Figure 4.1b). And consistent with the work reported in [27], for 'non-repeated' reciprocated sliding of brittle non-metallic materials, a steady increase in the CoF is observed over a sliding distance of 6 m. As is highlighted by Figure 4.6b–e, the worn contact area of the SiC sphere appears flattened and smoother than the pristine surface, suggesting continuous asperity removal over the course of the 6 m sliding experiment. The wear rate for this system during the running-in process (as presented in Figure 4.1) was found to be more than three times that of the overall wear rate for the extended 6 m unidirectional sliding study (700 $\mu m^3/Nm$), providing additional evidence for a transition in the friction and wear mechanism after running-in.

Thus it is likely that the overall steady increase in CoF over the 6 m sliding is not due exclusively to continual asperity ploughing but more conceivably a consequence of adhesion friction following asperity removal, and a gradual increase in area of real contact [27]. This is supported by SEM observations of the wear track on the Si flat. The SEM micrograph inset in Figure 4.6a illustrates the topography of the final wear tracks on the Si flat after 6 m sliding and shows no evidence of abrasive wear (unlike the initial sliding track in Figure 4.6f) and that the track width has increased to $\sim$60 μm. An estimation can be made to illustrate the potential for adhesion friction and mild wear mechanisms such as atom-by-atom attrition in this multi-asperity tribological system using the method proposed by Hsia et al. [27]. This method, without considering strain hardening, is based on the consideration that for rough surfaces, due to asperity-level plastic deformation, the contact pressure in the contact can never become greater than the hardness of the softest material, in this case the Si flat. This sets a minimum limit on the real area of contact, A_{min}. Thus, the minimum number of atoms (inferred as an area, A_{min}) on the SiC sphere in contact with the Si flat at any one time during the 6 m unidirectional sliding experiment can be estimated as follows:

$$A_{min} = \frac{F_n}{H_{Si}} = 1.0 \times 10^{-11}\ m^2 \approx \frac{1.0 \times 10^{-11}}{(2.0 \times 10^{-10})^2} = 2.5 \times 10^8\ atoms \qquad (4.2)$$

where F_n is the applied normal force (100 mN), H_{Si} is the Si flat hardness (10 GPa) and 2 Å is an approximate atom-to-atom distance. Over the whole area of the contact,

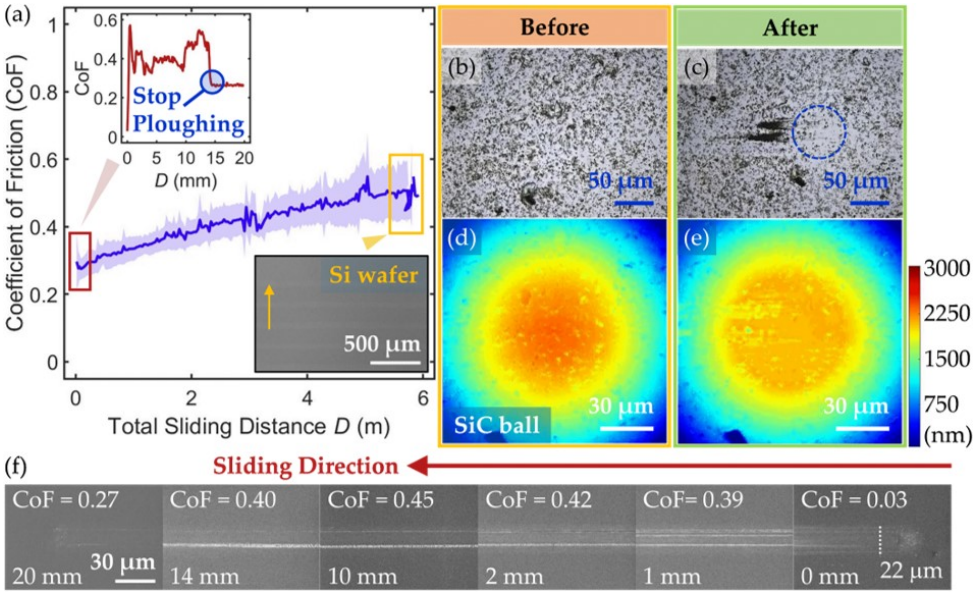

Figure 4.6: Friction and wear analysis for unidirectional sliding of a multi-asperity silicon carbide (SiC) sphere-on-silicon (Si) flat over 6 m distance: (a) coefficient of friction (CoF) as a function of sliding distance (solid blue line represents moving average CoF; shaded area represents standard deviation). Upper inset figure shows variation in CoF over initial sliding stroke; Lower inset figure shows SEM micrograph of final wear tracks on Si flat after 6 m sliding. Optical microscopy image of SiC sphere (b) prior to and (c) after sliding. Height profile of SiC sphere (d) prior to and (e) after sliding, measured by optical profilometry (see **Chapter 2**). (f) SEM micrographs of Si flat showing wear track evolution over initial sliding stroke.

2.5×10^8 atoms on the SiC sphere surface must touch and slide over the Si flat at any time. Thus, using the total wear volume (4.2×10^{-16} m^3) measured from the height profile in Figure 4.6e, it is possible to estimate the number of atoms removed from the SiC sphere surface over the 6 m sliding distance and thus the average distance required to remove one atomic layer:

$$\frac{4.2 \times 10^{-16}}{(2.0 \times 10^{-10})^3} \approx 5 \times 10^{13} \; atoms \text{ removed} \tag{4.3}$$

$$\frac{6 \text{ m} \times 2.5 \times 10^8}{5 \times 10^{13}} \approx 30 \; \mu\text{m} \tag{4.4}$$

This approximation indicates that the atoms on the SiC surface that make contact

with the Si flat slide an average of at least 30 μm (a distance that is equivalent to more than one hundred thousand atomic spacings) before one atomic layer is worn off. As there is evidence to suggest plastic deformation of the Si flat and asperity removal on the SiC sphere and thus a higher wear rate during the running-in process, the above calculation is likely to underestimate the mildness of the subsequent wear occurring at the SiC sphere-on-Si flat interface. This in itself provides additional support for atom-by-atom wear [10, 33], and adhesion friction being the dominant mechanism once the ploughing-asperity removal transition point has occurred.

As for the nature of the atomic attrition-like wear mechanism, it is plausible that a mechanochemical process is occurring at the SiC sphere-on-Si flat interface. As a unidirectional sliding mode was used, the SiC sphere continuously made contact with 'fresh' unworn native oxide layer on the Si flat. The bond energies (enthalpies) of the native oxide layer Si–O (452 kJ/mol), O–H (459 kJ/mol) and any potentially formed interfacial bonds O–C (358 kJ/mol) are all greater than that of Si–C (318 kJ/mol) [34]. Therefore, the probability that a Si–C bond would break before an O–H or Si–O, or indeed any interfacial O–C bonds, is higher. Hence, chemically, there is a preference for the removal of atoms one-by-one from the SiC sphere–which is in essence atomic attrition [10, 33].

4.4 Conclusion

The running-in wear mechanisms of multi-asperity contacts were investigated at the micro- and nanoscale in relation to the friction behavior of a macroscale tribological system sliding in a unidirectional mode. Focus was placed upon the study of industrially-relevant silicon carbide and silicon materials; systems with a Hertzian contact pressure less than that of the hardness of the contacting bodies. Experimental methods and contact simulations were combined in order to study the multi-asperity interfaces at a level of detail of a single asperity, as the system transitioned through the initial running-in stage. The resulting friction response of such a tribological system was found to be initially high and erratic at the onset of sliding, with a rapid decline to a stabilised coefficient of friction after $\sim$15 mm running-in period. Thereafter, the coefficient of friction was observed to increase relatively steadily over a total sliding distance of 6 m.

A direct correlation was found between the friction behavior from 0 to 15 mm, the appearance and disappearance of ploughing tracks on the flat, and the simultaneous removal of asperities on the sphere. It was understood that the macroscale

friction response during the running-in period was likely dominated by ploughing wear at a high wear rate, originating from the very high contact pressure exerted beneath the asperities at the sphere-on-flat interface. The behavior observed for this multi-asperity system, although more erratic, followed that of single asperity running-in friction behavior reported in the literature. Contrary to a single asperity system however, the evolution of the countersurface material (material expansion, compression, trapped wear debris), was found to play a dominant role in the friction response of the multi-asperity system; emphasising the challenges associated with potential scale-up theories.

A transition point in the wear mechanism of the multi-asperity system appeared to occur once the majority of asperities were removed. In line with the steady increase in friction observed over the remaining 6 m; the average contact pressure at the interface was seen to decrease, thus lowering the wear rate as the real area of contact gradually increased. On average the rate of material removal was very low, occurring at an atomic attrition-like rate that is potentially attributed to adhesive wear involving mechanochemical reactions on an atomic scale. Overall, the friction behavior of this multi-asperity brittle non-metallic tribological system appears to be governed by the wear behavior of the asperities, and the influence their existence has upon the interfacial contact pressure.

Bibliography

[1] Kenneth Holmberg and Ali Erdemir. Global impact of friction on energy consumption, economy and environment. *Fme Trans*, 43(3):181–5, 2015.

[2] Kenneth Holmberg and Ali Erdemir. Influence of tribology on global energy consumption, costs and emissions. *Friction*, 5(3):263–284, 2017.

[3] Wieslaw Grabon, Waldemar Koszela, Pawel Pawlus, and Slawomir Ochwat. Improving tribological behaviour of piston ring–cylinder liner frictional pair by liner surface texturing. *Tribology International*, 61:102–108, 2013.

[4] WR Tyfour, JH Beynon, and A Kapoor. The steady state wear behaviour of pearlitic rail steel under dry rolling-sliding contact conditions. *Wear*, 180(1-2):79–89, 1995.

[5] David L Luck, Maarten P de Boer, William R Ashurst, and Michael S Baker. Evidence for pre-sliding tangential deflections in mems friction. In *TRANSDUCERS'03. 12th International Conference on Solid-State Sensors, Actuators and Microsystems. Digest of Technical Papers (Cat. No. 03TH8664)*, volume 1, pages 404–407. IEEE, 2003.

[6] A Greco, S Sheng, J Keller, and A Erdemir. Material wear and fatigue in wind turbine systems. *Wear*, 302(1-2):1583–1591, 2013.

[7] Pantcho Stoyanov and Richard R Chromik. Scaling effects on materials tribology: from macro to micro scale. *Materials*, 10(5):550, 2017.

[8] Peter J Blau. *Friction science and technology: from concepts to applications*. CRC press, 2008.

[9] Peter J Blau. On the nature of running-in. *Tribology international*, 38(11-12):1007–1012, 2005.

[10] Tevis DB Jacobs and Robert W Carpick. Nanoscale wear as a stress-assisted chemical reaction. *Nature nanotechnology*, 8(2):108–112, 2013.

[11] Kai Zhao and Ramin Aghababaei. Interfacial plasticity controls material removal rate during adhesive sliding contact. *Physical Review Materials*, 4(10):103605, 2020.

[12] Harish Bhaskaran, Bernd Gotsmann, Abu Sebastian, Ute Drechsler, Mark A Lantz, Michel Despont, Papot Jaroenapibal, Robert W Carpick, Yun Chen, and Kumar Sridharan. Ultralow nanoscale wear through atom-by-atom attrition in silicon-containing diamond-like carbon. *Nature nanotechnology*, 5(3):181–185, 2010.

[13] Bernd Gotsmann and Mark A Lantz. Atomistic wear in a single asperity sliding contact. *Physical review letters*, 101(12):125501, 2008.

[14] MG Reitsma, RG Cain, S Biggs, and DW Smith. Wear of a single asperity using lateral force microscopy. *Tribology Letters*, 24(3):257–263, 2006.

[15] Kirsten I Schiffmann and Andreas Hieke. Analysis of microwear experiments on thin dlc coatings: friction, wear and plastic deformation. *Wear*, 254(5-6):565–572, 2003.

[16] Jiaxin Yu, Hailong Hu, Fei Jia, Weifeng Yuan, Hongbin Zang, Yong Cai, and Fang Ji. Quantitative investigation on single-asperity friction and wear of phosphate laser glass against a spherical afm diamond tip. *Tribology International*, 81:43–52, 2015.

[17] Bharat Bhushan and Michael Nosonovsky. Comprehensive model for scale effects in friction due to adhesion and two-and three-body deformation (plowing). *Acta materialia*, 52(8):2461–2474, 2004.

[18] Gianluca Roscioli, Seyedeh Mohadeseh Taheri-Mousavi, and Cemal Cem Tasan. How hair deforms steel. *Science*, 369(6504):689–694, 2020.

[19] Andrei G Khurshudov, Koji Kato, and Hiroyuki Koide. Wear of the afm diamond tip sliding against silicon. *Wear*, 203:22–27, 1997.

[20] Patrick C Fletcher, Jonathan R Felts, Zhenting Dai, Tevis D Jacobs, Hongjun Zeng, Woo Lee, Paul E Sheehan, John A Carlisle, Robert W Carpick, and William P King. Wear-resistant diamond nanoprobe tips with integrated silicon heater for tip-based nanomanufacturing. *ACS nano*, 4(6):3338–3344, 2010.

[21] Bingjun Yu, Hongtu He, Lei Chen, and Linmao Qian. Tribological behavior of monocrystalline silicon from single-to multiple-asperity scratch. *Wear*, 374:29–35, 2017.

[22] Huimin Qi, Wen Hu, Hongtu He, Yafeng Zhang, Chenfei Song, and Jiaxin Yu. Quantitative analysis of the tribological properties of phosphate glass at the nano-and macro-scales. *Friction*, 9(5):1138–1149, 2021.

[23] Brandon A Krick, Jennifer R Vail, Bo NJ Persson, and W Gregory Sawyer. Optical in situ micro tribometer for analysis of real contact area for contact mechanics, adhesion, and sliding experiments. *Tribology letters*, 45(1):185–194, 2012.

[24] NT Garabedian, A Bhattacharjee, MN Webster, GL Hunter, PW Jacobs, AR Konicek, and DL Burris. Quantifying, locating, and following asperity-scale wear processes within multiasperity contacts. *Tribology Letters*, 67(3):1–10, 2019.

[25] Bharat Bhushan. Nanotribology and nanomechanics of mems/nems and biomems/bionems materials and devices. *Microelectronic Engineering*, 84(3):387–412, 2007.

[26] Martin H Müser, Wolf B Dapp, Romain Bugnicourt, Philippe Sainsot, Nicolas Lesaffre, Ton A Lubrecht, Bo NJ Persson, Kathryn Harris, Alexander Bennett, Kyle Schulze, et al. Meeting the contact-mechanics challenge. *Tribology Letters*, 65(4):1–18, 2017.

[27] Feng-Chun Hsia, Fiona M Elam, Daniel Bonn, Bart Weber, and Steve E Franklin. Wear particle dynamics drive the difference between repeated and non-repeated reciprocated sliding. *Tribology International*, 142:105983, 2020.

[28] David Nečas and Petr Klapetek. Gwyddion: an open-source software for spm data analysis. *Open Physics*, 10(1):181–188, 2012.

[29] Rodrigo A Bernal and Robert W Carpick. Visualization of nanoscale wear mechanisms in ultrananocrystalline diamond by in-situ tem tribometry. *Carbon*, 154:132–139, 2019.

[30] RW Liefferink, B Weber, and D Bonn. Ploughing friction on wet and dry sand. *Physical Review E*, 98(5):052903, 2018.

[31] NB Pilling. The oxidation of metals at high temperature. *J. Inst. Met.*, 29:529–582, 1923.

[32] Tomoki Matsuda, Kota Inami, Keita Motoyama, Tomokazu Sano, and Akio Hirose. Silver oxide decomposition mediated direct bonding of silicon-based materials. *Scientific reports*, 8(1):1–10, 2018.

[33] Jingjing Liu, Yijie Jiang, David S Grierson, Kumar Sridharan, Yuchong Shao, Tevis DB Jacobs, Michael L Falk, Robert W Carpick, and Kevin T Turner. Tribochemical wear of diamond-like carbon-coated atomic force microscope tips. *ACS applied materials & interfaces*, 9(40):35341–35348, 2017.

[34] RB King, RH Crabtree, CM Lukehart, DA Atwood, and RA Scott. Bond energies. *Encyclopedia of Inorganic Chemistry*, pages 1–4, 2006.

CHAPTER 5

Rougher is more slippery

Friction originates at the area of real contact which depends on the (changing) surface topography. Observing and measuring the area of real contact at multi-asperity interfaces is difficult, making it challenging to quantitatively study the interplay between the frictional force and surface topography. In this paper, we systematically manipulate surface topography and use a fluorescence microscopy-based contact visualization technique to reveal this interplay. We demonstrate good agreement between elasto-plastic boundary element method contact calculations and experimental visualization of the area of real contact. While the area of real contact and thus contact pressure could be varied by a factor of 4 through control of the surface topography, this had only a modest effect on the coefficient of friction (CoF). We do find a small but systematic increase in the proportionality constant between frictional force and normal force (CoF) with decreasing surface roughness. The observation that smoother surfaces have a greater CoF is due to capillary adhesion between the two surfaces. We quantitatively model this behavior using a simple capillary adhesion model without adjustable parameters. Our results provide quantitative insights into the interplay between contact mechanics, friction, and capillary adhesion. A predictive understanding of this interplay is essential to demanding applications such as precision positioning.

5.1 Introduction

Friction is one of the most common natural phenomena. Around 2 million years ago, in the Middle Paleolithic period, our ancestors used the phenomenon to make fire [1]. Nowadays, friction is responsible for a large fraction of global energy consumption [2]. At almost all macroscopic interfaces, the force of friction (F_f) is proportional to the normal force (F_n) [3, 4, 5, 6, 7, 8, 9]; the ratio of the two forces is constant and known as the coefficient of friction (CoF $= \frac{F_f}{F_n}$). Single contact experiments and simulations have demonstrated that the proportionality between frictional force and normal force can emerge because increased normal force results in stronger atomic scale interlocking and thus proportionally more frictional force [10, 11, 12]. Alternatively, if the atomic scale interlocking is dominated by adhesion rather than by externally applied force, the frictional force may scale with the area of real contact [10, 12]. At macroscopic, multi-asperity interfaces, the contacting materials form asperity contacts and touch at the atomic scale within the area of real contact [11, 13]. Analytical theories such as the classical Greenwood and Williamson model [14] and the Persson contact theory [15] describe the process of contact formation. They attempt to explain why the area of real contact is proportional to the normal force, relating this to the surface topography, mechanical properties, and in some cases adhesion [16, 17, 18]. Alternatively, contact between rough surfaces can be understood through boundary element calculations and molecular dynamics simulations [16, 18, 19, 20]. However, these theoretical approaches toward describing multi-asperity contact formation are built on assumptions–such as idealized elasticity and plasticity or frictionless contacts–that do not necessarily hold in reality [6]. The area of real contact is elusive and difficult to access experimentally because it is hidden from view [21, 22] by the contacting materials and defined by the deformation of small-scale surface roughness variations. Therefore, it is challenging to compare multi-asperity contact theories to experiments at the appropriate length scales and even harder to assess the impact of the contact mechanics on friction [23]. As a result, a key question remained unanswered: to what extent does adhesive multi-asperity friction really depend on the area of real contact?

Here, we use a fluorescence microscopy-based contact visualization method to reveal the local nanometric gaps at a multi-asperity interface. Through a detailed comparison between visualization experiments and boundary element contact calculations, we show that the observed deformations of nanoscale surface roughness are well-described by idealized elasto-plasticity. We show that a direct consequence of the contact mechanics is that the area of real contact will increase when the surface

roughness is decreased and decrease when the roughness is increased. Counterintuitively, the surface roughness and area of real contact almost do not influence the dynamic frictional force: smooth and rough surfaces have approximately the same CoF. However, when the interface roughness drops to values of just a few nanometers, we do find an increased CoF due to the large areas across which the interface is subject to capillary adhesion forces. These measurements give a comprehensive picture of how surface topography, elasto-plasticity, and adhesion control the friction of multi-asperity contacts.

5.2 Experiments and calculations

5.2.1 Contact visualization

In the contact visualization experiments, a rheometer (DSR 301, Anton Paar) was placed on top of an inverted laser scanning confocal microscope (Axiovert 200M, Zeiss) with an LSM 5 PASCAL (Zeiss) laser scanning module (Figure 5.1a). A 3.18 mm Si_3N_4 ball was fixed to the rheometer and brought into contact with the sapphire flat (22 mm diameter), which was mounted on the microscopy sample stage. A droplet of fluorescent liquid 3,6-bis((2-ethylhexyl)oxy)-1,2,4,5-tetrazine was placed between the Si_3N_4 sphere and sapphire flat.

A 514 nm laser light was used to excite the fluorescent molecules. The fluorescence images were recorded using a $63\times$ 1.4 numerical aperture objective (Plan-Apochromat, Zeiss) at a pixel size of $\sim$3400 nm^2. At the interface, the fluorescent molecules were excited by the laser light, and the local fluorescence intensity scales linearly with the local gap [24]. Figure B.1 in the Appendix B shows the fluorescence intensity measured across two orthogonal profiles that run through the center of the sphere-on-flat contact. To conduct these measurements, the Si_3N_4 sphere was placed on the sapphire flat with no externally applied load-only gravitational force. Therefore, the deformation of the bulk sphere was negligible. The predicted sphere-on-flat gap, assuming there is no roughness and no contact deformation, is shown by the black solid and dotted curves in Figure B.1a in the Appendix B. We subtracted the finite background fluorescence intensity. We find a linear relation between the intensity and the gap $<$500 nm in both orthogonal in-plane directions (Figure B.1b in the Appendix B). The intensity-gap proportionality constant can be found by averaging the slope of the linear fitting lines on two intensity directions.

5.2.2 BEM contact calculation

Contact calculations are carried out by the Tribology Simulator that is publicly available at `www.tribology.org`. The half-space contact calculations were based on the BEM to estimate the elasto-plastic deformation (strain hardening is neglected) at the Si_3N_4 sphere-on-sapphire flat interface, where the input mechanical properties in the calculation are listed in Table B.1 in the Appendix B. The best match between experiment and calculation was obtained when the calculated contact image was convolved with the microscopy point spread function, and subsequently, a gap threshold of 9 nm was set (Figure 5.2). This is 3 nm larger than the gap used to obtain the experimental value of the contact area; the difference is of the order of the molecule size. We hypothesize that the difference may therefore be related to the inability of the fluorescent liquid molecules to fill the smallest gaps or the quenching of the fluorescence of the boundary layer molecules that interface to the solid surfaces. Nonetheless, we want to emphasize that the presented comparison between contact calculation and experiment provides an unprecedented level of detail.

5.2.3 Friction experiments

The Si_3N_4 sphere-on-sapphire flat friction experiments were performed using a customized rheometer setup (DSR 301, Anton Paar) placed in an ambient environment at ∼40% RH (Figure 5.1a). The 3.18-mm-diameter Si_3N_4 sphere was slid against the sapphire flat at a constant angular velocity ($\omega = 8.3 \times 10^{-5}$ rad/s) that can be converted into a constant sliding speed by multiplication with the fixed rotation radius ($r = 12.98$ mm); $V = \omega r = 1$ μm/s. The torque (τ) experienced while sliding was measured and converted to the frictional force ($F_f = \frac{\tau}{r}$). Si_3N_4 spheres and sapphire flats were cleaned by sonicating with isopropanol solution and kept in an ambient environment before friction experiments. The friction experiments were performed at different normal forces indicated in Figure 5.3b with different Si_3N_4 sphere topographies. The maximum normal force applied in the experiment was 160 mN, which results in a Hertzian contact pressure of ∼0.6 GPa. The Hertzian contact pressure is much lower than the hardness (Table B.1 in the Appendix B) of Si_3N_4 and sapphire so that the chance of plastic deformation and ploughing was minimized. In addition, in Figure B.4 in the Appendix B, we demonstrate the AFM topography of a Si_3N_4 sphere before and after the contact with a sapphire flat at 2 N normal force. At these elevated normal forces, we do observe some plasticity. To

correct for possible tilting of the rheometer with respect to the substrate, we slid the Si_3N_4 sphere on the sapphire flat both in the positive and negative directions and reported the average frictional force measured in both directions under the same applied normal force. For each normal force, the sliding strokes were performed at a previously untouched piece of the sapphire flat to prevent potential interaction of the contact surfaces and wear debris [25]. The frictional force at each normal force was measured at least three times (six times in both directions) by following the applied normal force sequence: increase, decrease, then increase. No hysteresis was observed, confirming that wear was minimized.

5.2.4 Contact stiffness measurement and calculation

The normal contact stiffness measurements were conducted using the same experimental setup as described above. The fluorescence intensity was averaged within the Hertzian contact area (A_{Hertz}) between the Si_3N_4 sphere and sapphire flat at different normal forces:

$$A_{\text{Hertz}} = \pi\left(\frac{3F_{\text{n}}R}{4E_{\text{eff}}}\right)^{\frac{2}{3}} \tag{5.1}$$

where R (= 1.59 mm) is the radius of Si_3N_4 sphere and $E_{\text{eff}} = \left(\frac{1-\nu_1}{E_1} + \frac{1-\nu_2}{E_2}\right)^{-1}$ is the effective modulus of Si_3N_4 (labeled as 1) and sapphire (labeled as 2). The mechanical properties of Si_3N_4 and sapphire are listed in Table B.1 in the Appendix B. The average fluorescence intensity (a.u.) was converted to a gap value (nm) by using the intensity-gap calibration as discussed above. Contact stiffness calculations were done using the BEM. The Si_3N_4 sphere topography was measured by laser scanning confocal microscopy (VK-X1000, Keyence) with a pixel size of $\sim 76 \times 10^3$ nm^2. The average gap values were based on the interfacial gap map output by the BEM calculation at normal forces between 30 and 160 mN with $S_{\text{q}} = 47.1$ nm ($S_{\text{k}} = 0.23$) sphere (blue triangle symbol) and 30–120 mN with $S_{\text{q}} = 99.3$ nm ($S_{\text{k}} = 0.45$) sphere (red square symbol) in Figure 5.5 and see Experiments 5.2.5 for surface topography characterization in more detail. In Figure B.6 in the Appendix B, we report the contact stiffness calculated for the roughest sphere in the absence of plasticity. As the sharp asperity peaks are not flattened plastically under these conditions, the interface is much more compliant.

5.2.5 AFM surface topography characterization

The surface topography characterization was performed using AFM (Dimension Icon, Bruker) in tapping mode. Power spectral density analysis of the topographies are presented in Figure B.3 in the Appendix B. A silicon AFM tip with an apex of ∼8 nm radius (RTESPA-300, Bruker) was used and replaced for each topography measurement. We quantified the surface roughness either through the root mean square (RMS) height variation (S_q = 99.3–4.7 nm) or through the RMS surface slope (S_k = 0.45–0.06) and the power spectral density (Figure B.3 in the Appendix B) [26], measured by AFM over an area of 10 μm × 10 μm with a pixel size of 95.4 nm^2.

5.3 Results

In our experiments, a customized rheometer pressed a 3.18-mm-diameter Si_3N_4 sphere against a sapphire flat plate at millinewton to Newton normal forces (Figure 5.1). The Si_3N_4 sphere was chosen because it has a similar hardness (23 GPa) to sapphire (20 GPa), enabling elastic contact up to very high contact pressures and minimizing wear at the interface. To determine the area of real contact, we recorded fluorescence images of the interface using laser scanning confocal microscopy through the transparent sapphire substrate [27]. A droplet of low-viscosity fluorescent liquid 3,6-bis((2-ethylhexyl)oxy)-1,2,4,5-tetrazine [28] was placed in between the Si_3N_4 sphere and sapphire flat before the normal force was applied. The large contact pressure associated with Si_3N_4-on-sapphire contacts (GPa) in combination with the viscosity [29] of the fluorescent liquid (2000 Pa s) ensured that viscous effects did not contribute to the transmission of the contact force at the experimental time scale (>1 s), as found previously [27]. If the local interfacial gap is large enough to host a liquid molecule (∼3 nm in size), an increased fluorescence intensity results. The relation between local interfacial gap and fluorescence intensity can be calibrated such that the local gap can be measured with nanometer accuracy (see Experiments 5.2.1 for more details) [24]. Combined with the submicrometer in-plane imaging resolution, fluorescence microscopy reveals the multi-asperity contacts as no other technique can.We find that fluorescence images of the Si_3N_4-on-sapphire contacts indeed display a clear peak in the intensity distribution at low but nonzero fluorescence intensities (Figure B.2 in the Appendix B), corresponding to the area of real contact. Both detector noise and the convolution of contact and noncontact regions lead to the finite intensity measured at the area of real contact; pixels may contain a mixture of contact and no contact. To extract the area of real contact, we set an

intensity threshold at a value that corresponds to an average gap of 6 nm. Figure 5.2 shows that the area of real contact in the experiment increases with the normal force, as the asperities and bulk materials are being deformed. To compare these experimental observations with theoretical predictions of the contact formation process, we also performed contact calculations using the boundary element method (BEM) [19] (see Experiments 5.2.2). Based on the sphere surface topography [measured using atomic force microscopy (AFM)] and the elasto-plastic properties of Si_3N_4 and sapphire (Table B.1 in the Appendix B), the simulator solves the elastic equations and permits idealized plastic flow to relax the local contact pressure to values below the material hardness. Despite these idealizations of the contact problem, we find a compelling match between theory and experiment; not only does the predicted contact area correspond to what we observe experimentally, but individual contact patches revealed by fluorescence microscopy are reproduced by the calculations. This indicates that elasto-plasticity is the key ingredient required to describe the Si_3N_4-on-sapphire contact mechanics at the length scales that can be resolved by our inverted confocal fluorescence microscope.

A direct consequence of the elasticity of the asperities is that the area of real contact depends on the topography of the contacting surfaces; the smoother the surfaces become, the larger the area of real contact. To investigate the interplay between roughness and contact area deeper, we compared Si_3N_4 spheres with different surface roughness as prepared by abrasion or polishing. Subsequently, we used the measured topographies to perform BEM contact calculations (such as shown in the inset of Figure 5.3a) to quantify Areal for each sphere roughness at various normal forces. As shown in Figure 5.3a, we find that there is a linear relation between the area of real contact and the normal force for each sphere. As expected, the area of real contact increases with decreasing surface roughness at the same normal force; the smoothest sphere makes contact over an area that is $\sim$4 times larger than the area of real contact associated with the roughest sphere. To investigate if the larger area of real contact also leads to a larger frictional force, we carried out dry friction experiments with the Si_3N_4 spheres with varying surface roughness (see Experiments 5.2.3). The rough-on-smooth contact geometry ensures that ploughing and interlocking friction are suppressed. We find that, despite the significant impact the roughness has on the contact mechanics (Figure 5.3a), the variation in CoF is quite modest (Figure 5.3b). Reducing the area of real contact increases the interfacial normal stress and the interfacial shear stress such that the CoF varies much less than the contact pressure. This behavior contrasts with the classical description of friction by Bowden and Tabor [12] in which the frictional force is proportional to the area of

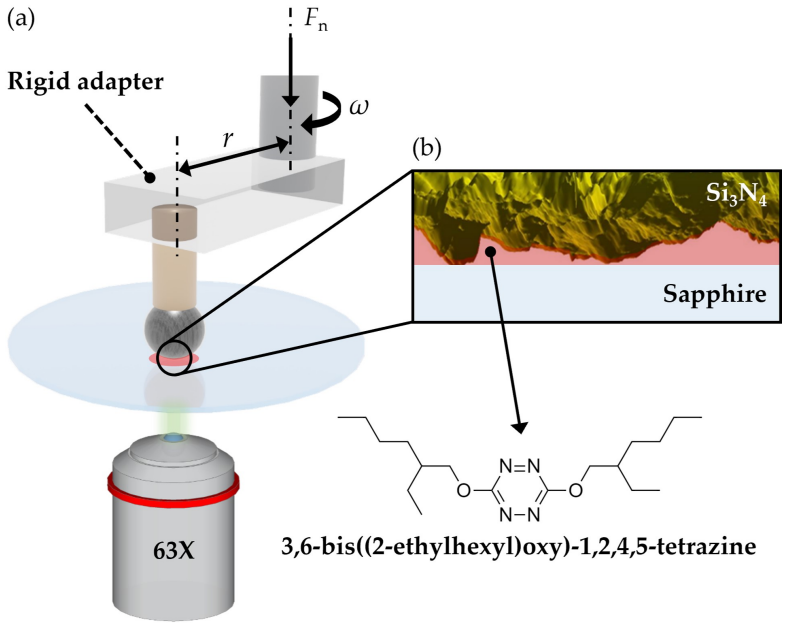

Figure 5.1: Experimental setup. (a) A rheometer is mounted on top of an inverted confocal microscope. Via a rigid adapter, the rheometer controls the movement of a Si_3N_4 sphere in contact with a sapphire flat. The sapphire flat has a root mean square roughness (S_q) of 0.14 nm, measured by atomic force microscopy (AFM) over an area of 10 μm $\times$ 10 μm (95.4 nm^2 per pixel). By lowering and rotating the rheometer, a normal force (F_n) is applied at the Si_3N_4-on-sapphire interface, and the torque (τ) is measured. In the contact visualization experiment, the contact is wetted with a droplet of fluorescent liquid, as shown in (b), where the inset illustrates the structure of the fluorescent liquid 3,6-bis((2-ethylhexyl)oxy)-1,2,4,5-tetrazine. The fluorescent molecules are excited by 514 nm laser light, and the fluorescence intensity at the interface is measured by the microscope (63$\times$ magnification with 1.4 numerical aperture)

real contact. Proportionality between interfacial normal stress and interfacial shear stress has previously been observed in surface force apparatus experiments [10] and atomistic simulations [11, 30] and is in fact expected for stiff materials such as those used in the present experiments [12]. However, when averaged over the measured normal forces, the average CoF does show a small but systematic dependence on the surface roughness of the sphere (Figure 5.3b inset).

To elucidate the observed relation between surface roughness and CoF, we considered the contact calculations presented in Figure 5.3 and analyzed these calculations in terms of the interfacial regions across which the gap between the two surfaces is

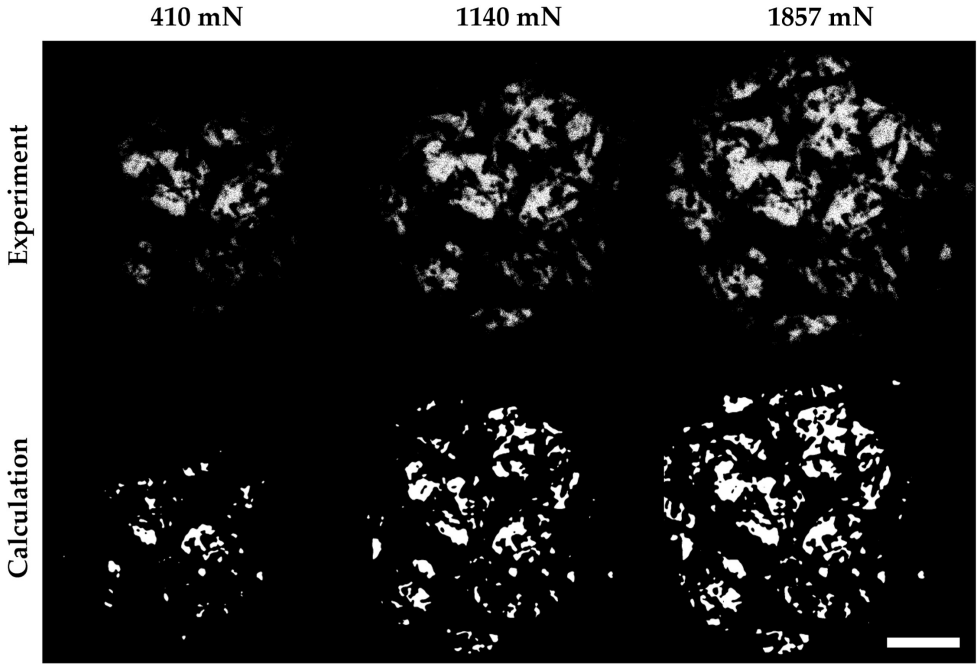

Figure 5.2: Si_3N_4-on-sapphire contact visualization and calculation. Upper row, area of real contact (white patches), defined as the pixels within which the average gap is smaller than 6 nm, for three values of the normal force. Bottom row, the area of real contact (white patches) calculated by the Tribology Simulator based on the topography of the sphere used in the experiments as measured by atomic force microscopy (AFM; 60 μm $\times$ 60 μm, $2 \times 10^3 \text{nm}^2$ per pixel). The results of the contact calculation were convolved with the microscopy point spread function: a Gaussian function with full width at half maximum of 600 nm. Scale bar, 20 μm.

finite but small enough for adhesive interactions to take place. Since the experimental interfaces were in ambient air, the surfaces were likely covered by water layers that can form capillary bridges around contact points [31]. The work of adhesion associated with capillarity [32, 33] can be as high as two times the water surface tension ($2\gamma_{\text{water}} = 145\ \text{mJ/m}^2$), far above the work of adhesion associated with van der Waals interactions, which in turn decreases when the solid-on-solid interface is partially wetted by water [34]. The typical interfacial gap across which capillary bridges can be formed under thermodynamic equilibrium conditions is given by $W = 2t + d_c$. Here, t is the equilibrium thickness of the water film condensed at a free silicon oxide (SiO_x) surface (0.7 nm at 20% relative humidity (RH) and 1.1 nm at

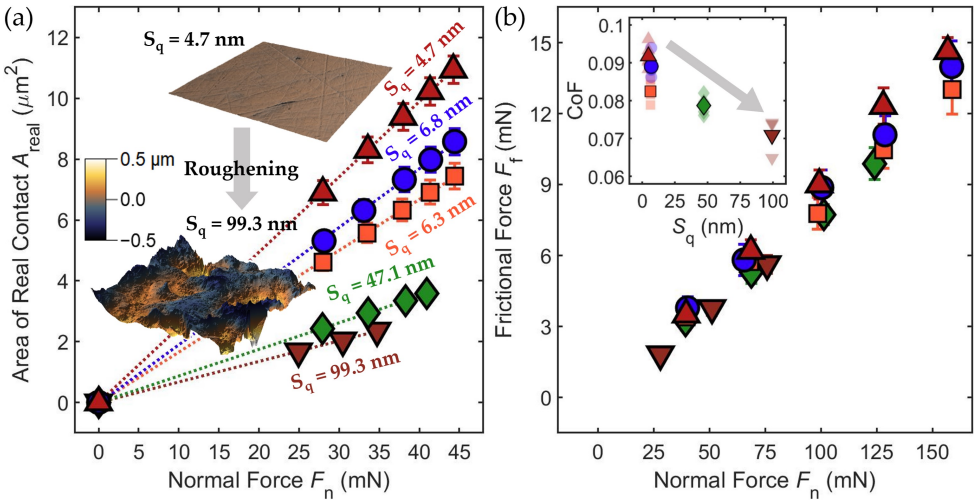

Figure 5.3: Area of real contact and frictional force as a function of normal force and surface topography. (a) Calculated area of real contact (A_{real}) as a function of normal force (F_{n}) for Si_3N_4 spheres of varying roughness. The insets highlight 10 μm $\times$ 10 μm (95.4 nm^2 per pixel) atomic force microscopy (AFM) topographies of the smoothest sphere ($S_{\text{q}} = 4.7$ nm) and the roughest sphere ($S_{\text{q}} = 99.3$ nm). (b) The frictional force (F_{f}) was measured at different normal forces (F_{n}) for the same spheres used in (a). The coefficient of friction (CoF), averaged over the measured normal forces, is plotted in the inset. Contact calculations (a) were performed at normal forces up to 45 mN to ensure that the nominal pressure in the calculations remained like that in the experiment (b). The error bars cover one standard deviation of the results.

50% RH [35]), and d_{c} is the critical distance between two surfaces at which capillary condensation occurs according to the Kelvin-Tolman equation [36] [1.5 nm at 20% RH and 2.5 nm at 50% RH (Table 5.1)]. This yields interface gaps between 2.8 nm (20% RH) and 4.8 nm (50% RH). A schematic illustration of the capillary bridges formed at the interface is shown in the inset of Figure 5.4a. There indeed is a dramatic increase in the area of the interface within which the surfaces are separated by a finite gap that is <4.8 nm (gray area Figure 5.4b) as the surface roughness decreases, suggesting that capillary adhesion may play a role in the observed dependence of the frictional force on the surface roughness.

Inspired by previous work [37], we now present a simplified model in which capillary adhesion occurs within gaps at the interface <4.8 nm, as illustrated by the gray areas in Figure 5.4b. In our model, we solely account for the capillary adhesion force and ignore other contributions to the adhesion such as the tension force and

Table 5.1: Equilibrium thickness (t) of the water condensate on a free SiO_x surface and critical distance for capillary condensation (d_c) of water as a function of relative humidity (RH) as extracted from the literature [34, 35].

***RH* (%)**	***t* (nm)**	**d_c (nm)**
20	0.65	1.49
50	1.11	2.54

the van der Waals force. The capillary bridges at the interface are characterized by a positive radius of curvature (r_1) in the in-plane direction and a negative radius of curvature (r_2) in the direction normal to the hydrophilic interface. Because $|r_1| \gg |r_2|$ (see Figure 5.4b), the overall radius of curvature of the capillary bridges $\frac{1}{R_{\text{overall}}} = \frac{1}{r_1} + \frac{1}{r_2}$ is negative and dominated by r_2 such that a negative Laplace pressure difference between the water inside the bridges and the surrounding air leads to an adhesive force at the interface [34, 36]. The Laplace pressure (P_{Laplace}) is given by $P_{\text{Laplace}} = \frac{\gamma_{\text{water}}}{r_2+\delta}$, with γ_{water} the bulk water surface tension, $r_2 = \frac{-d_c}{2}$, and δ the Tolman length ($\delta = 0.2$ nm at 20–50% RH) [36]. Hence, the total adhesion force (F_{ad}) in our model is given by the product of the Laplace pressure difference across the water-air interface and the area on the sphere (A_{cap}) that is wetted by the capillary water (Figure 5.4b); $F_{\text{ad}} = P_{\text{Laplace}} \times A_{\text{cap}}$. The capillary adhesion force associated with the modeled interface can therefore be calculated–without adjustable parameters–based on literature values for the water layer thickness on the free SiO_x surface, the critical distance for capillary condensation, the water surface tension, and the Tolman length. Through our model, we obtain capillary adhesion forces in the range of 3.9–14.5 mN for the smoothest interface to 0.03–0.2 mN for the roughest interface between 20% RH and 50% RH.

The capillary adhesion–which is particularly strong for the smooth interface–contributes to the externally applied load (F_{ex}) and is balanced by the repulsive force (F_{rep}) generated at the solid-on-solid contacts: $F_{\text{rep}} = F_{\text{ex}} + F_{\text{ad}}$. As illustrated by the results in Figure 5.3, the frictional force is proportional to the applied normal force. Therefore, the relative increase in frictional force resulting from capillary adhesion should scale as $\frac{F_{\text{ad}}}{F_{\text{ex}}}$. This ratio is close to zero for the roughest sphere: $\frac{F_{\text{ad}}}{F_{\text{ex}}} = 6 \times 10^{-3}$. We thus can express the expected increase in CoF due to capillary adhesion (CoF_{ad}) in terms of the CoF measured using the roughest sphere ($\text{CoF}_{\text{roughest}}$):

$$\text{CoF}_{\text{ad}} = \text{CoF}_{\text{roughest}} \times (1 + \frac{F_{\text{ad}}}{F_{\text{ex}}}) \tag{5.2}$$

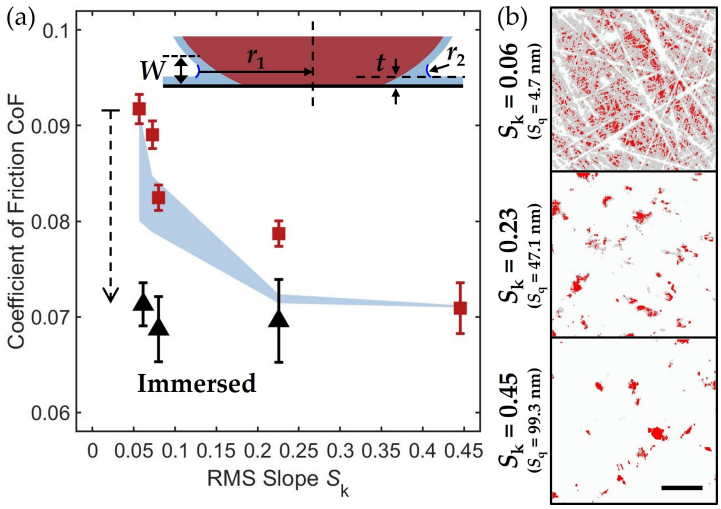

Figure 5.4: Coefficient of friction (CoF) as a function of surface slope and the effect of capillary adhesion. (a) Si_3N_4-on-sapphire CoF (red square symbols) as measured using spheres with different topographies as a function of average root mean square (RMS) surface slope (S_k) of sphere surfaces as measured by atomic force microscopy (AFM). The gray shaded area shows the CoF values predicted by Equation 5.2 for relative humidities ranging from 20 to 50%. The black triangles indicate the CoF measured when the interface is immersed in water. The inset illustrates the formation of the capillary bridges at the multi-asperity interface. (b) Calculated contact areas at an externally applied normal force (F_{ex}) of 35 mN for three different Si_3N_4 spheres with RMS slopes ranging from 0.06 (top) to 0.45 (bottom). The red and gray patches indicate solid-solid contact area and capillary-wetted area, respectively. The error bar covers the RMS variation between independent results. Scale bar, 2.5 μm.

It is important to note that just like the area of real contact, the area within which capillary adhesion contributes to the loading of the interface can be expected to scale with the normal force. Therefore, adhesion effectively results in a change in coefficient of friction rather than in a finite frictional force measured at zero applied normal force. Implicit in this calculation is the assumption that our thermodynamic equilibrium estimate of the capillary force holds during low-velocity rough-on-smooth sliding. Our simple adhesion model is thus used to predict the surface topography dependence of the CoF. The parameters that go into our model are not adjustable; the topography is measured by AFM, the BEM contact calculations are based on the elasto-plastic properties of Si_3N_4 and sapphire, and the capillary

adhesion range and Laplace pressure are estimated based on the Kelvin-Tolman equation and based on previous measurements [35]. We evaluate the model for RHs in the typical range for lab experiments (RH = 20–50%) and plot the results in Figure 5.4a. The predicted CoF (CoF_{ad})–without adjustable parameters–quantitatively captures the dependence of the CoF on surface roughness: smoother interfaces display higher frictional force due to capillary adhesion. As capillary adhesion can only take place in the presence of solid, liquid, and gas phases, we further challenge our model by immersing the contacts in liquid water. This removes the air from the contact zone, preventing capillary bridges from forming. Indeed, this results in a CoF that is no longer dependent on the surface roughness (Figure 5.4a), confirming our model. We want to emphasize that this provides direct evidence that all dependence of the CoF on the area of real contact in ambient conditions can be attributed to capillary effects and that, therefore, the experiments and model provide indirect evidence that the shear stress depends linearly on the normal stress (Figure B.5 in the Appendix B).

While our results demonstrate how surface topography affects dynamic friction through capillary adhesion, the impact of surface topography on static friction remains an important open question. The transition from static to dynamic friction [38, 39, 40] is of key importance to, for instance, the initiation of earthquakes or the precision and accuracy of positioning systems and microelectromechanical system or nanoelectromechanical system actuators. A loaded interface subjected to an increasing tangential force will initially deform elastically before the interfacial junctions yield. However, the asperity-scale deformations associated with this presliding process are typically difficult to assess experimentally. Nonetheless, the tangential interface stiffness that determines the initial elastic response of an interface to an increasing tangential force is predicted to be proportional to the normal stiffness of the interface [41]. The combination of experiments and contact calculations employed in this paper enables a direct measurement of this normal interfacial stiffness as a function of surface topography. In the contact calculations discussed above, we extracted the average interfacial gap (Gap) as a function of the normal force and derived the normal interfacial contact stiffness (k) using Hooke's law, $k = \frac{F_n}{\text{Gap}}$. In these calculations, we only consider the roughness of the Si_3N_4 sphere, as the RMS roughness of the sapphire plate is two orders of magnitude smaller. Rougher interfaces–higher S_q or S_k of Si_3N_4 sphere-on-sapphire flat–have a lower interfacial stiffness than smooth interfaces. The results show that the normal contact stiffness strongly depends on the RMS roughness of the sphere surface (Figure 5.5). Since the contact pressure for most spheres is below the hardness of the contacting materials

(see also Figure B.6 in the Appendix B), the contact stiffness is determined by the elasticity of the long wavelength roughness of the surface. The fluorescence imaging of the experimental interface provides an additional opportunity to measure the average interfacial gap as a function of normal force, through the average interfacial fluorescence intensity (Figure 5.5; see also Experiments 5.2.4). The contact stiffness measured in the visualization experiments agrees with the contact calculations and is far beyond the stiffness of most mechanical measurement devices.

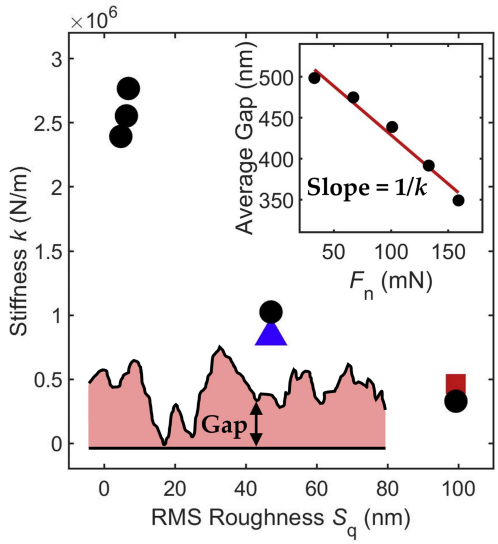

Figure 5.5: Normal contact stiffness as a function of surface roughness. Black circular symbols indicate boundary element method (BEM) contact calculations based on the sphere topographies. The blue triangle and red square symbols indicate measurements using the contact visualization method. The measured average gap at the multi-asperity interface (an example is shown in the bottom left inset) is shown in the upper right inset as a function of normal force (F_n). For the smoothest interfaces, the average gaps become comparable with the size of the fluorescent molecules ($\sim$3 nm), and the visualization experiments can no longer reliably measure interface stiffness.

5.4 Discussion

In conclusion, we demonstrated that the Si_3N_4-on-sapphire frictional force is not proportional to the area of real contact; the CoF reflects a proportionality between normal stress and shear stress. By controlling the surface topography, we varied the

area of real contact between a Si_3N_4 sphere and flat sapphire surface by a factor of four and found a much weaker but systematic variation in CoF of ∼20%. This 20% variation of the CoF with surface roughness was found to be caused by capillary adhesion; the smoother the interface, the larger the area across which capillary adhesion can contribute to the load experienced by the contacting asperities. Our simple adhesion model, based on the Laplace and Kelvin-Tolman equations and without adjustable parameters, successfully predicts the adhesion-induced increase in the CoF with decreasing surface roughness for RHs in the range of 20–50%. This large range of humidity reflects that the model can capture the experimental trend regardless of the precise thickness of the pre-absorbed water film, which may vary for different hydrophilic surfaces.In the calculations, the contact angle at the three-phase contact line is ignored; considering a non-zero contact angle for the hydrophilic (oxidized) Si_3N_4 and sapphire surfaces would result in a small decrease in the range of the capillary adhesion but would not affect the overall trend of increasing CoF for decreasing surface roughness. The solid-on-solid friction measured in the experiments may be affected by boundary layers of water and/or airborne hydrocarbons from the environment. Since the only material-specific parameters included in our model are the bulk elasto-plastic properties, the model can in principle be applied to any stiff hydrophilic interface. Interfaces between materials with lower stiffness have been shown to display a more complex interplay between adhesion and friction [37, 42]. While our microscopy and AFM-based approach does not enable the measurement of surface roughness at length scales smaller than that of the AFM tip [43], we conclude that the resolution is sufficient to capture the mechanism by which topography controls friction [44, 45]: capillary adhesion. In addition to showing that dynamic friction at such interfaces is largely independent on surface roughness, we also show that the elastic deformations that play an important role in controlling the initial response of an interface to external loading are highly roughness dependent; the interfacial stiffness was shown to change by almost an order of magnitude as the RMS slope varied from 0.06 to 0.45 (corresponding to RMS roughness range of 5–100 nm). These results provide insight into how friction behavior evolves as surface roughness is worn off, which is paramount in precision positioning applications.

Bibliography

[1] Wil Roebroeks and Paola Villa. On the earliest evidence for habitual use of fire in europe. *Proceedings of the National Academy of Sciences*, 108(13):5209–5214, 2011.

[2] Kenneth Holmberg and Ali Erdemir. Influence of tribology on global energy consumption, costs and emissions. *Friction*, 5(3):263–284, 2017.

[3] Ian M Hutchings. Leonardo da vinci's studies of friction. *Wear*, 360:51–66, 2016.

[4] Elena Popova and Valentin L Popov. The research works of coulomb and amontons and generalized laws of friction. *Friction*, 3(2):183–190, 2015.

[5] C Mathew Mate and Robert W Carpick. *Tribology on the small scale: a modern textbook on friction, lubrication, and wear*. Oxford University Press, USA, 2019.

[6] B Weber, T Suhina, T Junge, L Pastewka, AM Brouwer, and D Bonn. Molecular probes reveal deviations from amontons' law in multi-asperity frictional contacts. *Nature communications*, 9(1):1–7, 2018.

[7] Robert W Carpick, D Frank Ogletree, and Miquel Salmeron. A general equation for fitting contact area and friction vs load measurements. *Journal of colloid and interface science*, 211(2):395–400, 1999.

[8] Jianping Gao, WD Luedtke, D Gourdon, M Ruths, JN Israelachvili, and Uzi Landman. Frictional forces and amontons' law: from the molecular to the macroscopic scale, 2004.

[9] Xin He, Zhong Liu, Lars B Ripley, Victoria L Swensen, Isaac J Griffin-Wiesner, Beatrice R Gulner, Gabriel R McAndrews, Raymond J Wieser, Brian P Borovsky, Q Jane Wang, et al. Empirical relationship between interfacial shear stress and contact pressure in micro-and macro-scale friction. *Tribology International*, 155:106780, 2021.

[10] Alan Berman, Carlos Drummond, and Jacob Israelachvili. Amontons' law at the molecular level. *Tribology letters*, 4(2):95–101, 1998.

[11] Gang He, Martin H Müser, and Mark O Robbins. Adsorbed layers and the origin of static friction. *Science*, 284(5420):1650–1652, 1999.

[12] Frank Philip Bowden, Frank Philip Bowden, and David Tabor. *The friction and lubrication of solids*, volume 1. Oxford university press, 2001.

[13] Marius Enachescu, RJA Van den Oetelaar, RW Carpick, DF Ogletree, CFJ Flipse, and M Salmeron. Observation of proportionality between friction and contact area at the nanometer scale. *Tribology Letters*, 7(2):73–78, 1999.

[14] James A Greenwood and JB Pl Williamson. Contact of nominally flat surfaces. *Proceedings of the royal society of London. Series A. Mathematical and physical sciences*, 295(1442):300–319, 1966.

[15] Bo NJ Persson. Theory of rubber friction and contact mechanics. *The Journal of Chemical Physics*, 115(8):3840–3861, 2001.

[16] Lars Pastewka and Mark O Robbins. Contact between rough surfaces and a criterion for macroscopic adhesion. *Proceedings of the National Academy of Sciences*, 111(9):3298–3303, 2014.

[17] Bo NJ Persson. Contact mechanics for randomly rough surfaces. *Surface science reports*, 61(4):201–227, 2006.

[18] Lars Pastewka and Mark O Robbins. Contact area of rough spheres: Large scale simulations and simple scaling laws. *Applied Physics Letters*, 108(22):221601, 2016.

[19] Martin H Müser, Wolf B Dapp, Romain Bugnicourt, Philippe Sainsot, Nicolas Lesaffre, Ton A Lubrecht, Bo NJ Persson, Kathryn Harris, Alexander Bennett, Kyle Schulze, et al. Meeting the contact-mechanics challenge. *Tribology Letters*, 65(4):1–18, 2017.

[20] Binquan Luan and Mark O Robbins. The breakdown of continuum models for mechanical contacts. *Nature*, 435(7044):929–932, 2005.

[21] R Sahli, G Pallares, Christophe Ducottet, IE Ben Ali, S Al Akhrass, Matthieu Guibert, and Julien Scheibert. Evolution of real contact area under shear and the value of static friction of soft materials. *Proceedings of the National Academy of Sciences*, 115(3):471–476, 2018.

[22] Alexander J McGhee, Angela A Pitenis, Alexander I Bennett, Kathryn L Harris, Kyle D Schulze, Juan Manuel Urueña, Peter G Ifju, Thomas E Angelini, Martin H Müser, and W Gregory Sawyer. Contact and deformation of randomly rough surfaces with varying root-mean-square gradient. *Tribology Letters*, 65(4):1–7, 2017.

[23] Robert W Carpick. The contact sport of rough surfaces. *Science*, 359(6371):38–38, 2018.

[24] Dina Petrova, Bart Weber, Clémence Allain, Pierre Audebert, Daniel Bonn, and Albert M Brouwer. Fast 3d microscopy imaging of contacts between surfaces using a fluorescent liquid. *ACS applied materials & interfaces*, 10(48):40973–40977, 2018.

[25] Feng-Chun Hsia, Fiona M Elam, Daniel Bonn, Bart Weber, and Steve E Franklin. Wear particle dynamics drive the difference between repeated and non-repeated reciprocated sliding. *Tribology International*, 142:105983, 2020.

[26] Subarna R Khanal, Abhijeet Gujrati, Sai Bharadwaj Vishnubhotla, Pawel Nowakowski, Cecile S Bonifacio, Lars Pastewka, and Tevis DB Jacobs. Characterization of small-scale surface topography using transmission electron microscopy. *Surface Topography: Metrology and Properties*, 6(4):045004, 2018.

[27] Dina Petrova, Bart Weber, Cleménce Allain, Pierre Audebert, Cees H Venner, Albert M Brouwer, and Daniel Bonn. Fluorescence microscopy visualization of the roughness-induced transition between lubrication regimes. *Science advances*, 5(12):eaaw4761, 2019.

[28] Clémence Allain, Jonathan Piard, Arnaud Brosseau, Madeleine Han, Julien Paquier, Thomas Marchandier, Médéric Lequeux, Cédric Boissière, and Pierre Audebert. Fluorescent and electroactive low-viscosity tetrazine-based organic liquids. *ACS applied materials & interfaces*, 8(31):19843–19846, 2016.

[29] Maximilian Paradiz Dominguez, Begüm Demirkurt, Marion Grzelka, Daniel Bonn, Laurent Galmiche, Pierre Audebert, and Albert M Brouwer. Fluorescent liquid tetrazines. *Molecules*, 26(19):6047, 2021.

[30] H Sakuma, K Kawai, I Katayama, and S Suehara. What is the origin of macroscopic friction? *Science advances*, 4(12):eaav2268, 2018.

[31] Matthew D Butler and Dominic Vella. Liquid bridge splitting enhances normal capillary adhesion and resistance to shear on rough surfaces. *Journal of Colloid and Interface Science*, 607:514–529, 2022.

[32] PJ Van Zwol, G Palasantzas, and J Th M De Hosson. Influence of random roughness on the adhesion between metal surfaces due to capillary condensation. *Applied Physics Letters*, 91(10):101905, 2007.

[33] Emrecan Soylemez and Maarten P de Boer. Capillary-induced crack healing between surfaces of nanoscale roughness. *Langmuir*, 30(39):11625–11633, 2014.

[34] Miroslav Bartošík, Lukáš Kormoš, Lukáš Flajšman, Radek Kalousek, Jindřich Mach, Zuzana Lišková, David Nezval, Vojtěch Švarc, Tomáš Šamořil, and Tomáš Šikola. Nanometer-sized water bridge and pull-off force in afm at different relative humidities: Reproducibility measurement and model based on surface tension change. *The Journal of Physical Chemistry B*, 121(3):610–619, 2017.

[35] David B Asay and Seong H Kim. Evolution of the adsorbed water layer structure on silicon oxide at room temperature. *The Journal of Physical Chemistry B*, 109(35):16760–16763, 2005.

[36] Seongsoo Kim, Dohyun Kim, Jongwoo Kim, Sangmin An, and Wonho Jhe. Direct evidence for curvature-dependent surface tension in capillary condensation: Kelvin equation at molecular scale. *Physical Review X*, 8(4):041046, 2018.

[37] BNJ Persson. Capillary adhesion between elastic solids with randomly rough surfaces. *Journal of Physics: Condensed Matter*, 20(31):315007, 2008.

[38] M Bazrafshan, MB De Rooij, EG De Vries, and DJ Schipper. Evaluation of pre-sliding behavior at a rough interface: Modeling and experiment. *Journal of Applied Mechanics*, 87(4):041006, 2020.

[39] B Weber, T Suhina, AM Brouwer, and D Bonn. Frictional weakening of slip interfaces. *Science advances*, 5(4):eaav7603, 2019.

[40] Elsa Bayart, Ilya Svetlizky, and Jay Fineberg. Fracture mechanics determine the lengths of interface ruptures that mediate frictional motion. *Nature Physics*, 12(2):166–170, 2016.

[41] C Campana, BNJ Persson, and MH Müser. Transverse and normal interfacial stiffness of solids with randomly rough surfaces. *Journal of physics: condensed matter*, 23(8):085001, 2011.

[42] Olaf Lahayne, Bernhard Pichler, Roland Reihsner, Josef Eberhardsteiner, Jongbeom Suh, Dongsub Kim, Seungkuk Nam, Hanseung Paek, Boris Lorenz, and Bo NJ Persson. Rubber friction on ice: experiments and modeling. *Tribology Letters*, 62(2):17, 2016.

[43] Abhijeet Gujrati, Subarna R Khanal, Lars Pastewka, and Tevis DB Jacobs. Combining tem, afm, and profilometry for quantitative topography characterization across all scales. *ACS applied materials & interfaces*, 10(34):29169–29178, 2018.

[44] Luke A Thimons, Abhijeet Gujrati, Antoine Sanner, Lars Pastewka, and Tevis DB Jacobs. Hard-material adhesion: Which scales of roughness matter? *Experimental Mechanics*, 61(7):1109–1120, 2021.

[45] Michelle Ciavarella and Antonio Papangelo. Discussion of "measuring and understanding contact area at the nanoscale: A review"(jacobs, tdb, and ashlie martini, a., 2017, asme appl. mech. rev., 69 (6), p. 060802). *Applied Mechanics Reviews*, 69(6), 2017.

CHAPTER 6

Contribution of capillary adhesion to macroscopic friction

Capillary adhesion is commonly present in ambient conditions. It can be measured in single asperity contacts through atomic force microscopy using a sharp probe that is pulled off a smooth substrate. However, for macroscopic multi-asperity interfaces, the measured adhesive force is always close to zero because of the elastic energy stored into the deformation of surface roughness; this is known as the adhesion paradox. Here, we experimentally show how capillary adhesion influences friction between macroscopic Si-on-Si interfaces, covered with native oxide, in two vapor environments: humid air and isopropanol (IPA) vapor. To quantify the adhesion contribution to friction, we present a boundary element method that successfully models the interplay between capillary adhesion, surface topography and friction without adjustable parameters and show that the evolution of the surface topography during sliding dramatically increases capillary adhesion and thus friction. Replacing the water vapor with an organic (IPA) vapor, we find a lower adhesion due to the smaller surface tension.

6.1 Introduction

Approximately 71% of the surface of the Earth is covered by water. The polarity of water molecules induces strong cohesive and adhesive forces between water and hydrophilic surfaces causing water to condense at free and contacting surfaces in humid environments. The presence of water at interfaces between hydrophilic surfaces is ubiquitous and leads to capillary adhesion. This is caused by capillary bridges that typically display negative curvature in the direction normal to the interface leading to a Laplace pressure difference between the fluid inside the bridge and the surrounding gas, which in turn causes attraction of the surfaces to each other [1, 2]. This capillary attraction contributes to the ability of insects to walk vertically [2, 3, 4], dictates the mechanics of granular materials [5] and leads to failure in micro- and nano-electromechanical systems (MEMS and NEMS) [6, 7, 8, 9, 10, 11, 12]. Moreover, the car industry, 5G-networks, artificial intelligence (AI) and high-performance computing (HPC) all rely on the production of modern integrated circuits which currently are scarce. Nanoscale tribological phenomena, i.e. friction and wear, form one of the challenges in the high-precision positioning [13, 14, 15, 16] that is required for efficient chip production.

The effect of capillary adhesion on the contact mechanics and friction behavior of nanoscale single asperity interfaces is widely studied [17, 18, 19]. Many AFM experiments display a strong dependence of the capillary adhesion or friction on relative humidity (RH) [17, 19, 20]. Besides direct adhesion [19, 21], displacement of the three-phase contact line of the capillary meniscus also leads to friction [22]. Furthermore, the structure of the absorbed water layer affects the adhesion and friction at single nano-asperity contacts [19, 23, 24, 25, 26, 27]. However, the relative importance of mechanisms that control single asperity adhesion and friction is not necessarily identical to that for multi-asperity contacts. It is important to note that the typical asperity aspect ratios can vary at multi-asperity interfaces leading to changes in the relative importance of adhesion exerted across finite gaps at the interface [28]. For smooth multi-asperity contacts, the adhesion exerted within the area of real contact can become significant compared to the normal stress exerted within these contacts. In this situation, the friction will become proportional to the area of real contact with a proportionality constant that is set by the solid-on-solid adhesion [29, 30, 31, 32]. Furthermore, at multi-asperity interfaces the presence or absence of a few tall asperities can completely change the sliding behavior [33]. Surface topography can influence the uniformity of the water condensate thickness [34] and the number of capillary bridges that can form across the interface [35, 36],

thereby determining the capillary adhesion exerted at the interface.

Direct measurement of adhesion between macroscopic objects is often problematic because of the adhesion paradox [37]: despite the strong adhesive interactions that many solids undergo at the nanoscale, they rarely stick at the macroscopic scale [28]. The adhesion typically is short ranged [38] and upon unloading the interface this adhesion is cancelled by the elastic energy stored in the larger scale elastic deformation of roughness. In addition, the topography of rubbing surfaces is constantly changed by wear [33, 39]. The evolution of the surface topography and the generation of wear debris then leads to temporal variations in the capillary adhesion. The contribution of capillary adhesion to friction in macroscopic contacts therefore remains difficult to quantify, which is one of the fundamental problems for understanding the friction between macroscopic bodies. Furthermore, while there is extensive work on single asperity contacts describing capillary adhesion and friction [17, 18, 19, 21, 22, 26, 40], few studies[2, 31, 33] have aimed to bridge from nanoscale adhesion measurements to the macroscale, multi-asperity manifestation of capillary adhesion and its influence on friction.

In this work, we show how the capillary adhesion, and the contribution of capillary adhesion to friction, can be quantified through friction measurements in vapor and liquid immersed environments. Our experiments show that capillary adhesion significantly contributes to friction at multi-asperity Si-on-Si interfaces that are covered with a native oxide. The experimental results can be reproduced by a simple capillary adhesion model, without adjustable parameters, that is based on boundary element contact calculations. When compared, the experiments and model calculations demonstrate that the capillary adhesion is very sensitive to wear; removal of the highest asperities at the interface strongly reduces the average separation thereby increasing the adhesion by bringing the two surfaces closer together.

In addition to water measurements, we also perform the same experiments when the surfaces are brought in contact with an isopropanol (IPA) vapor. In agreement with our model, the adhesion is weaker due to the lower surface tension and higher volatility. For both liquids, if the contact is fully immersed, we find that the friction is significantly lower, demonstrating directly that the capillary bridges typically contribute 30% to the total friction in a partially saturated environment. We also find that the fully immersed IPA contact has a significantly lower friction than the fully immersed water contact and attribute this difference to IPA boundary lubrication. While our work focusses on Si-on-Si interfaces, the observed behavior is representative of interfaces between stiff and hydrophilic materials [31].

6.2 Experiments and calculations

6.2.1 AFM-based single asperity adhesion measurements

The single asperity pull-off experiments were performed by using atomic force microscopy (AFM) (Dimension Icon, Bruker) in four environmental conditions: isopropanol (IPA) or water vapors and IPA or water liquids. The various gas environments are established by flowing water saturated N_2 or IPA saturated N_2 into the semi-open fluid AFM cell (Bruker) at a fixed flow rate of 0.5 L/minute while the lab humidity was maintained at 50% RH. We introduced an equilibration time of 30 minutes after each change in environment to ensure a steady state gas mixture in the liquid cell. The normal displacement of the AFM probe is imposed by the piezo tube that holds at the end of the AFM cantilever adjacent to the tip. Typical force-displacement (*F-D*) curves (Figure 6.1a and b) were recorded by approaching the Si wafer with the AFM tip and subsequently retracting the tip, both at a speed of 5 nm/s, while measuring the normal force exerted at the interface. In the vapor environments we used a Si AFM tip (RTESPA-300, Bruker), and in the liquid immersed measurements–which lack capillary effects–we used a Si_3N_4 tip (SCANASYST-FLUID).

6.2.2 Macroscopic adhesion measurement

The macroscopic pull-off experiments are carried out using a universal mechanical tester (UMT Tribolab, Bruker) in an ambient air environment ($53 \pm 1.4\%$ RH). A Si ball is mounted on the force sensor (DFM-0.5G, Bruker, 1.94×10^3 N/m normal stiffness). The force sensor measures 1 mN minimum force with 0.25 mN resolution. The Si ball is pre-loaded onto a Si wafer substrate at 40 mN, and retracted from the Si wafer with 2 μm/s pull-off speed. The native oxide layer of Si is expected to form on both Si ball and Si wafer surfaces.

6.2.3 Surface characterization

The surface topography of the contacting bodies is measured by tapping mode AFM (Dimension Icon, Bruker) with Si tips (RTESPA-300, Bruker).

6.2.4 Multi-asperity capillary adhesion calculation

The calculation of capillary adhesion exerted at multi-asperity interfaces consists of two parts: contact calculations based on the boundary element method (BEM) [41] and calculations of the area wetted by the capillary liquid (A_{cap}) at the interfaces. First, the area of real contact at the Si ball-on-Si wafer interface is estimated by BEM contact calculations in which the elasto-plastic equations that describe the deformed interface are solved. We employ the contact calculations by using the Tribology Simulator that is publicly available at `www.tribology.org`. As input, the calculations make use of the measured AFM surface topography of the Si ball with about 1.7×10^3 nm^2 per pixel. The contact calculation was carried out at 40 mN elastic force (F_{elastic}) and the mechanical properties of the Si ball and the Si wafer are reported in Table C.2. The result of contact calculation is shown in Figure 6.4b and c where the solid-solid area of real contact is indicated in red. Second, we estimate the wetted area (A_{cap}) across the interface (grey area in Figure 6.4b and c) where capillary adhesion occurs as described in Results and discussion. The capillary adhesion is caused by the pressure difference between gaseous and liquid environments as quantified by the Laplace pressure (P_{Laplace}) of the capillary meniscus. The capillary meniscus at the hydrophilic interface is characterized by a positive radius of curvature (r_1) in the in-plane direction and a negative radius (r_2) of curvature in the out of plane direction as illustrated in the inset of Figure 6.1b. Because $|r_1| \gg |r_2|$ the overall radius of curvature ($\frac{1}{R_{\text{overall}}} = \frac{1}{r_1} + \frac{1}{r_2}$) of the capillary meniscus [20, 42] can be approximated as $R_{\text{overall}} \approx r_2$ such that the Laplace pressure is dominated by the negative radius of meniscus curvature. The P_{Laplace} estimated based on the Kelvin-Tolman equation is given by $P_{\text{Laplace}} = \frac{\gamma}{r_2+\delta}$ where γ the bulk liquid surface tension (see Appendix C.1), $r_2 = \frac{-d_c}{2}$ and δ the Tolman length ($\delta = 0.2$ nm at 40–50% RH) [42]. Thus, combining above calculations the capillary adhesion exerted at multi-asperity interfaces (F_{ad}) is calculated as $F_{\text{ad}} = P_{\text{Laplace}} \times A_{\text{cap}}$.

6.2.5 Macroscopic sliding experiment

Ball-on-flat friction experiments are performed using a customized rheometer setup (DSR 301, Anton Paar) in four different environmental conditions: ambient air (40% RH), IPA vapor, and liquid water and IPA immersed environments (Figure 6.2a). The 3 mm diameter Si ball ($R_q = 28.3$ nm over a 85 μm $\times$ 85 μm scan area with 430.6 nm^2 pixel size) was slid against Si flat ($R_q = 0.9$ nm over a 5 μm $\times$ 5 μm scan area [43]) at a constant angular velocity ($\omega = 8.3 \times 10^{-5}$ rad/s) that can be

converted into a constant sliding speed by multiplication with the fixed rotation radius ($r = 12.98$ mm); $V = \omega r = 1$ μm/s. The applied normal force was manually adjusted to ∼40 mN. At 40 mN normal force, the Hertzian contact pressure (P_{Hertz}) is determined to be ∼250 MPa. In order to minimize wear induced changes in friction, the measurements were performed as separate strokes–each stroke on a previously untouched piece of Si wafer to prevent the interaction between the sliding contact and wear debris [43]. The stroke length for each Si ball in the experiments is listed in Table C.3 and was minimized to avoid wear of the balls. The IPA gas flows were supplied at a constant flow rate of 5 L/minute through a plastic tube with an inner diameter of 4 mm. The tube outlet was directed at the contact and situated at a distance of up to 1 cm from the contact. Dry N_2 saturated with IPA vapor was generated by passing dry N_2 through a liquid IPA bubbler. In all experiments the flow was turned on before creating contacts. Each set of sliding experiments was repeated at least three times under the same environmental condition.

6.3 Results and discussion

6.3.1 Adhesion at single asperity contacts

To relate adhesion at single asperity interfaces to adhesion at multi-asperity interfaces, we perform pull-off experiments at single and multi-asperity Si-on-Si hydrophilic interfaces. The single asperity AFM-based experiments (see Experiments 6.2.1) were performed both in water rich and in IPA rich vapor environments. Control over the environment was obtained by introducing a 0.5 L/minute air flow into a semi-open fluid AFM cell (Bruker). The air flow consisted of dry nitrogen that was passed through a gas wash bottle filled with either water or IPA. This resulted in a relative humidity of 58 ± 0.7% RH inside the AFM cell when the air flow was bubbled through water. The partial pressure of IPA in the AFM cell resulting from bubbling the dry nitrogen through IPA could not be measured directly and is treated as unknown.

In both environments water and IPA, a Si AFM tip was moved towards the surface of a Si wafer and retracted afterwards at a speed of 5 nm/s, sufficiently slow to warrant (near) equilibrium conditions [27, 44, 45]. The externally applied normal force (F) on the tip was measured through the deflection of the AFM cantilever as a function of the normal displacement (D) resulting in a typical F-D curve (Figure 6.1a and b). Such F-D curves clearly indicate that the tip snaps into contact roughly 4 nm

(W_{tip} in Figure 6.1a) before a repulsive force is detected on the AFM cantilever [27]. In the repulsive part of the *F-D* curve, the measured normal force increases linearly with displacement at a rate that is set by the stiffness of the AFM cantilever, 42 N/m in our experiments. Upon retraction of the probe we measured an *F-D* curve that approximately follows the approach curve, except for the important distinction that the probe can be retracted by up to 10 nm beyond the snap-in point before the probe is completely pulled off the surface and no normal force is measured. This rather long pull-off distance is often interpreted [27] in the context of capillary adhesion; the reduced pressure inside a negatively curved capillary bridge between tip and substrate causes an attractive force (inset of Figure 6.1b) and the attractive force is gradually reduced as the tip is separated from the substrate and the capillary bridge is stretched [36].

To test this interpretation, we also performed *F-D* measurements with the tip-substrate interface fully immersed in liquid water or IPA (inset of Figure 6.1a and b). Indeed, the adhesive strength and range are strongly reduced in liquid immersed experiments; since there is no gas phase available, capillary bridges cannot form. We define the adhesive force as the difference between the minimum force and the force measured when there is no interaction between the tip and the substrate (Figure 6.1a). To further understand the nature of the adhesion, we calculate the adhesive force using the model from Ref. [20] that incorporates three contributions: (i) the capillary force caused by the Laplace pressure acting over the area on the tip that is wetted by the capillary bridge ($F_c = \gamma(\frac{1}{r_1} + \frac{1}{r_2})\pi R'^2$). (ii) The tension force ($F_t = 2\pi R'\gamma\cos\alpha\sin\beta$) caused by the surface tension acting on the three phase contact line of the capillary bridge. (iii) The van der Waals force ($F_v = (H_{air}(1 - A_{Rel}) + H_{water}A_{Rel})\frac{R_{tip}}{6d_a^2}$) that causes attraction of the solids across an air or liquid medium (see Appendix C.1 for details). The adhesion model approximates the tip-sample interface as a sphere-on-flat interface and can be evaluated if the tip radius and the amount of water present at the interface are known. The former we obtain through tip deconvolution ($R_{tip} = 28 \pm 2$ nm, see Appendix C.2) and the latter we infer from the literature [42, 46]; both the critical distance for capillary condensation ($d_c = 3$ nm, see Figure 6.1b inset) and the thickness of condensed water on a free Si substrate ($h = 1.2$ nm, see Figure 6.1b inset) were measured at the relative humidity corresponding to our experiment ($58 \pm 0.7\%$).

We find good agreement between the adhesion model prediction (54 ± 4 nN)–without adjustable parameters–and the adhesion experiment conducted in the 58% RH environment (52 ± 15 nN). The capillary force (F_c) is responsible for ~80% of the total adhesive force according to the model: indeed capillary adhesion is the

dominant adhesion mechanism. Furthermore, the observed snap-in distance (W_{tip}) in the experiments (see Figure 6.1a) was 3.9 ± 0.2 nm, close to that observed in tuning fork based experiments: $W_{tip} = h + d_c = 4.2 \pm 0.3$ nm at 58% RH (Table C.1) [42, 46]. The error quantifies the standard deviation of the distribution of pull-off forces that were observed (Figure C.2). This variation in pull-off forces is thought to result from a thermally activated pull-off process [47]. In the measurements conducted with the same AFM tip in an IPA rich environment, we observe a snap in distance of $W_{tip} = 7 \pm 0.7$ nm and an adhesive force of 34 ± 14 nN. Interestingly, in comparison to the humid measurements, the adhesive force is smaller while the area of the tip that is wetted by the capillary bridge must be larger, due to the increased snap-in distance [48, 49]. The capillary force (F_c), the tension force (F_t) and the van der Waals force (F_v) are likely all reduced when IPA is introduced into the environment while water is removed. Capillary force and tension force are proportional to the liquid surface tension, which is lower for IPA than for water. The van der Waals force scales with the difference in refractive index between silicon and the medium in between the tip and the substrate. Since IPA has a higher refractive index than water, this force should also decrease upon the introduction of IPA [50]. However, since the capillary force is dominant, we focus our discussion on this force.

The capillary force is the product of the tip area that is wetted by a capillary bridge and the Laplace pressure difference: $P_{Laplace} = \frac{\gamma}{R_{overall}}$, with γ the liquid surface tension and $R_{overall}$ the radius of curvature of the capillary bridge. As water at the interface is replaced with IPA, the wetted area of the tip and the curvature of the capillary bridge change slightly [42, 49], while the surface tension drops by a factor 3 ($\gamma_{IPA} = 23.8$ mN/m [51] and $\gamma_{water} = 72.8$ mN/m [52]). We argue that this strong reduction in surface tension thus drives the drop in adhesive force observed when the humid environment is dried and IPA is introduced at the interface. The AFM experiments show that capillary adhesion is the dominant adhesion mechanism at single asperity Si-on-Si interfaces. Reduction of the humidity and introduction of IPA into the environment of the contact strongly reduces the capillary adhesion while increasing its range.

6.3.2 Adhesion at multi-asperity contacts

Virtually all frictional interfaces are multi-asperity; the key question is how the capillary adhesion that dominates single asperity Si-on-Si interfaces manifests itself at larger multi-asperity Si-on-Si interfaces. To answer this question, we performed ball-on-flat pull-off experiments. In the pull-off experiments a 3 mm diameter Si

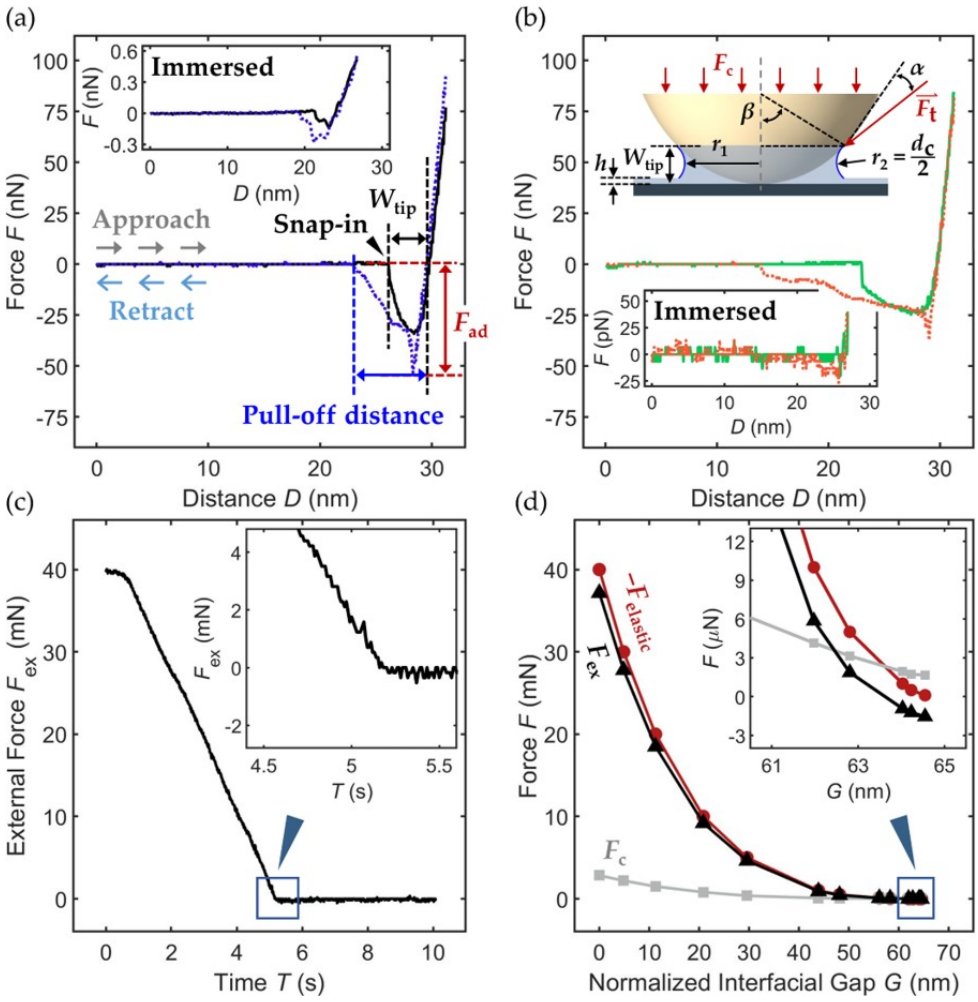

Figure 6.1: Single nano-asperity and macroscopic multi-asperity pull-off force measurements and calculations. (a) A typical force-displacement (*F*-*D*) curve measured at a relative humidity (RH) of 58%, showing the tip-sample normal force measured by AFM as the tip approaches the sample and as the tip is retracted. (b) An *F*-*D* curve measured by AFM in an isoproponal (IPA) rich vapor environment. The inset (a) and lower inset (b) display an *F*-*D* curve measured while the tip-sample interface is immersed in liquid water and IPA, respectively. The upper inset (b) illustrates a capillary bridge and the capillary and tension forces exerted at such a bridge. (c) External force (F_{ex}) as a function of time (T) measured in the UMT during the retraction of a Si ball from a Si wafer surface, the inset shows a close up. (d) The BEM calculation of capillary adhesion (F_c) exerted at the Si ball-on-Si wafer interface as a function of the average interfacial gap relative to the average interfacial gap corresponding to an elastic force of 40 mN. The inset shows that as the elastic force ($F_{elastic}$) decreases to zero the capillary adhesive and external force, both on the order of μN, cancel each other. The experiments and calculations in (c) and (d) were conducted at a relative humidity of $53 \pm 1.4\%$ and 50%, respectively.

ball was brought into contact with a Si wafer in a 53% RH air environment, after which a load of 40 mN was applied and the ball was pulled ball back up (see Figure 6.1c and Experiments 6.2.2). Perhaps surprisingly, within the mN accuracy of the experiment, no pull-off force was detected (inset of Figure 6.1c). It should be noted that the high stiffness of the force sensor, combined with the pull-off speed, limits the sensitivity to adhesion of the macroscale adhesion experiment (see Experiments 6.2.2 for details). The force balance at the interface requires that the capillary adhesion (F_c) and the externally applied load (F_{ex}) cancel the elastic force ($F_{elastic}$) generated by the compressed asperities at the interface: $-\overrightarrow{F_{elastic}} = \overrightarrow{F_{ex}} + \overrightarrow{F_c}$. During pull-off, the external load vanishes. The capillary bridges pull the two surfaces together, but in doing so elastically deform the asperities thereby generating an elastic counter force. Due to the high stiffness of the Si asperities, the elastic energy dominates over the adhesion energy. This is the reason why no pull-off force is measured, and the origin of the adhesion paradox.

To understand what happens quantitatively, we carried out boundary element method (BEM) contact calculations (see Experiments 6.2.4) to estimate the elastic and capillary force at multi-asperity interfaces as a function of interfacial gap (Figure 6.1d). The BEM contact calculation takes the surface topography of the pristine Si ball, measured by AFM (Figure 6.3a), as input together with the mechanical properties of Si as listed in Table C.2 (see Experiments 6.2.3). The BEM solver subsequently calculates how the topography is elastically deformed by a given load ($F_{elastic}$) in the absence of adhesion. The resulting interface gap profile can be used to estimate the capillary force associated with that interface geometry. To roughly estimate the capillary force, we assume that–like in the single asperity AFM experiments–water can condense at regions of the interface within which the interfacial gap is finite but smaller than $W = 2h + d_c$ (see Figure 6.1b inset; we assume a water layer of equilibrium thickness on both surfaces). Across this area within which capillary condensation can take place, a Laplace pressure difference caused by the negative curvature of the water-air interface in the direction normal to the contact, leads to capillary attraction. To estimate the capillary force (F_c), we multiply the Laplace pressure difference with the area of the interface at which the gap is larger than zero and smaller than W. The equilibrium values for both W and the Laplace pressure difference can be obtained from the literature [42, 49] as a function of relative humidity. Furthermore, our single asperity experiments (Figure 6.1) with the same materials confirm the range and strength of the capillary adhesion found in the literature. Subsequently the external force at which the calculated interface is balanced is given by $-\overrightarrow{F_{ex}} = \overrightarrow{F_{elastic}} + \overrightarrow{F_c}$.

The result of the calculations, conducted for various elastic forces (F_{elastic}) is summarized in Figure 6.1d. The calculations show that the pull-off force (F_{ex}) is negligible (μN) compared to the mN accuracy of the experiment; multi-asperity adhesion may be significant at a loaded interface but disappears due to the elasticity of the asperities when the external load is removed. Rough estimates of the elastic and adhesion energy can be obtained by integrating the calculated force distance curve upon loading (assuming 10^5 N/m contact stiffness [31]): 20 mN $\times$ 400 nm = 8×10^{-9} J, and by multiplying the water surface tension with the area of apparent contact (Figure 6.4c): $72.8 \times 10^{-3} \times (\pi(10 \times 10^{-6})^2) = 2.3 \times 10^{-11}$ J. Indeed, this estimate confirms that for this stiff system elastic energy dominates over surface energy. This destructive interplay between adhesion and elasticity is known as the adhesion paradox; despite strong adhesive interactions at the molecular scale larger interfaces usually do not display stickiness because the elasticity of compressed asperities cancels out the adhesion when the external load is removed [43].

6.3.3 Capillary adhesion and friction

The adhesion paradox thus prevents direct measurement of Si ball-on-Si wafer multi-asperity adhesion through pull-off experiments. This makes it challenging to understand how the adhesion contributes to the friction at such interfaces. To elucidate the contribution to friction of capillary adhesion, we perform Si ball-on-Si wafer sliding experiments (Figure 6.2a) in ambient ($41 \pm 1\%$ RH) and IPA vapor as well as liquid environments (see Experiments 6.2.5). The frictional force (F_{f}) was measured during sliding and converted into a coefficient of friction (CoF), which is the ratio of frictional force to normal force (F_{n}): $\text{CoF} = \frac{F_{\text{f}}}{F_{\text{n}}}$. We confirmed that the CoF was well-defined and independent of the normal force (Figure C.3).

The friction experiments show that the CoF measured in ambient and IPA vapor environments is significantly higher than the CoF measured in water and IPA immersed environments (Figure 6.2b). At low sliding speeds ($V = 1$ μm/s) the high Si ball-on-Si wafer contact pressure ($P_{\text{Hertz}} = \sim$250 MPa) in combination with the low viscosity of the fluids ($\eta_{\text{water}} = 1.0 \times 10^{-3}$ Pa s and $\eta_{\text{IPA}} = 2.4 \times 10^{-3}$ Pa s at 20 °C) clearly excludes hydrodynamic lubrication, and places the sliding system in the boundary lubrication regime (Hersey number 10^{-13}). We therefore argue that since both water and IPA form thick boundary layers on Si when presented in the gas phase [42, 49], the boundary lubrication of the system should not be affected by the change from water vapor to liquid water [19] or from IPA vapor to liquid IPA. However, there is an important difference between the vapor experiments and the

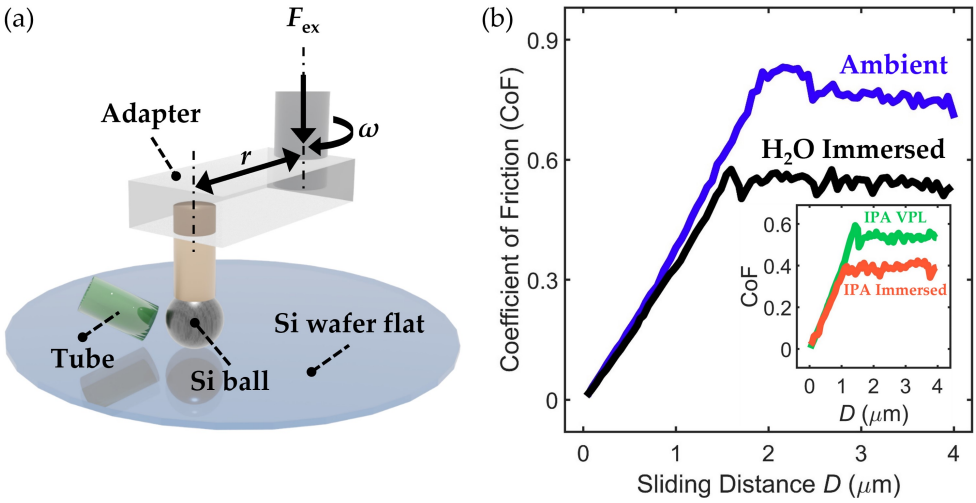

Figure 6.2: Macroscopic siding experiment. (a) The Si ball-on-Si wafer friction measurements are performed using a customized rheometer that measures the normal force and torque exerted on a geometry to which the Si ball is clamped while it is slid at a constant externally applied normal force (F_{ex}) and angular velocity (ω). A plastic tube is mounted right next to the 3 mm ball to perform IPA VPL friction experiments. The tube directs a gas flow of dry N_2 that is passed through a gas wash bottle filled with IPA towards the interface at a rate of 5 L/minute (see Experiments 6.2.5 for more details). (b) The static and dynamic coefficient of friction (CoF) are measured in ambient ($41 \pm 1\%$ RH) and water immersed environments. The inset of (b) shows the COF measured in IPA vapor as described above and immersed in IPA. All measurements are performed at a normal force of 40 mN and a sliding velocity of 1 μm/s.

liquid immersed experiments: when the Si-on-Si interface is fully immersed in water or IPA, capillary adhesion is absent since capillary menisci can only form when a gas phase is present. The reduction in friction upon immersion can therefore be translated into a capillary adhesive force: $F_c = (\frac{\text{CoF}_{\text{vapor}}}{\text{CoF}_{\text{immersed}}} - 1) \times F_{ex}$, where ($\text{CoF}_{\text{vapor}}$ and $\text{CoF}_{\text{immersed}}$ are the CoF measured in vapor and liquid immersed environments, respectively. Implicit in this calculation is the assumption that the frictional force is proportional to the normal force (Figure C.3) experienced by the asperities [30], an assumption that was recently confirmed in a similar system [31]. The capillary adhesion thus calculated at an external force of $F_{ex} = 40$ mN for both water (41% RH) and IPA rich vapor environments is 23 ± 5 mN and 8 ± 5 mN, respectively. We observe stronger capillary adhesion in the ambient environment than in the IPA environment, like in the AFM measurements. However, the capillary adhesion

estimated from the sliding experiments (23 ± 5 mN) is significantly larger than that calculated for the interface under 40 mN externally applied load (2.8 mN, Figure 6.1d). Furthermore, we find that in the absence of capillary adhesion (immersed conditions), the CoF for the IPA experiment is about 30% lower than that measured in water (Figure 6.2b). This reduction in CoF may be attributed to the difference in boundary lubrication between water and IPA [40].

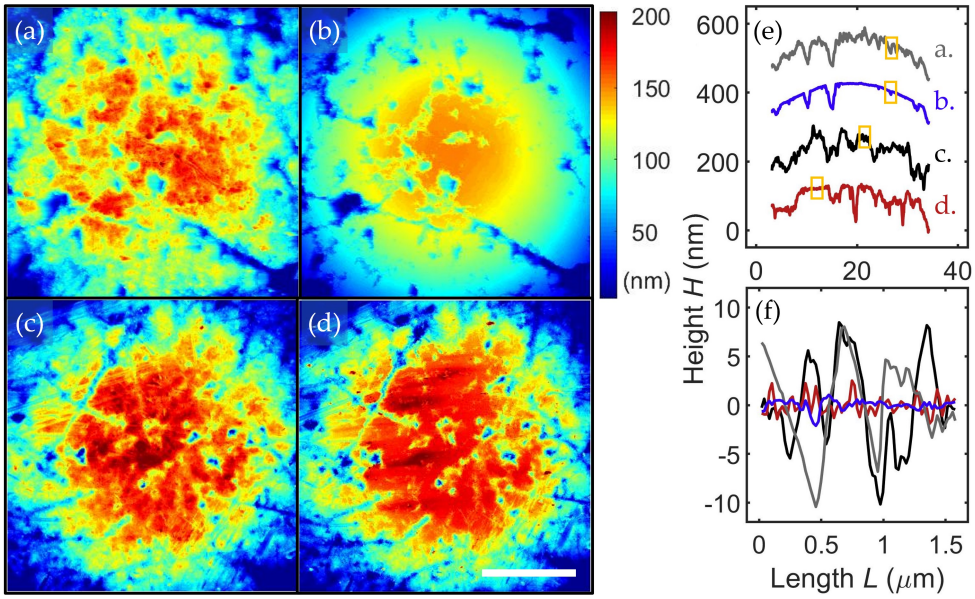

Figure 6.3: Atomic force microscopy (AFM) surface topography of Si balls. The AFM topography of a pristine Si ball (a) and (b) an artificially worn Si ball. The AFM topography of a pristine Si ball before sliding (c) and (d) after 190 μm sliding at a velocity of 1 μm/s and a normal force of 40 mN. The AFM topographies are measured over a 31 μm $\times$ 31 μm scan area with 430.6 nm^2 pixel size. (e) The cross-section height profile (H) of the topographies shown in (a–d). (f) Zoom in height profile corresponding to the orange boxes in (e). Scale bar, 10 μm.

6.3.4 Capillary adhesion and wear

To understand the discrepancy between the calculated (2.8 mN) and experimentally estimated (23 ± 5 mN) water capillary adhesive force in more detail, we return to the contact calculations. Since the contact calculations are based on the topography of the Si ball measured by AFM before performing sliding experiments, the calculations

may not represent the experimental interface accurately. AFM topography measurements performed on the Si ball after the sliding experiment reveal a circular wear scar. To estimate how much material was removed from the sphere, we calculated the volume of the spherical cap (Figure C.4) corresponding to the wear scar and found an average wear volume $V_{\mathrm{avg}} = 4.3 \pm 1.3 \times 10^9$ nm^3 based on four independent sliding experiments. The average total sliding distance for the four experiments was 205 μm (D_{Tot}, Table C.3) and the normal force (F_{ex}) was 40 mN leading to a specific wear rate (K) of the Si ball that is $K = \frac{V_{\mathrm{avg}}}{F_{\mathrm{ex}} D_{\mathrm{Tot}}} = 5.2 \times 10^5$ μm^3/Nm, which can be interpreted as mild wear.

We emphasize that most wear is expected to take place when sharp and high asperities on the Si ball are removed during the very first stroke, as demonstrated previously [33]. The cross-section height profiles of the Si ball surface taken after sliding indeed show that high asperities are removed from the Si ball (the red curve in Figure 6.3e) resulting in a reduced root mean square (RMS) roughness (R_{q}, calculated along the 1.5 μm profile in Figure 6.3f) as low as 0.9 nm in the contacting regions–comparable to the roughness of the Si wafer counter surface. To mimic this dynamic material removal process, we analyze the AFM topography recorded before the sliding experiments as follows. First, we remove the sphere curvature from the data. Next, we cut the highest asperities off the topography (Figure 6.3a) by setting all heights above a (variable) threshold value equal to that threshold value. Subsequently, we impose the Si wafer roughness on top of the cut (flattened) areas of the topography (Figure 6.3b). This last step is motivated by the observation (Figure 6.3d–f) that worn areas on the Si ball display a roughness akin to that of the counter surface; the Si wafer. Once the topography has thus been artificially worn, we impose the sphere curvature again and run BEM calculations in which the artificially worn sphere is pressed onto a Si wafer. To calculate the artificial wear volume, we subtract the original topography from the worn topography (Figure 6.3a and b).

We calculated the capillary adhesive force at the Si ball-on-Si wafer interface that is externally loaded with a force of 40 mN as a function of wear volume (Figure 6.4a). As the roughness of the sphere decreases due to increasing wear an increase in capillary adhesion results (Figure 6.4a inset); worn topographies experience stronger adhesion. The reason for this is that high asperities on the ball surface initially prevent intimate contact between the two surfaces. As such asperities are removed, water bridges can form across more regions of the interface and therefore generate more capillary adhesion [37]. The model predicts that the adhesive force increases from 2.8 mN for the pristine surface to 28 mN for the Si ball surface from which

$V_{avg} = 4.3 \times 10^9$ nm^3 of material was worn, in agreement with the experiments based on which an adhesive force of 23 ± 5 mN was found. This result is also in line with the analytical capillary adhesion model proposed by Persson [53] in which the capillary adhesion increases strongly when the root mean square roughness of the interface approaches the range of the adhesion.

In addition to the water adhesion calculations, we performed contact calculations relating to the IPA vapor environment. However, because the precise composition of the gas surrounding the interface is unknown, we used literature values for W and $P_{Laplace}$ that correspond to an IPA partial pressure (P/P_{sat}) range of 10–70%. According to our model the capillary adhesion increases with decreasing IPA partial pressure; the effect of increasing Laplace pressure with decreasing IPA partial pressure outweighs the decrease in the wetted area with decreasing partial pressure (decreasing W). The IPA capillary adhesion calculations as a function of wear show good agreement with the experimental estimates of the adhesive force and support the interpretation of our experiments and our model. The relative impact of capillary adhesion is greatly enhanced by wear, but can be minimized by replacing water in the environment with IPA. Furthermore, in the absence of capillary adhesion, Si-on-Si friction is lower in an IPA immersed environment than in a water immersed environment suggesting that IPA is more effective as a boundary lubricant. The mechanism behind this boundary lubrication provided by IPA may lie in its ability to passivate bond-forming species such as hydroxyl groups, thereby lowering the surface energy and friction [54, 55]. Furthermore, IPA may suppress wear and slow down the wear induced changes in adhesion [54].

6.4 Conclusion

We demonstrated that capillary adhesion dominates single nano-asperity Si-on-Si pull-off force measurements. While strong capillary adhesion is present at loaded multi-asperity interfaces, the adhesion disappears when the load is removed. Nonetheless, the capillary adhesive force at a loaded multi-asperity interface significantly increases friction. Wear of the highest roughness peaks drastically reduces the average interfacial gap thereby further increasing adhesion and friction. This interplay between capillary adhesion, wear induced topography changes and friction was successfully captured by a boundary element model without adjustable parameters. One assumption in the model is that the capillary bridges are in equilibrium with the surrounding vapor. This assumption is known to break down at velocities above 100

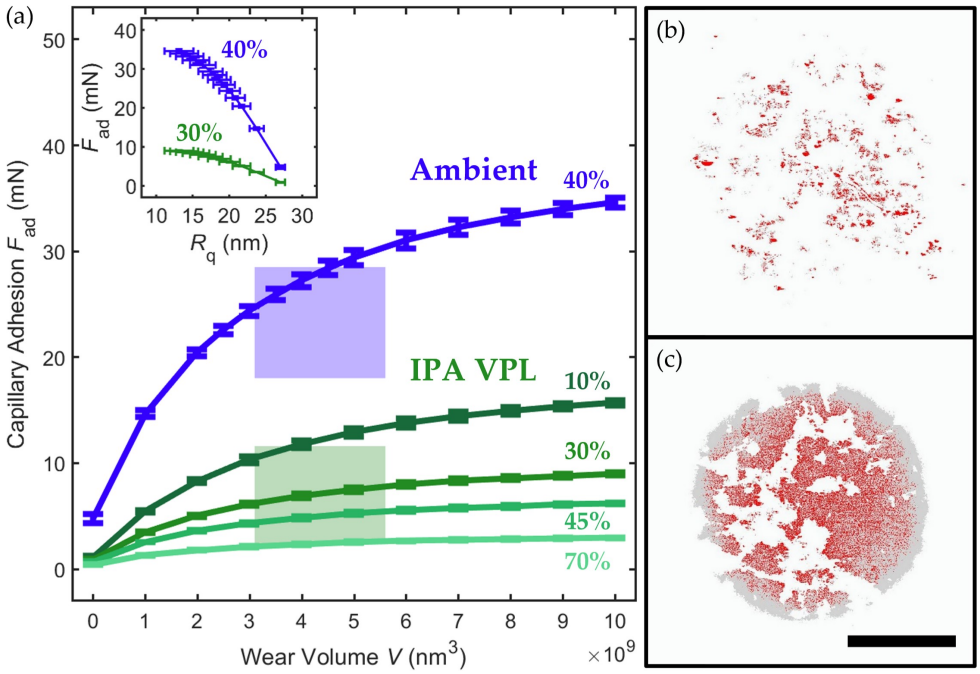

Figure 6.4: Si ball-on-Si wafer capillary adhesion calculations and experiments. (a) Calculated capillary adhesion (F_{ad}) at 40 mN external load in ambient (40% relative humidity, blue line) and 10–70% partial pressure of IPA vapor (green lines) environments as a function of wear volume (V). The adhesive forces in (a) were calculated based on the topographies of 4 independent Si balls, we report the average and the standard deviation of the results. The experimental estimates of the capillary adhesion and wear volume are reflected by the blue (ambient) and green (IPA) shaded squares. The capillary adhesion is plotted against the root mean square (RMS) roughness (R_q) of the artificially worn Si ball in the inset of (a). The BEM contact calculations of solid-solid contacts (red) and capillary-wetted areas (grey, $W = 4$ nm) are shown for the pristine ($V = 0$ nm^3) Si ball (b) and the artificially worn ($V = 4 \times 10^9$ nm^3) Si ball (c). Scale bar, 10 μm.

μm/s [56], well above the sliding speeds (and pull-off speeds) investigated in this work. Capillary adhesion and wear can easily lead to failure of devices that involve silicon based interfaces with nanoscale surface roughness such as MEMS and NEMS. The latter is known to occur through nanoscale wear processes [43]. Our model can be used to predict the friction behavior and failure of stiff hydrophilic interfaces in general [31]. Furthermore, we showed that replacement of water with IPA strongly reduces capillary adhesion and improves boundary lubrication. These insights pave

the way for better control over friction and wear in demanding high-tech applications such as the positioning systems used in the semiconductor manufacturing industry.

Bibliography

[1] Emrecan Soylemez and Maarten P de Boer. Capillary-induced crack healing between surfaces of nanoscale roughness. *Langmuir*, 30(39):11625–11633, 2014.

[2] Matthew D Butler and Dominic Vella. Liquid bridge splitting enhances normal capillary adhesion and resistance to shear on rough surfaces. *Journal of Colloid and Interface Science*, 607:514–529, 2022.

[3] Longjian Xue, Alexander Kovalev, Anna Eichler-Volf, Martin Steinhart, and Stanislav N Gorb. Humidity-enhanced wet adhesion on insect-inspired fibrillar adhesive pads. *Nature communications*, 6(1):1–9, 2015.

[4] Sophie Gernay, Walter Federle, Pierre Lambert, and Tristan Gilet. Elasto-capillarity in insect fibrillar adhesion. *Journal of The Royal Society Interface*, 13(121):20160371, 2016.

[5] Maryam Pakpour, Mehdi Habibi, Peder Møller, and Daniel Bonn. How to construct the perfect sandcastle. *Scientific reports*, 2(1):1–3, 2012.

[6] JA Williams and HR Le. Tribology and mems. *Journal of Physics D: Applied Physics*, 39(12):R201, 2006.

[7] Seong H Kim, David B Asay, and Michael T Dugger. Nanotribology and mems. *Nano today*, 2(5):22–29, 2007.

[8] Antonis I Vakis, Vladislav A Yastrebov, Julien Scheibert, Lucia Nicola, Daniele Dini, Clotilde Minfray, Andreas Almqvist, Marco Paggi, Seunghwan Lee, Georges Limbert, et al. Modeling and simulation in tribology across scales: An overview. *Tribology International*, 125:169–199, 2018.

[9] Oded Hod, Ernst Meyer, Quanshui Zheng, and Michael Urbakh. Structural superlubricity and ultralow friction across the length scales. *Nature*, 563(7732):485–492, 2018.

[10] Owen Y Loh and Horacio D Espinosa. Nanoelectromechanical contact switches. *Nature nanotechnology*, 7(5):283–295, 2012.

[11] Paolo F Ferrari, SunPhil Kim, and Arend M Van Der Zande. Dissipation from interlayer friction in graphene nanoelectromechanical resonators. *Nano letters*, 21(19):8058–8065, 2021.

[12] Ashkan Ghanbarzadeh-Dagheyan, Nader Jalili, and Mohammad Taghi Ahmadian. A holistic survey on mechatronic systems in micro/nano scale with challenges and applications. *Journal of Micro-Bio Robotics*, pages 1–22, 2021.

[13] Yanling Tian, Zhichen Huo, Fujun Wang, Cunman Liang, Beichao Shi, and Dawei Zhang. A novel friction-actuated 2-dof high precision positioning stage with hybrid decoupling structure. *Mechanism and Machine Theory*, 167:104511, 2022.

[14] Dongwoo Kang, Xin Dong, Hyunchang Kim, Pyungwon Park, and Chinedum E Okwudire. Friction isolated rotary system for high-precision roll-to-roll manufacturing. *Precision Engineering*, 68:358–364, 2021.

[15] Yun-Hsiang Sun, Tao Chen, Christine Qiong Wu, and Cyrus Shafai. Comparison of four friction models: feature prediction. *Journal of Computational and Nonlinear Dynamics*, 11(3), 2016.

[16] Sébastien Thiery, Marc Kunze, Alireza Karimi, Alain Curnier, and Roland Longchamp. Friction modeling of a high-precision positioning system. In *2006 American Control Conference*, pages 5–pp. IEEE, 2006.

[17] Kathryn Hasz, Zhijiang Ye, Ashlie Martini, and Robert W Carpick. Experiments and simulations of the humidity dependence of friction between nanoasperities and graphite: The role of interfacial contact quality. *Physical Review Materials*, 2(12):126001, 2018.

[18] Christian Greiner, Jonathan R Felts, Zhenting Dai, William P King, and Robert W Carpick. Controlling nanoscale friction through the competition between capillary adsorption and thermally activated sliding. *ACS nano*, 6(5):4305–4313, 2012.

[19] Lei Chen, Chen Xiao, Bingjun Yu, Seong H Kim, and Linmao Qian. What governs friction of silicon oxide in humid environment: contact area between solids, water meniscus around the contact, or water layer structure? *Langmuir*, 33(38):9673–9679, 2017.

[20] Miroslav Bartošík, Lukáš Kormoš, Lukáš Flajšman, Radek Kalousek, Jindřich Mach, Zuzana Lišková, David Nezval, Vojtěch Švarc, Tomáš Šamořil, and Tomáš Šikola. Nanometer-sized water bridge and pull-off force in afm at different relative humidities: Reproducibility measurement and model based on surface tension change. *The Journal of Physical Chemistry B*, 121(3):610–619, 2017.

[21] Elisa Riedo, Francis Lévy, and Harald Brune. Kinetics of capillary condensation in nanoscopic sliding friction. *Physical review letters*, 88(18):185505, 2002.

[22] Manhee Lee, Bongsu Kim, Jongwoo Kim, and Wonho Jhe. Noncontact friction via capillary shear interaction at nanoscale. *Nature communications*, 6(1):1–6, 2015.

[23] Tai-De Li, Hsiang-Chih Chiu, Deborah Ortiz-Young, and Elisa Riedo. Nanorheology by atomic force microscopy. *Review of Scientific Instruments*, 85(12):123707, 2014.

[24] Deborah Ortiz-Young, Hsiang-Chih Chiu, Suenne Kim, Kislon Voïtchovsky, and Elisa Riedo. The interplay between apparent viscosity and wettability in nanoconfined water. *Nature communications*, 4(1):1–6, 2013.

[25] Chen Xiao, Pengfei Shi, Wenmeng Yan, Lei Chen, Linmao Qian, and Seong H Kim. Thickness and structure of adsorbed water layer and effects on adhesion and friction at nanoasperity contact. *Colloids and Interfaces*, 3(3):55, 2019.

[26] KB Jinesh and JWM Frenken. Capillary condensation in atomic scale friction: how water acts like a glue. *Physical review letters*, 96(16):166103, 2006.

[27] Manuel R Uhlig and Ricardo Garcia. In situ atomic-scale imaging of interfacial water under 3d nanoscale confinement. *Nano Letters*, 2021.

[28] Lars Pastewka and Mark O Robbins. Contact between rough surfaces and a criterion for macroscopic adhesion. *Proceedings of the National Academy of Sciences*, 111(9):3298–3303, 2014.

[29] Xin He, Zhong Liu, Lars B Ripley, Victoria L Swensen, Isaac J Griffin-Wiesner, Beatrice R Gulner, Gabriel R McAndrews, Raymond J Wieser, Brian P Borovsky, Q Jane Wang, et al. Empirical relationship between interfacial shear stress and contact pressure in micro-and macro-scale friction. *Tribology International*, 155:106780, 2021.

[30] Alan Berman, Carlos Drummond, and Jacob Israelachvili. Amontons' law at the molecular level. *Tribology letters*, 4(2):95–101, 1998.

[31] Feng-Chun Hsia, Steve Franklin, Pierre Audebert, Albert M Brouwer, Daniel Bonn, and Bart Weber. Rougher is more slippery: How adhesive friction decreases with increasing surface roughness due to the suppression of capillary adhesion. *Physical Review Research*, 3(4):043204, 2021.

[32] H Sakuma, K Kawai, I Katayama, and S Suehara. What is the origin of macroscopic friction? *Science advances*, 4(12):eaav2268, 2018.

[33] Feng-Chun Hsia, Fiona M Elam, Daniel Bonn, Bart Weber, and Steve E Franklin. Tracing single asperity wear in relation to macroscale friction during running-in. *Tribology International*, page 107108, 2021.

[34] M Bazrafshan, MB de Rooij, and DJ Schipper. Adhesive force model at a rough interface in the presence of thin water films: The role of relative humidity. *International journal of mechanical sciences*, 140:471–485, 2018.

[35] Jizeng Wang, Jin Qian, and Huajian Gao. Effects of capillary condensation in adhesion between rough surfaces. *Langmuir*, 25(19):11727–11731, 2009.

[36] M Sedighi, VB Svetovoy, and G Palasantzas. Capillary-force measurement on sic surfaces. *Physical Review E*, 93(6):062803, 2016.

[37] A Tiwari, J Wang, and BNJ Persson. Adhesion paradox: Why adhesion is usually not observed for macroscopic solids. *Physical Review E*, 102(4):042803, 2020.

[38] Luke A Thimons, A Gujrati, A Sanner, L Pastewka, and TDB Jacobs. Data associated with publication:" hard-material adhesion: Which scales of roughness matter?" by la thimons, a. gujrati, a. sanner, l. pastewka, tdb jacobs, published in experimental mechanics, 2021. 2021.

[39] Son Pham-Ba and Jean-François Molinari. Creation and evolution of roughness on silica under unlubricated wear. *Wear*, 472:203648, 2021.

[40] David B Asay, Erik Hsiao, and Seong H Kim. Effects of adsorbate coverage and capillary on nano-asperity friction in atmosphere containing organic vapor. *Journal of Applied Physics*, 110(6):064326, 2011.

[41] Martin H Müser, Wolf B Dapp, Romain Bugnicourt, Philippe Sainsot, Nicolas Lesaffre, Ton A Lubrecht, Bo NJ Persson, Kathryn Harris, Alexander Bennett, Kyle Schulze, et al. Meeting the contact-mechanics challenge. *Tribology Letters*, 65(4):1–18, 2017.

[42] Seongsoo Kim, Dohyun Kim, Jongwoo Kim, Sangmin An, and Wonho Jhe. Direct evidence for curvature-dependent surface tension in capillary condensation: Kelvin equation at molecular scale. *Physical Review X*, 8(4):041046, 2018.

[43] Feng-Chun Hsia, Fiona M Elam, Daniel Bonn, Bart Weber, and Steve E Franklin. Wear particle dynamics drive the difference between repeated and non-repeated reciprocated sliding. *Tribology International*, 142:105983, 2020.

[44] Tobias Cramer, Francesco Zerbetto, and Ricardo García. Molecular mechanism of water bridge buildup: Field-induced formation of nanoscale menisci. *Langmuir*, 24(12):6116–6120, 2008.

[45] Shengfeng Cheng and Mark O Robbins. Nanocapillary adhesion between parallel plates. *Langmuir*, 32(31):7788–7795, 2016.

[46] David B Asay and Seong H Kim. Evolution of the adsorbed water layer structure on silicon oxide at room temperature. *The Journal of Physical Chemistry B*, 109(35):16760–16763, 2005.

[47] AV Pinon, M Wierez-Kien, AD Craciun, N Beyer, JL Gallani, and MV Rastei. Thermal effects on van der waals adhesive forces. *Physical Review B*, 93(3):035424, 2016.

[48] Emrecan Soylemez and Maarten P de Boer. Crack healing between rough polycrystalline silicon hydrophilic surfaces in n-pentanol and water vapors. *Tribology Letters*, 59(1):1–12, 2015.

[49] Dohyun Kim, Jongwoo Kim, Jonggeun Hwang, Dongha Shin, Sangmin An, and Wonho Jhe. Direct measurement of curvature-dependent surface tension of an alcohol nanomeniscus. *Nanoscale*, 13(14):6991–6996, 2021.

[50] C Mathew Mate and Robert W Carpick. *Tribology on the small scale: a modern textbook on friction, lubrication, and wear*. Oxford University Press, USA, 2019.

[51] Shaina Kelly, Carlos Torres-Verdín, and Matthew T Balhoff. Anomalous liquid imbibition at the nanoscale: the critical role of interfacial deformations. *Nanoscale*, 8(5):2751–2767, 2016.

[52] David B Asay and Seong H Kim. Effects of adsorbed water layer structure on adhesion force of silicon oxide nanoasperity contact in humid ambient. *The Journal of chemical physics*, 124(17):174712, 2006.

[53] BNJ Persson. Capillary adhesion between elastic solids with randomly rough surfaces. *Journal of Physics: Condensed Matter*, 20(31):315007, 2008.

[54] Anna L Barnette, David B Asay, Don Kim, Benjamin D Guyer, Hanim Lim, Michael J Janik, and Seong H Kim. Experimental and density functional theory study of the tribochemical wear behavior of SiO_2 in humid and alcohol vapor environments. *Langmuir*, 25(22):13052–13061, 2009.

[55] L Chen, YJ Yang, HT He, SH Kim, and LM Qian. Effect of coadsorption of water and alcohol vapor on the nanowear of silicon. *Wear*, 332:879–884, 2015.

[56] Olivier Noel, Pierre-Emmanuel Mazeran, and Hussein Nasrallah. Sliding velocity dependence of adhesion in a nanometer-sized contact. *Physical review letters*, 108(1):015503, 2012.

Appendices

APPENDIX A

Wear particle dynamics drive the difference between repeated and non-repeated reciprocated sliding

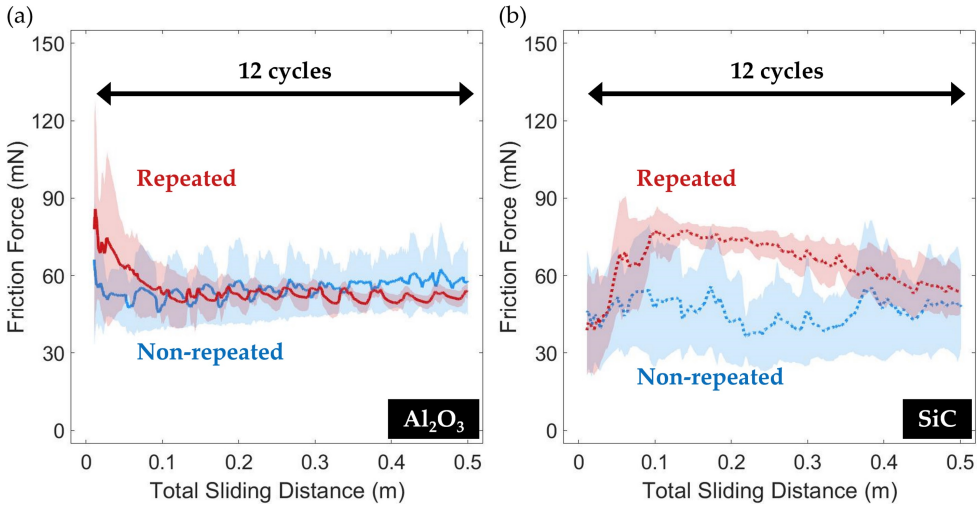

Figure A.1: The frictional force measured during the first 12 cycles in repeated and non-repeated experiments, emphasizing the running-in behavior in the repeated experiments. (a) Sapphire-on-Si wafer and (b) SiC-on-Si wafer experiments.

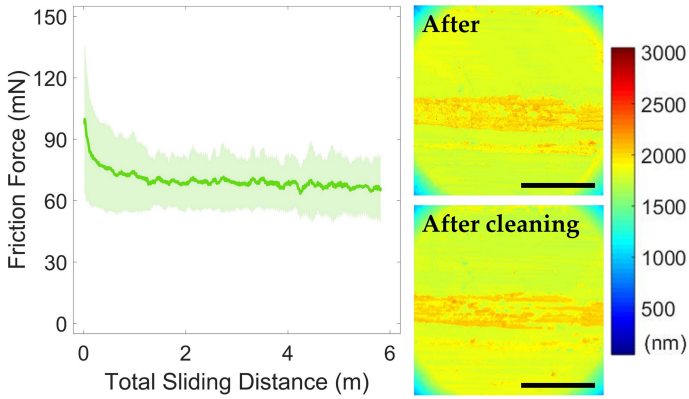

Figure A.2: Third body formation during non-repeated sliding. A thin third body that could be washed off by sonicating the sapphire sphere in acetone was observed on the wear scar on the sapphire ball after a non-repeated experiment. The friction behavior for this particular experiment is consistent with that observed in all repeated experiments. Scale bars, 50 μm.

Table A.1.1: Wear mechanisms predominantly involved at the contact interface with sliding distance.

Sapphire-on-Si wafer			
Sliding mode	**Contact surface**	**Sliding distance (m)**	**Wear mechanisms**
Repeated	Ball	0–1	Running-in behavior; Third body is formed and adheres to ball
		4–6	Third body on ball minimized wear
	Flat	0–1	Abrasive wear; Ploughing from pristine surface asperities on ball
		4–6	Third body on ball minimized wear
Non-repeated	Ball	0–1	Running-in behavior; Flattening of sharpest asperities
		4–6	Mild wear (adhesive wear in some cases)
	Flat	0–1	Abrasive wear (only first ∼cm)
		4–6	Mild wear

Table A.1.2: Wear mechanisms predominantly involved at the contact interface with sliding distance.

SiC-on-Si wafer			
Sliding mode	**Contact surface**	**Sliding distance (m)**	**Wear mechanisms**
Repeated	Ball	0–1	Running-in behavior; Removal of sharpest asperities, mild wear
		4–6	Mild wear; Abrasive wear resulting from compressed debris ridge formed on flat
	Flat	0–1	Abrasive wear and formation of compressed debris ridge in wear track
		4–6	Abrasive wear at either side of compressed debris ridge
Non-repeated	Ball	0–1	Abrasive wear
		4–6	Predominantly mild wear
	Flat	0–1	Abrasive wear
		4–6	Predominantly mild wear

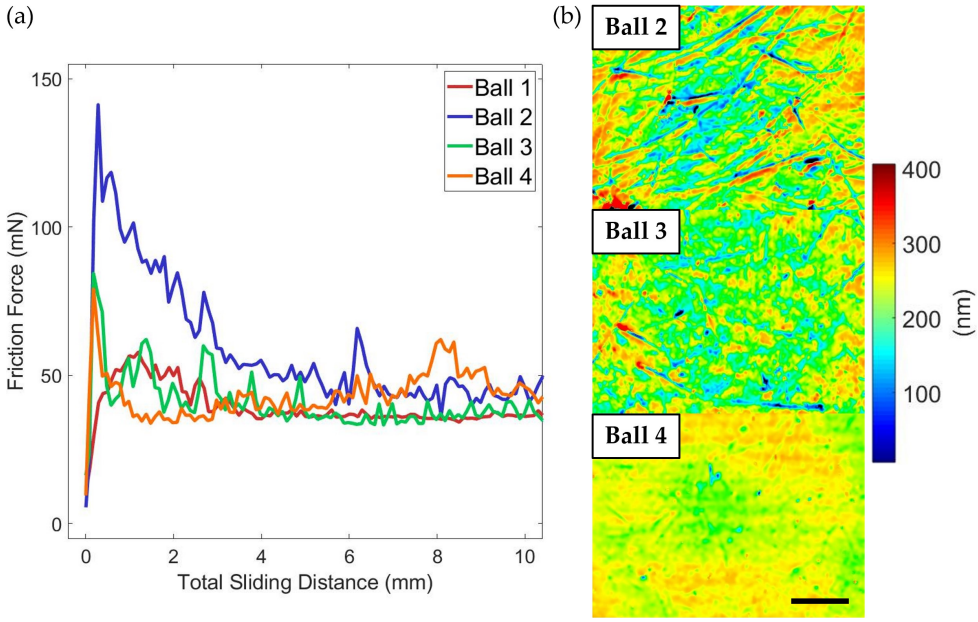

Figure A.3: Friction measurements for non-repeated sliding of sapphire-on-Si wafer and corresponding variation in ball topography. (a) Frictional force for 6 m sliding distance (same data as Figure 3.1a) (b) The RMS surface roughness measured by optical profilometry of Ball 2, Ball 3 and Ball 4 are 78 nm, 44 nm and 18 nm, respectively. Scale bar, 20 μm. There is a substantial ball-to-ball variation in the measured frictional forces as well as the ball topography: the highest frictional forces were measured using the smoothest ball, as expected based on the interpretation of the experiments that is presented in the main text.

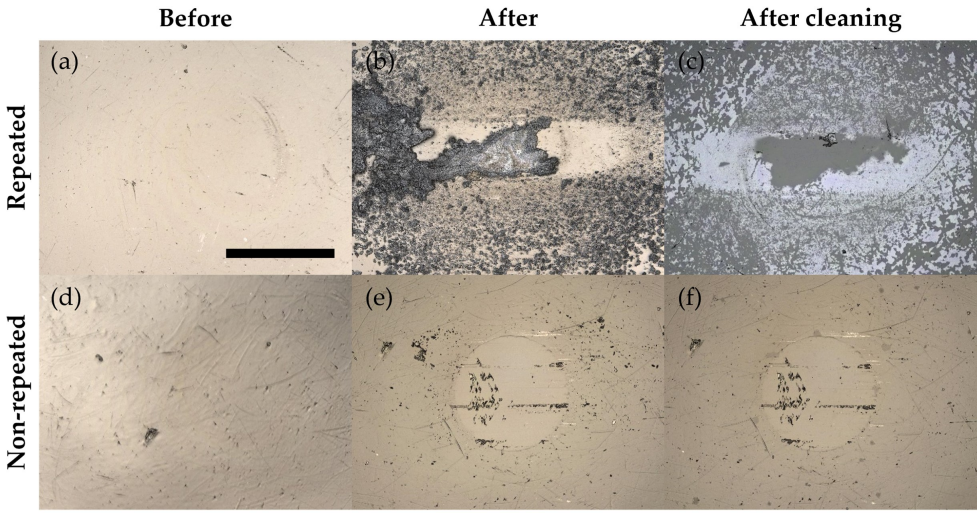

Figure A.4: Optical images of sapphire balls. (a),(d) Measured before the friction experiment. (b),(e) Measured after the friction experiment. (c),(f) Measured after ultrasonic cleaning of the ball after the friction experiment. Scale bar, 100 μm.

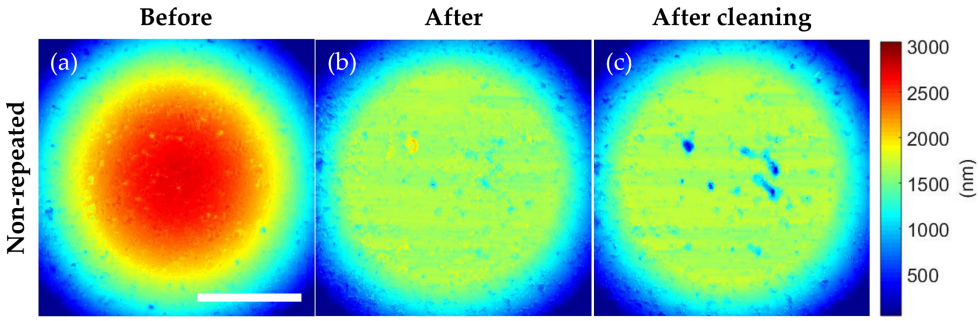

Figure A.5: *Ex situ* height profiles of SiC ball. (a) Measured before and (b) after the friction experiment. (c) Measured after ultrasonic cleaning of the ball after the friction experiment. Scale bar, 50 μm.

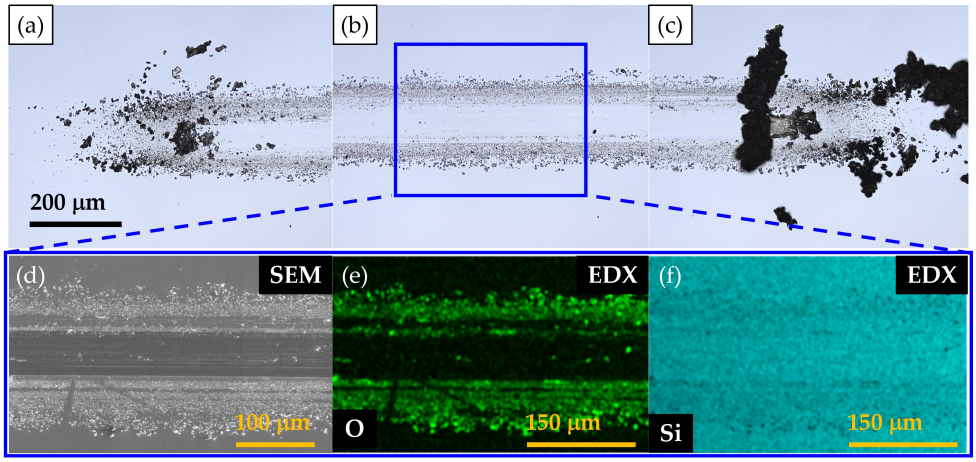

Figure A.6: Optical images and SEM-EDX analysis of the wear track on the Si substrate of the repeated sapphire-on-Si wafer experiment. Optical images of (a) Left and (c) Right ends of the wear track. (b),(d) Optical and SEM images of the wear track, respectively. The presence of the oxygen (O) signal in (e) and the absence of the Si signal in (f) indicate the formation of the SiO_x debris.

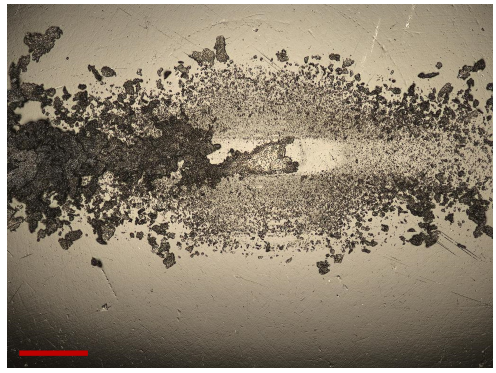

Figure A.7: Optical image of the sapphire ball after repeated sliding. Scale bar, 100 μm.

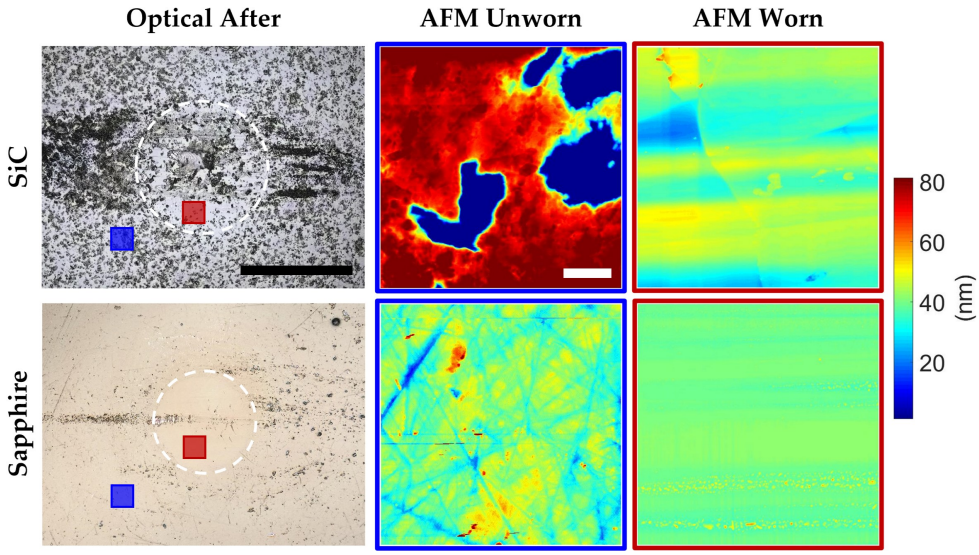

Figure A.8: Comparison of the surface topography of the sapphire and SiC balls before and after non-repeated sliding experiments. The blue and red shaded areas indicate where the AFM height mapping was performed on the unworn and worn regions on the balls. The scale bars for optical and AFM images are 100 μm and 1 μm, respectively.

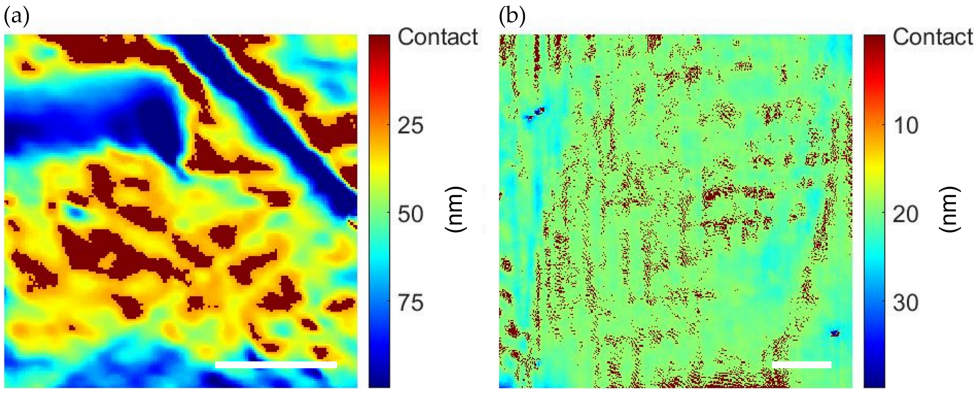

Figure A.9: Contact gap profiles (a) before and (b) after sliding. The surface height profiles for the BEM calculation are recorded by the profilometry. The normal force in the BEM calculation was scaled with the size of the height profiles of the ball compared to the area of the Hertzian contact before sliding and the area of apparent contact after sliding, ∼21 mN in both cases. The color scale shows the gap between contact surfaces where dark red regions indicate the contact part; 8.3 μm^2 before sliding and 60.5 μm^2 after sliding. Scale bars, 5 μm.

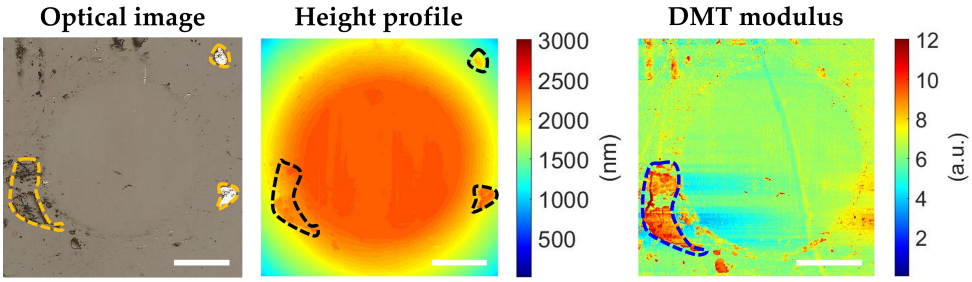

Figure A.10: The surface topography of wear scar on the sapphire ball after milling. Wear debris, highlighted by dashed lines, can be observed outside the wear scar but not in the contact zone; the worn region on the ball is higher than the debris. The local elastic modulus measured during PeakForce tapping mode AFM imaging of the worn ball signals contrast between the wear debris and the (worn) sapphire. Scale bars, 25 μm.

APPENDIX B

Rougher is more slippery

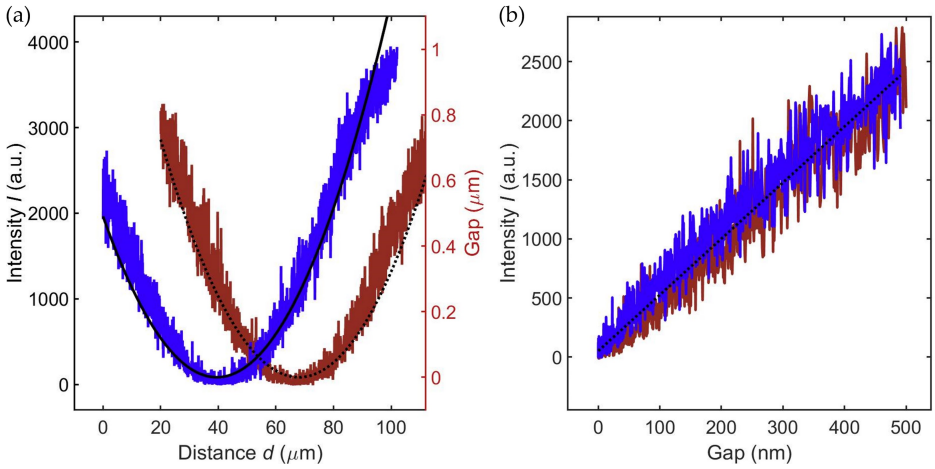

Figure B.1: Fluorescence intensity and local gap. Fluorescence is excited by an argon ion laser at a wavelength of 514 nm and the resulting emission light is detected through an emission filter BP 560|615. (a) Cross-sectional fluorescence intensity (I) profile taken through the sphere-on-flat contact center in both orthogonal in-plane directions (blue and red curves; the two curves were manually shifted for clarity). Black solid and dotted lines show the expected sphere-on-flat gap based on the sphere diameter and on the assumption that there is no roughness and no deformation. (b) Intensity as a function of the gap size for gaps smaller than 500 nm in both in-plane directions. The potted black line indicates a linear fit to the data.

Table B.1: Mechanical properties of Si_3N_4 and sapphire.

Materials	Young's modulus E (GPa)	Poisson's ratio ν	Hardness H (GPa)
Sapphire	335 [1]	0.25 [2]	20 [3]
Si_3N_4	205†	0.25†	23†

† Measured by nanoindentation (TI980, Bruker)

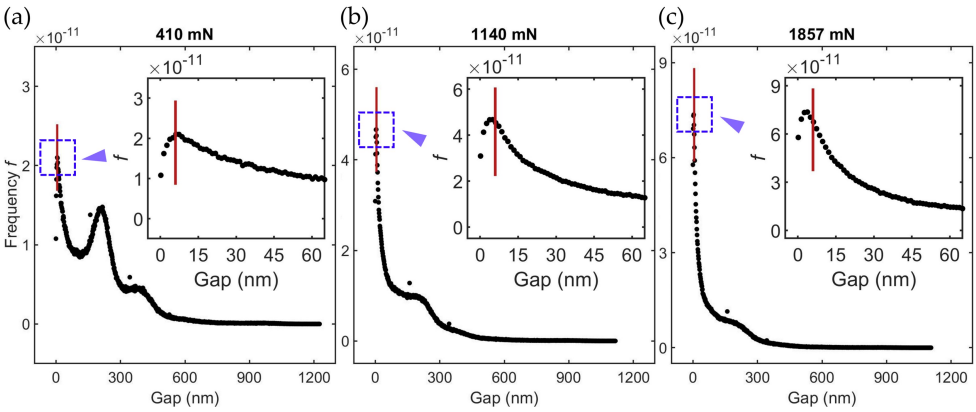

Figure B.2: Fluorescence intensity distribution as a function of the local gap. The fluorescence intensity shows a clear peak at a gap of ∼6 nm (red line, inset figures) at each normal force 410 mN (a), 1140 mN (b), and 1857 mN (c). The corresponding gap value at the peak position determines the threshold for the area of real contact in Figure 5.2.

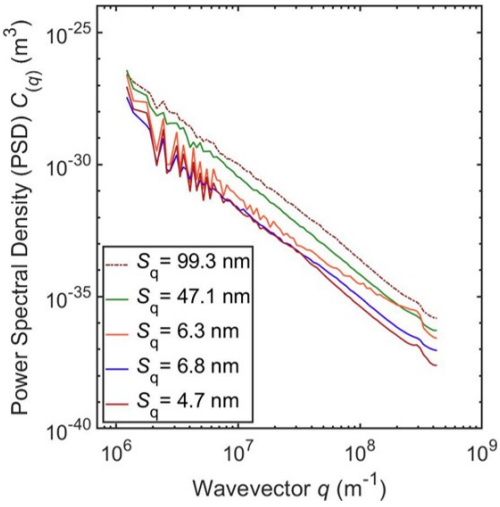

Figure B.3: The power spectral density (PSD) of the surface topography of Si_3N_4 with varying surface roughness. Each curve indicates the average of 3 AFM measurements taken on different locations on the same sphere. The size of the AFM topography is 10 μm $\times$ 10 μm with 95.4 nm^2 per pixel resolution.

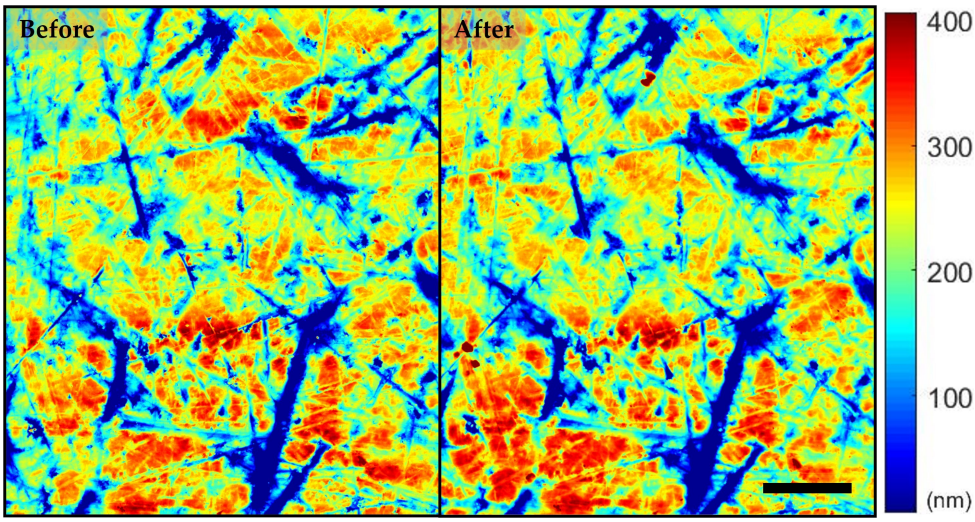

Figure B.4: Si_3N_4 sphere AFM topography before and after contact. A 2 N normal force was applied to the Si_3N_4 sphere against sapphire flat contact. The RMS roughness of the Si_3N_4 sphere is 90 nm. Scale bar, 10 μm.

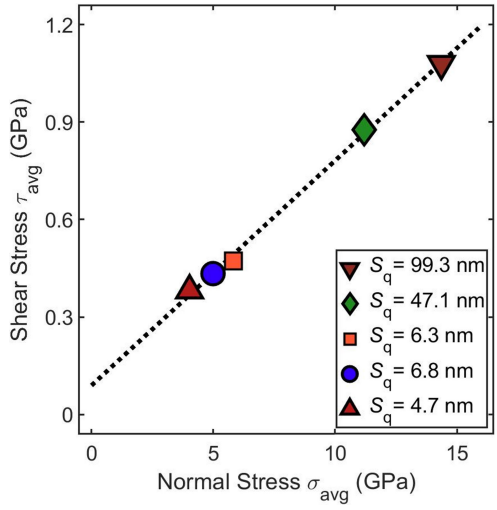

Figure B.5: Shear stress as a function of normal stress. The average shear stress (τ_{avg}) is calculated by multiplying the average normal stress (σ_{avg}), which is the inverse of the slope between the area of real contact as a function of normal force of Si_3N_4 sphere for different surface roughness (Figure 5.3a), to the average coefficient of friction (inset of Figure 5.3b).

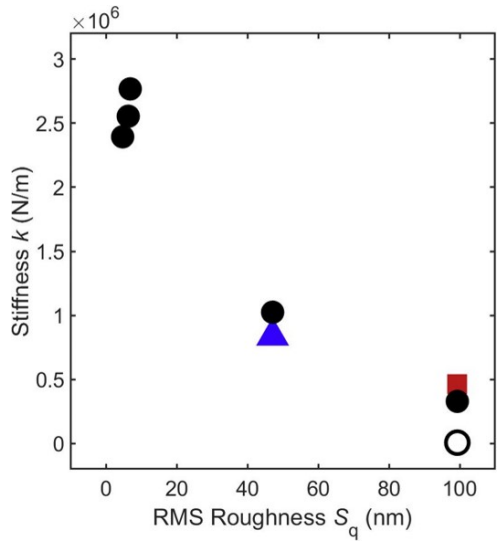

Figure B.6: Normal contact stiffness calculation with and without plasticity. The normal contact stiffness calculation without plasticity was conducted with the roughest Si_3N_4 sphere ($S_q = 99.3$ nm) as shown with open black circle mark. The lower stiffness without plasticity compared to with plasticity (solid black circle mark) is attributed to the fact that the highest asperity peaks on the sphere surface are provide a low stiffness when they are not plastically flattened.

Bibliography

[1] Seryeyohan Cho, Jihoon Jeong, Seungjin Hwang, and Tae Jun Yu. Thermal lens effect model of ti: sapphire for use in high-power laser amplifiers. *Applied Physics Express*, 11(9):092701, 2018.

[2] DJ Dumin. Deformation of and stress in epitaxial silicon films on single-crystal sapphire. *Journal of Applied Physics*, 36(9):2700–2703, 1965.

[3] Suat Pat, M Zafer Balbağ, and Şadan Korkmaz. Mechanical properties of deposited carbon thin films on sapphire substrates using atomic force microscopy (afm). *Ceramics International*, 40(7):10159–10162, 2014.

APPENDIX C

Contribution of capillary adhesion to macroscopic friction

C.1 Single nanoasperity adhesion calculation

We calculate the maximal adhesive force that results from the capillary bridge at the tip-on-substrate interface. This adhesive force consists of three contributions; the capillary force (F_c), the tension force (F_t) and the van der Waals force (F_v), $\overrightarrow{F_{ad}} = \overrightarrow{F_c} + \overrightarrow{F_t} + \overrightarrow{F_v}$. The capillary force (Equation C.1) results from the pressure difference inside and outside the meniscus known as the Laplace pressure ($P_{Laplace}$), which then acts on the circular projected area within which the meniscus wets the tip ($A = \pi R'^2$), as illustrated in inset of Figure 6.1b:

$$|F_c| = P_{Laplace} A = \gamma(\frac{1}{r_1} + \frac{1}{r_2})\pi R'^2 \tag{C.1}$$

where γ is the liquid-vapor surface tension, r_1 is the positive meniscus neck radius and r_2 ($= \frac{d_c}{2}$, d_c is critical distance of nucleation) is the negative curvature of the meniscus in the normal direction. The parameters for the calculation of the capillary force are listed in Table C.1. The second contribution to the adhesive force, the tension force (Equation C.2), acts along the circular contact line on the AFM tip and is described by:

$$|F_t| = 2\pi R' \gamma \cos\alpha \sin\beta \tag{C.2}$$

where α is the meniscus-tip contact angle, and β is the angle between the normal axis of the tip and the vector that connects the center of the (spherical) tip to the meniscus-tip contact line (see inset of Figure 6.1b). The relation between R' and r can be approximated by: $R' = 2(R_{tip} r + R_{tip} h)^{\frac{1}{2}} - r$ where R_{tip} is the tip apex radius and h is the condensate thickness [1]. We estimated the apex radius of the AFM tip to be $R_{tip} = 26$ nm and 30 nm through the tip qualification method (see Appendix C.2). The meniscus-tip contact angle and the liquid-vapor surface tension are set to $\alpha = 40°$ [2] and $\gamma = 72.8$ mN/m [1] for water. The last contribution to the adhesive force is the van der Waals force. The van der Waals interactions between SiO_2-air-SiO_2 and SiO_2-water-SiO_2 can be described by Equation C.3 [2]:

$$|F_v| = (H_{air}(1 - A_{Rel}) + H_{water} A_{Rel}) \frac{R_{tip}}{6 d_a^2} \tag{C.3}$$

where $H_{air} = 10.38 \times 10^{-20}$ J and $H_{water} = 1.9 \times 10^{-20}$ J are the Hamaker constants for the interfaces of SiO_2-air-SiO_2 and SiO_2-water-SiO_2, respectively, and da (0.2 nm) is the average distance between atoms [2]. The adhesive force that is then calculated using the model is 54 ± 4 nN.

C.2 AFM tip radius determination

To compare theoretical predictions of the adhesive force to AFM measurements, we estimated the AFM tip radii (R_{tip}) using a tip reconstruction method [3]. Within this method, a titanium sample with sharp edges (RS-12M, Bruker) is scanned by the AFM tip over an area of 5 μm $\times$ 2.5 μm using Bruker PeakForce QNM mode. The tip geometry can then be extracted from the measured topography through deconvolution (NanoScope Analysis, Bruker) (Figure C.1). By fitting a circle to the (2D) height profile of the reconstructed tip, we can estimate the tip radius.

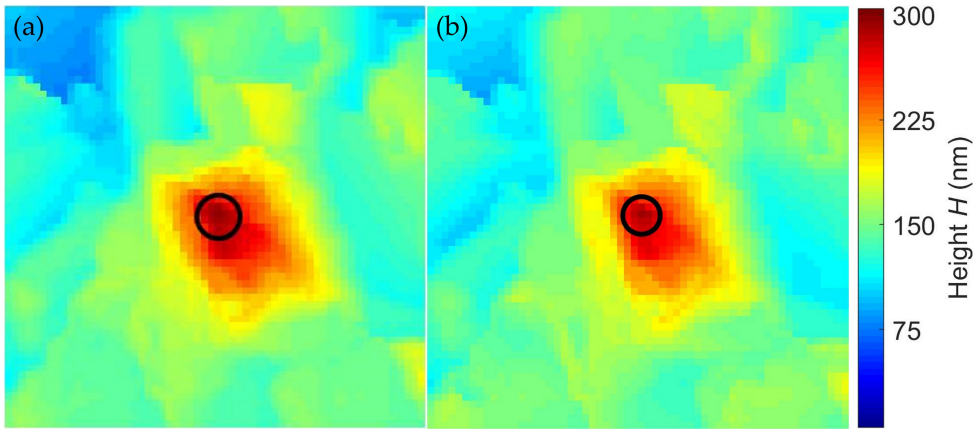

Figure C.1: AFM tip radius characterization. The reconstructed geometrical height map of the tip apex. The black circle is fitted to the spherical shape of the tip apex where the radius of the circle or the tip radius (R_{tip}) is given as 30 nm (a) and 26 nm (b). For the fitting process, we estimated the tip radius to be the smallest circumference of the tip apex determined.

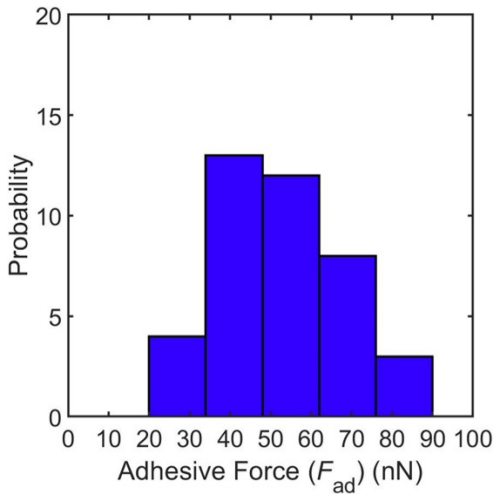

Figure C.2: Probability distribution of the adhesive force (F_{ad}) measured in water vapor environment ($58 \pm 0.7\%$ RH). The distribution of the adhesive force obtained through 40 AFM pull-off force measurements at different locations on the Si wafer (see Experiments 6.2.1). The mean adhesive force is 52 nN with a standard deviation of 15 nN.

Table C.1: Condensate thickness (h) and critical distance (d_c) of water and isopropanol (IPA) at different relative humidity (RH) and partial pressure (P/P_{sat}).

Vapors	**RH (%)**	**Thickness h (nm)** [4]	**Critical distance d_c (nm)** [5]
Water	58	1.18	3.0
Water	50	1.11	2.5
Water	40	0.98	2.1
Vapors	**P/P_{sat} (%)**	**Thickness h (nm)** [6]	**Critical distance d_c (nm)** [7]
IPA	70	0.60	4.0[†]
IPA	45	0.51	2.8
IPA	30	0.46	2.3
IPA	10	0.29	1.6

[†] The critical distance at $P/P_{sat} = 70\%$ is extrapolated by the value of the linear correlation between critical distance and IPA partial pressure at 10–45%.

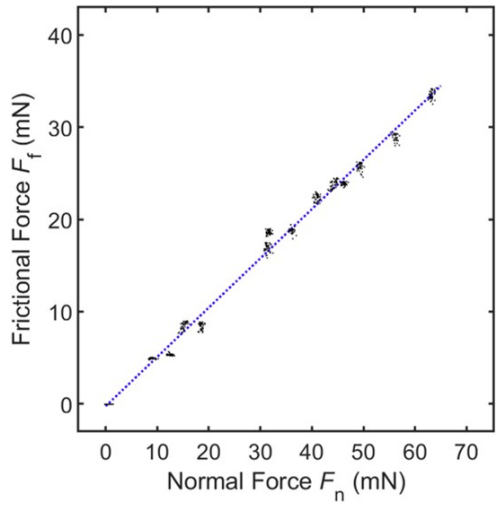

Figure C.3: Frictional force as a function of normal force for the contact between a Si ball and a Si wafer. The measured frictional force (black dots) linearly increases with the applied normal force at 1 µm/s sliding speed in ambient environment (36% RH; 20.3 °C). The linear fitting line is extended to the origin of the graph, indicating that the coefficient of friction (CoF) is well defined: $\mathrm{CoF} = \frac{F_\mathrm{f}}{F_\mathrm{n}}$, with F_f the frictional force and F_n the normal force.

Table C.2: Mechanical properties of the Si ball and the Si wafer.

Young's modulus E (GPa)	**Poisson's ratio ν**	**Hardness H (GPa)**
130	0.2	10

Table C.3: Total sliding distance and Wear volume of Si ball samples.

Samples	**Total sliding distance D_{Tot} (μm)**	**Wear volume $\times$ 10^9 (nm)^3**
1	190	4.75
2	180	4.09
3	180	2.77
4	270	5.76

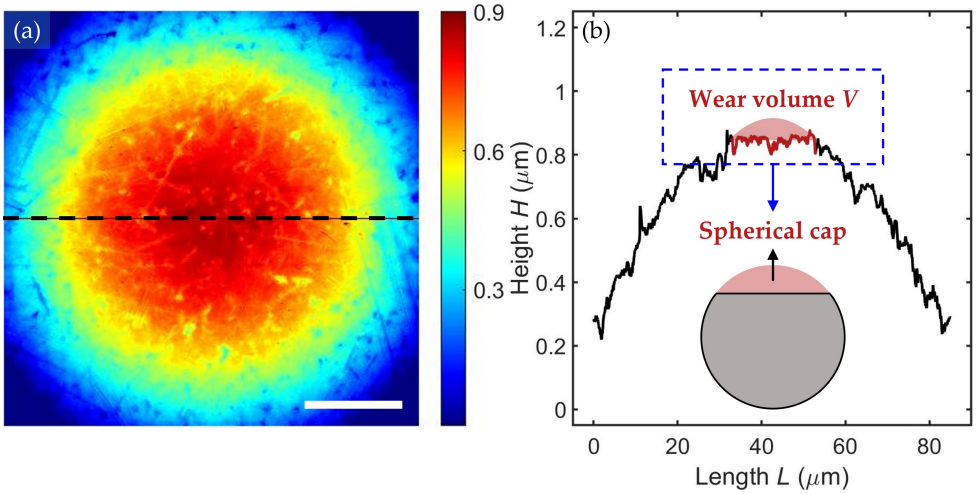

Figure C.4: Wear volume calculation. (a) The AFM surface topography of a Si ball after sliding. (b) The cross-sectional height profile through the wear scar (dashed line in (a)). The wear volume (V) is calculated by assuming that the lost material forms a spherical cap the base diameter of which is equal to the diameter of the wear scar. Scale bar, 20 μm.

Bibliography

[1] David B Asay and Seong H Kim. Effects of adsorbed water layer structure on adhesion force of silicon oxide nanoasperity contact in humid ambient. *The Journal of chemical physics*, 124(17):174712, 2006.

[2] Miroslav Bartošík, Lukáš Kormoš, Lukáš Flajšman, Radek Kalousek, Jindřich Mach, Zuzana Lišková, David Nezval, Vojtěch Švarc, Tomáš Šamořil, and Tomáš Šikola. Nanometer-sized water bridge and pull-off force in afm at different relative humidities: Reproducibility measurement and model based on surface tension change. *The Journal of Physical Chemistry B*, 121(3):610–619, 2017.

[3] Daan Vorselen, Ernst S Kooreman, Gijs JL Wuite, and Wouter H Roos. Controlled tip wear on high roughness surfaces yields gradual broadening and rounding of cantilever tips. *Scientific reports*, 6(1):1–7, 2016.

[4] David B Asay and Seong H Kim. Evolution of the adsorbed water layer structure on silicon oxide at room temperature. *The Journal of Physical Chemistry B*, 109(35):16760–16763, 2005.

[5] Seongsoo Kim, Dohyun Kim, Jongwoo Kim, Sangmin An, and Wonho Jhe. Direct evidence for curvature-dependent surface tension in capillary condensation: Kelvin equation at molecular scale. *Physical Review X*, 8(4):041046, 2018.

[6] Anna L Barnette, David B Asay, Michael J Janik, and Seong H Kim. Adsorption isotherm and orientation of alcohols on hydrophilic SiO_2 under ambient conditions. *The Journal of Physical Chemistry C*, 113(24):10632–10641, 2009.

[7] Dohyun Kim, Jongwoo Kim, Jonggeun Hwang, Dongha Shin, Sangmin An, and Wonho Jhe. Direct measurement of curvature-dependent surface tension of an alcohol nanomeniscus. *Nanoscale*, 13(14):6991–6996, 2021.

Summary

500 years ago, Leonardo da Vinci systematically investigated the relation between the frictional force and normal force. Da Vinci concluded that the frictional force is proportional to the normal force. The proportionality constant that links the frictional force and normal force is defined as the coefficient of friction (CoF). Although the CoF is an empirical number that resulted from da Vinci's experiments and does not explain the fundamental origin of friction, this simple relation between frictional force and normal force successfully captures most dry sliding friction behavior between macroscopic objects. However, when the sliding surfaces strongly adhere to each other or are atomically smooth, the proportionality between frictional force and normal force may breakdown and, in this case, the frictional force is proportional to the area of real contact. John Frederick Archard proposed a simple multiple-contacts model in which the cross-sectional area of the contact points is increased linearly with applied load when the contact points are plastically deformed. More analytical models have been proposed, such as the Greenwood and Williamson (GW) model and Persson's contact theory, to quantify the area of real contact at multi-asperity interfaces. Experimentally it remains challenging to access and measure the area of real contact hidden from view by the contacting objects. To quantify the area of real contact, numerical methods, such as the boundary element method, have been developed. The calculation of contact mechanics either by analytical or numerical methods provides further insight into the formation of contacts which leads to friction.

In the **Introduction Chapter**, we provide a brief overview of several aspects of friction beginning with how we naturally learn how to manage friction, for instance preventing falling down while walking on ice or rubbing our hands to warm up in the winter. We then discussed how ancient civilizations such as the ancient Egyptians and Chinese managed to reduce friction to transport massive objects. These examples show the strong relevance of friction to our daily life, and that understanding friction is non-trivial. Nowadays, friction not only influences us individually but also shows great impact on the environment and economy. A large fraction of the global energy consumption is directly or indirectly due to friction. This

motivates a significant research effort directed towards understanding and reducing friction. In the second part of the **Introduction**, we summarized the findings from the sliding experiments conducted by Leonardo da Vinci. Da Vinci's results were later confirmed by Guillaume Amontons and Charles-Augustin Coulomb: frictional force is proportional to the normal force and frictional force is independent of the apparent area of contact and sliding velocity. The dependence of friction on the normal force, contact area and sliding speed found by da Vinci, Amontons and Coulomb generally holds for most dry macroscopic sliding systems. However, in later studies reported by Frank Philip Bowden, David Tabor and John Frederick Archard, frictional force was found to be proportional to the area of real contact at multi-asperity interfaces. The proposed relation between friction and contact area raised interest in the development of contact models that could predict the area of real contact. We briefly discussed the differences between two common analytical models–the GW model and Persson's model–that calculate the area of real contact between rough surfaces. In the third part of the **Introduction**, we introduced the effect of capillary adhesion on friction. Water vapor condensation on surfaces is ubiquitous in ambient environments. In fact, even in high vacuum environments, the water absorbed onto surfaces is difficult to remove without heating up the vacuum chamber. At sliding interfaces, liquid bridges form across the surfaces due to capillary condensation–capillary bridges–leading to an increase of the normal force and thus the frictional force as expected from Amontons' second law. Other factors, such as the evolution of the surface topography due to wear and the accumulation of wear debris at the sliding interface, also influence the friction behavior.

In this thesis, we study the interplay between friction, capillary adhesion, surface topography and third body formation at multi-asperity interfaces. We aim to bridge the gap between macroscopic friction behavior and nanoscale surface features and interfacial phenomena. In **Chapter 2**, we introduce experimental techniques and numerical methods that were applied throughout the thesis. We introduce sphere-on-flat friction measurements between ceramic materials, including sapphire (Al_2O_3), SiC, Si_3N_4, glass and Si. Surface characterization techniques to measure the surface topography from the nanoscale to the microscale as well as boundary element method (BEM) contact calculations to simulate the contact geometry resulting from different materials, surface topographies and applied loads are discussed. A state-of-art visualization method is introduced to measure the area of real contact and normal contact stiffness at multi-asperity interfaces.

In **Chapter 3**, we investigated the impact of two distinct sliding modes–repeated and non-repeated reciprocated sliding–on friction and wear behavior at sphere-on-

flat interfaces. The non-repeated sliding was designed to prevent the sphere from continuously contacting the same worn counter surface. We observed that during repeated sliding of the sphere on the counter surface wear debris was collected at the interface forming a third body that stabilized the friction and prevented wear of the sphere while the third body formation was much less evident during non-repeated sliding, which resulted in increasing friction. The observed continuous increase in friction scaled with the increase of the area of apparent contact and is attributed to a reduction in roughness and an increase in adhesion. In both sliding modes, the friction decreased during the very first strokes, behavior that is often referred to as running-in. In **Chapter 4**, we presented friction experiments in which a SiC sphere is slid against a Si flat in a unidirectional fashion. By comparing the sphere surface topographies measured before and after sliding using atomic force microscopy (AFM), we found that the decrease of friction during running-in originated from the wear behavior of asperities. The asperities on the sphere were removed during sliding thereby reducing the effect of ploughing of the asperities of the SiC sphere into the Si flat. The reduction in ploughing led to the reduction of ploughing friction during running-in. We then performed BEM contact calculations to analyze the microscale contact mechanics in relation to the friction behavior at single asperity level. Contact calculations suggested that the overall contact pressure exerted by contacting asperities decreased after sliding, which indicates that less asperity level ploughing is expected. However, we found that the contact calculations cannot reliably predict multi-asperity friction. After running-in, the asperity scale wear transitions from ploughing wear to mild wear.

In **Chapter 5**, we discussed the classical topic of the interplay between frictional force, normal force and area of real contact at multi-asperity interfaces. We systematically manipulated the surface roughness of Si_3N_4 spheres to control the area of real contact. To quantify the area of real contact, we employed BEM contact calculations and contact visualization experiments to reveal the relation between surface roughness and the area of real contact at the asperity level. Both numerical and experimental methods demonstrate that the area of real contact increases with increasing applied load and decreasing surface roughness. To correlate the contact area with the frictional and normal force, we slid Si_3N_4 spheres with varying surface roughness on a sapphire flat at various normal forces and measured the frictional force. The experiments and calculations showed that the frictional force linearly increased with the applied load. Furthermore, the various Si_3N_4 sphere surface topographies resulted in up to 400% variation in the area of real contact, calculated at the same normal load. Nonetheless, the frictional force only showed a variation of

up to 20% with varying surface roughness. Our results show that Amontons' law holds for macroscopic contacts between Si_3N_4 spheres with varying roughness and a sapphire flat. However, we did observe a modest increase in CoF for smoother surfaces that was attributed to the formation of capillary bridges across the interface leading to an increase in the interfacial normal load. A capillary adhesion model was presented to calculate the change in capillary adhesion as a function of surface topography at multi-asperity interfaces. The adhesion model bridges asperity level contact formation and capillarity to macroscopic friction behavior. Surface topography not only impacts adhesion but also the stiffness of the interface. We applied the contact visualization method to directly measure the interfacial normal stiffness via the fluorescence intensity and demonstrated that the normal stiffness decreases with increasing surface roughness, in agreement with the stiffness predicted by BEM contact calculations. The message delivered in **Chapter 5** stated that at microscopic non adhering multi-asperity interfaces the adhesive friction is controlled by the load and independent of the surface topography, unless the topography becomes so smooth that large sections of the apparent area of contact become covered with capillary bridges. In this regime of low surface roughness, the friction will scale with the apparent area of contact, as demonstrated in **Chapter 3**.

In **Chapter 6**, we casted our focus toward engineering applications in the semiconductor industry involving contact formation and friction behavior at multi-asperity interfaces. In humid environments, the contacts are influenced by capillary condensation of water at interfaces. We performed single asperity AFM-based pull-off experiments to quantify the capillary adhesion between Si surfaces. A distinct capillary force was measured when pulling off the Si AFM probe from a Si wafer in humid conditions, while no such adhesion was observed when the experiment was repeated in a water immersed environment. However, when we repeated the experiment with a millimeter Si sphere–instead of a sharp AFM tip–the distinct pull-off force corresponding to capillary adhesion was not observed. No pull-off force was detected because capillary adhesion is cancelled by the elastic energy stored in deformed asperities at the interface. This is known as the adhesion paradox. Inspired by the work presented in **Chapter 5**, we alternatively measured the capillary adhesion exerted at the multi-asperity interfaces via friction. We performed Si sphere-on-Si wafer friction experiments in ambient and immersed conditions and converted the difference in frictional force into a capillary adhesive force. Mild wear was observed on the surface of the sphere after friction measurements. We incorporated the effect of the changing surface topography into our capillary adhesion model. Furthermore, we demonstrated that capillary adhesion at the interfaces is strongly reduced when

water is replaced with isopropanol (IPA) due to the lower liquid surface tension of IPA. Finally, we observed a difference in friction measured in water and IPA immersed environments, in the absence of capillary adhesion. We attributed the reduction of the frictional force in IPA immersed conditions to boundary lubrication.

To conclude, in this thesis we experimentally and numerically investigated several factors that influence friction and wear behavior, including the dynamics of third bodies at the sliding interface, the area of real contact, capillary adhesion and surface tension. We established a non-repeated sliding method that minimizes the accumulation of wear debris at the sliding interface providing a unique opportunity to understand fundamental mechanisms that govern macroscopic friction. We provided new insights into the relation between friction, surface topography and capillary adhesion at multi-asperity interfaces. Insight into asperity-level contact phenomena at the nanoscale was connected to friction behavior observed at macroscopic ceramic contacts. Our work contributes to linking fundamental insights into friction and wear from the laboratory scale to industrial applications or daily life activities in which reducing or manipulating friction and wear is of importance.

Samenvatting

Nanoschaal ruwheid en slijtage van grensvlakken tussen keramische materialen en hun effect op macroscopische wrijving

500 jaar geleden onderzocht Leonardo da Vinci al systematisch de relatie tussen de wrijvingskracht en de normaalkracht. Da Vinci concludeerde dat de wrijvingskracht evenredig is met de normaalkracht. De evenredigheidsconstante die de wrijvingskracht en de normaalkracht met elkaar verbindt, wordt gedefinieerd als de wrijvingscoëfficiënt (CoF). Hoewel de CoF een empirisch getal is dat voortvloeit uit da Vinci's experimenten en niet de fundamentele oorsprong van wrijving verklaart, omschrijft deze eenvoudige relatie tussen wrijvingskracht en normaalkracht met succes het droge wrijvingsgedrag tussen macroscopische objecten. Echter, wanneer de glijdende oppervlakken aan elkaar kleven of zeer glad zijn, is wrijvingskracht niet langer evenredig aan de normaalkracht en, in dit geval, is de wrijvingskracht evenredig met de oppervlakte van het werkelijke nanoscopicsche contact van de twee oppervlakten. John Frederick Archard stelde een eenvoudig meervoudig-contactmodel voor waarin de doorsnede van de contactpunten lineair toeneemt met de uitgeoefende belasting wanneer de contactpunten plastisch vervormen. Er zijn meer analytische modellen voorgesteld, zoals het model van Greenwood en Williamson (GW) en de contacttheorie van Persson, om de oppervlakte van het werkelijke contact bij macroscopische grensvlakken te kwantificeren. Experimenteel blijft het een uitdaging om de oppervlakte van het echte contact, aan het zicht onttrokken door de voorwerpen zelf, te bestuderen en de echte contact oppervlakte te kwantificeren. Voor de kwantificatie zijn numerieke methoden ontwikkeld, zoals de grenselementmethode. De berekening van de contactmechanica met behulp van analytische of numerieke methoden verschaft verder inzicht in de vorming van de contacten die tot wrijving leidt.

In de **Inleiding** geven we een kort overzicht van verschillende aspecten van wrijving. We beginnen met hoe we van nature leren met wrijving om te gaan, bijvoorbeeld door te voorkomen dat we vallen terwijl we over ijs lopen of door in onze handen te wrijven om ons op te warmen in de winter. Vervolgens bespreken we

hoe oude beschavingen, zoals de oude Egyptenaren en de Chinezen, erin slaagden wrijving te verminderen en massieve voorwerpen te vervoeren. Uit deze voorbeelden blijkt hoe belangrijk wrijving in ons dagelijks leven is, en dat het begrijpen van wrijving toepassingen heeft overal om ons heen. Tegenwoordig beïnvloedt wrijving ons niet alleen individueel, maar heeft zij ook een grote invloed op het milieu en de economie. Een groot deel van het wereldwijde energieverbruik is direct, of indirect, het gevolg van wrijving. Dit motiveert een aanzienlijke onderzoeksinspanning gericht op het begrijpen en verminderen van wrijving. We hebben al gesproken over de glijdende experimenten van Leonardo da Vinci. De resultaten van Da Vinci werden later bevestigd door Guillaume Amontons en Charles-Augustin Coulomb, nu betere bekend als Amontons' wetten voor de wrijving: 'de wrijvingskracht is evenredig met de normaalkracht' en 'de wrijvingskracht is onafhankelijk van het schijnbare contactoppervlak en de glijsnelheid'. De door da Vinci, Amontons en Coulomb gevonden evenredigheid van de wrijving met de normaalkracht, onafhankelijk van het contactoppervlak en de glijsnelheid geldt in het algemeen voor de meeste droge macroscopische glijsystemen. In latere studies, gerapporteerd door Frank Philip Bowden, David Tabor en John Frederick Archard, bleek de wrijvingskracht echter evenredig te zijn met de oppervlakte van het werkelijke contact bij 'multi-asperity interfaces'. De voorgestelde relatie tussen wrijving en contactoppervlak wekte belangstelling voor de ontwikkeling van contactmodellen die het oppervlak van echt contact konden voorspellen. We bespraken kort de verschillen tussen twee gangbare analytische modellen–het GW model en Persson's model–die de oppervlakte van echt contact tussen ruwe oppervlakken berekenen. In het derde deel van de **Inleiding** introduceerden wij het effect van capillaire adhesie op wrijving. Condensatie van waterdamp op oppervlakken is alomtegenwoordig in een atmospherische omgeving. Zelfs in hoogvacuüm-omgevingen is het op oppervlakken geabsorbeerde water moeilijk te verwijderen zonder de vacuümkamer op te warmen. Bij glijdende oppervlakken vormen zich vloeistofbruggen over de oppervlakken als gevolg van capillaire condensatie–capillaire bruggen–welke leiden tot een toename van de normaalkracht en dus van de wrijvingskracht zoals verwacht volgens de tweede wet van Amonton. Andere factoren, zoals de evolutie van de oppervlaktetopografie als gevolg van slijtage en de ophoping van slijtagepuin, beïnvloeden ook het wrijvingsgedrag.

In dit proefschrift bestuderen we de wisselwerking tussen wrijving, capillaire adhesie, oppervlaktetopografie en de vorming van derde lichamen bij macroscopische grensvlakken. We proberen een brug te slaan tussen macroscopisch wrijvingsgedrag en nanoschaal oppervlakte-kenmerken en fenomenen. In **Hoofdstuk 2** introduceren

we experimentele technieken en numerieke methoden die in het gehele proefschrift zijn toegepast. We introduceren bol-op-vlak wrijvingsmetingen tussen keramische materialen, waaronder saffier (Al_2O_3), SiC, Si_3N_4, glas en Si. Technieken voor oppervlaktekarakterisatie om de oppervlaktetopografie van de nanoschaal tot de microschaal te meten, evenals BEM-contactberekeningen om de contactgeometrie te simuleren die het resultaat is van verschillende materialen, oppervlaktetopografieën en toegepaste belastingen, worden besproken. Een state-of-art visualisatie methode wordt geïntroduceerd om de oppervlakte van het werkelijke contact en de normale contactstijfheid te meten bij multi-asperity interfaces.

In **Hoofdstuk 3** onderzoeken we de invloed van twee verschillende meetmethodes voor wrijving. Herhaald over hetzelfde oppervlake of niet-herhaald, steeds op een ongesleten oppervlakte. We vergelijken het verschill van de twee methodes op de wrijving en het slijtagegedrag bij bol-op-vlak oppervlaktes. Het niet-herhaaldelijk glijden was bedoeld om te voorkomen dat de bol voortdurend in contact zou komen met hetzelfde uitgesleten tegenoppervlak. Wij stelden vast dat tijdens het herhaaldelijk glijden van de bol op het tegenoppervlak slijtagepuin werd verzameld bij het grensvlak en een derde lichaam vormde dat de wrijving stabiliseerde en slijtage van de bol verhinderde, terwijl de vorming van het derde lichaam veel minder duidelijk was tijdens het niet herhaaldelijk glijden, wat resulteerde in toenemende wrijving. De waargenomen voortdurende toename van de wrijving schaalt met de toename van het gebied van schijnbaar contact en wordt toegeschreven aan een vermindering van de ruwheid en een toename van de adhesie. Bij beide glijwijzen nam de wrijving af tijdens de allereerste slagen, een gedrag dat vaak wordt aangeduid als 'inlopen'. In **Hoofdstuk 4** hebben wij wrijvingsexperimenten gepresenteerd waarbij een SiC-bol in één richting tegen een Si vlak wordt geschoven. Door de oppervlaktetopografie van de bol te vergelijken, gemeten voor en na het schuiven met behulp van atoomkrachtmicroscopie (AFM), ontdekten we dat de afname van de wrijving tijdens het inlopen veroorzaakt werd door het slijtagegedrag van de contactpunten, de topografiepieken die in contact komen. Deze uiteindes op de bol werden tijdens het glijden verwijderd, waardoor het effect van het ploegen van de pieken van de SiC-bol in de Si vlakte werd verminderd. De vermindering van het ploegen leidde tot een vermindering van de ploegwrijving tijdens het inlopen. Vervolgens voerden we BEM-contactberekeningen uit om de contactmechanica op microscopische schaal te analyseren in relatie tot het wrijvingsgedrag op microcontactniveau. Contactberekeningen suggereren dat de totale contactdruk uitgeoefend door microcontacten afneemt na het glijden, wat aangeeft dat minder ploegen op microcontactniveau wordt verwacht. We ontdekten echter dat de contactberekenin-

gen de macroscopische ploegwrijving niet betrouwbaar kunnen voorspellen. Na het inlopen gaat de slijtage van de microcontacten over van ploegslijtage naar milde slijtage.

In **Hoofdstuk 5** bespraken we het klassieke onderwerp van de wisselwerking tussen wrijvingskracht, normaalkracht en oppervlakte van echt contact bij macroscopische grensvlakken. Wij manipuleerden systematisch de oppervlakteruwheid van Si_3N_4 bollen om het gebied van echt contact te bestuderen. Om de oppervlakte van echt contact te kwantificeren, gebruikten we BEM-contactberekeningen en contactvisualisatie-experimenten om de relatie tussen oppervlakteruwheid en de oppervlakte van echt contact op het microcontactniveau te onthullen. Zowel numerieke als experimentele methodes tonen aan dat het oppervlakte van echt contact toeneemt met toenemende belasting en afnemende oppervlakteruwheid. Om het contactoppervlak te vergelijken met de wrijvings en normaalkracht, hebben we Si_3N_4 bolletjes met variërende oppervlakteruwheid op een saffier vlak geschoven bij verschillende normaalkrachten en hebben we de wrijvingskracht gemeten. Uit de experimenten en berekeningen bleek dat de wrijvingskracht lineair toenam met de uitgeoefende belasting. Bovendien resulteerden de verschillende topografieën van het Si_3N_4-boloppervlak in een variatie tot 400% van de oppervlakte van het werkelijke contact, berekend bij dezelfde normaalkracht. Niettemin vertoonde de wrijvingskracht slechts een variatie tot 20% met variërende oppervlakteruwheid. Onze resultaten tonen aan dat de wet van Amontons geldt voor macroscopische contacten tussen Si_3N_4 bollen met variërende ruwheid en een saffier vlak. We zagen echter een bescheiden toename in CoF voor gladdere oppervlakken die werd toegeschreven aan de vorming van capillaire bruggen over het grensvlak die leidt tot een effective toename van de belasting. Een capillair-adhesiemodel werd voorgesteld om de verandering in capillaire adhesie als functie van oppervlaktetopografie bij macroscopische grensvlakken te berekenen. Het adhesiemodel slaat een brug tussen contactvorming op microcontactniveau en capillariteit en macroscopisch wrijvingsgedrag. Oppervlaktetopografie beïnvloedt niet alleen de adhesie maar ook de stijfheid van het grensvlak. Wij pasten de contactvisualisatiemethode toe om de normale stijfheid van het grensvlak direct te meten via de fluorescentie-intensiteit en toonden aan dat de normale stijfheid afneemt met toenemende oppervlakteruwheid, in overeenstemming met de stijfheid voorspeld door BEM-contactberekeningen. De boodschap van **Hoofdstuk 5** stelde dat bij macroscopische niet-adhesieve grensvlakken de adhesieve wrijving gecontroleerd wordt door de belasting en onafhankelijk is van de oppervlaktetopografie, tenzij de topografie zo glad wordt dat grote delen van het schijnbare contactoppervlak bedekt worden met capillaire bruggen. In dit

regime van lage oppervlakteruwheid, zal de wrijving schalen met het schijnbare contactoppervlak, zoals aangetoond in **Hoofdstuk 3**.

In **Hoofdstuk 6** hebben we onze aandacht verlegd naar technische toepassingen in de halfgeleiderindustrie waarbij contactvorming en wrijvingsgedrag bij macroscopische grensvlakken een rol spelen. In vochtige omgevingen worden de contacten beïnvloed door capillaire condensatie van water. We voerden experimenten uit met AFM-gebaseerde adhesiemetingen om de capillaire adhesie tussen Si oppervlakken te kwantificeren. Een duidelijke capillaire kracht werd gemeten bij het aftrekken van de Si AFM probe van een Si wafer in vochtige omstandigheden, terwijl geen dergelijke adhesie werd waargenomen wanneer het experiment werd herhaald in een ondergedompeld water omgeving. Echter, wanneer we het experiment herhaalden met een millimeter Si bol–in plaats van een scherpe AFM tip werd de adhesie kracht die overeenkomt met capillaire hechting niet waargenomen. Er werd geen adhesiekracht gedetecteerd omdat capillaire adhesie wordt geannuleerd door de elastische energie opgeslagen in vervormde microcontacten op het grensvlak. Dit staat bekend als de adhesieparadox. Geïnspireerd door het werk gepresenteerd in **Hoofdstuk 5**, hebben we als alternatief de capillaire adhesie gemeten via wrijving. We voerden wrijvingsexperimenten uit met Si bol-op-Si wafers in droge en natte omgevingen en zetten het verschil in wrijvingskracht om in een capillaire adhesiekracht. Milde slijtage werd waargenomen op het oppervlak van de bol na wrijvingsmetingen. We hebben het effect van de veranderende oppervlaktetopografie in ons capillaire adhesiemodel opgenomen. Verder hebben we aangetoond dat de capillaire adhesie aan de grensvlakken sterk vermindert wanneer water wordt vervangen door isopropanol (IPA), vanwege de lagere vloeistofoppervlaktespanning van IPA. Tenslotte hebben wij een verschil waargenomen in wrijving gemeten in water en IPA ondergedompelde omgevingen, in de afwezigheid van capillaire adhesie. We schreven de vermindering van de wrijvingskracht in IPA-ondergedompelde omstandigheden toe aan grenssmering.

Samenvattend, hebben we in dit proefschrift experimenteel en numeriek onderzoek gedaan naar verschillende factoren die wrijving en slijtage beïnvloeden, waaronder de dynamica van derde lichamen op het glijvlak, de oppervlakte van het werkelijke contact, capillaire adhesie en oppervlaktespanning. We stelden een niet-herhaalde glijmethode op die de accumulatie van slijtagepuin aan het glijvlak minimaliseert en zo een unieke kans biedt om fundamentele mechanismen te begrijpen die macroscopische wrijving bepalen. We verschaften nieuwe inzichten in de relatie tussen wrijving, oppervlaktetopografie en capillaire adhesie bij macroscopische grensvlakken. Inzicht in contactfenomenen op het niveau van contacten op

nanoschaal werden in verband gebracht met wrijvingsgedrag dat werd waargenomen bij macroscopische keramische contacten. Ons werk draagt bij aan het koppelen van fundamentele inzichten in wrijving en slijtage van de laboratoriumschaal aan industriële toepassingen of activiteiten in het dagelijks leven waarbij het verminderen of manipuleren van wrijving en slijtage van belang is.

List of Publications

- **F.-C. Hsia**, F. M. Elam, D. Bonn, B. Weber, and S. E. Franklin
  "Wear particle dynamics drive the difference between repeated and non-repeated reciprocated sliding"
  Tribology International **142**, 105983, 2020, (Chapter 3)

- **F.-C. Hsia**[†], F. M. Elam[†], D. Bonn, B. Weber, and S. E. Franklin
  "Tracing single asperity wear in relation to macroscale friction during running-in"
  Tribology International, **162**, 107108, 2021, (Chapter 4)

- **F.-C. Hsia**, S. E. Franklin, P. Audebert, A. M. Brouwer, D. Bonn, and B. Weber
  "Rougher is more slippery: How adhesive friction decreases with increasing surface roughness due to the suppression of capillary adhesion"
  Physical Review Research, **3**, 043204, 2021, (Chapter 5)

- **F.-C. Hsia**, C.-C. Hsu, L. Peng, F. M. Elam, C. Xiao, S. E. Franklin, D. Bonn, and B. Weber
  "Contribution of capillary adhesion to friction at macroscopic solid-solid interfaces"
  Physical Review Applied, **17**, 034034, 2022, (Chapter 6)

Other topics by the author (2019–2023)

- X. Zhou, **F.-C. Hsia**, Y. Xue, D.-M. Tang, O. Cretu, C. Zhang, M. Mitome, Y. Bando, T. Sasaki, and D. Golberg
  "Tunable m echanical a nd e lectrical p roperties of c oaxial BN-C n anotubes"
  physica status solidi (RRL)–Rapid Research Letters, **13**, 1800576, 2019

- **F.-C. Hsia**, D.-M. Tang, W. Jevasuwan, N. Fukata, X. Zhou, M. Mitome, T. E.M. Nordling, and D. Golberg
  "Realization and direct observation of five normal and parametric modes in silicon nanowire resonators by in situ transmission electron microscopy"
  Nanoscale Advances, **1**, 1784, 2019

- R. W. Liefferink, **F.-C. Hsia**, B. Weber, and D. Bonn
  "Friction on ice: How temperature, pressure and speed control the slipperiness of ice"
  Physical Review X, **11**, 011025, 2021

- F. M. Elam, **F.-C. Hsia**, S. van Vlieta, R. Bliem, L. Yang, B. Weber, and S. E. Franklin
  "The influence of corrosion on diamond like carbon topography and friction at the nanoscale"
  Carbon, **179**, 590, 2021

- D.-M. Tang, S. V. Erohin, D. G. Kvashnin, V. A. Demin, O. Cretu, S. Jiang, L. Zhang, P.-X. Hou, G. Chen, D. N. Futaba, Y. Zheng, R. Xiang, X. Zhou, **F.-C. Hsia**, N. Kawamoto, M. Mitome, Y. Nemoto, F. Uesugi, M. Takeguchi, S. Maruyama, H.-M. Cheng, Y. Bando, C. Liu, P. B. Sorokin, and D. Golberg
  "Semiconductor nanochannels in metallic carbon nano tubes by thermomechanical chirality alteration"
  Science, **374**, 1616, 2021

- C. Xiao, **F.-C. Hsia**, A. Sutton-Cook, B. Weber, and S. E. Franklin
  "Polishing of polycrystalline diamond using synergies between chemical and mechanical inputs: A review of mechanisms and processes"
  Carbon, **196**, 29, 2022

- C.-C. Hsu, **F.-C. Hsia**, B. Weber, M. B. de Rooij, D. Bonn, and A. M. Brouwer
  "Local shearing force measurement during frictional sliding using fluorogenic mechanophores"
  J. Phys. Chem. Lett., **13**, 8840, 2022

- L. Peng, **F.-C. Hsia**, S. Woutersen, M. Bonn, B. Weber, and D. Bonn
  "Nonmonotonic friction due to water capillary adhesion and hydrogen bonding at multi-asperity interfaces"
  Physical Review Letters, **129**, 256101, 2022

- C. Xiao, L. Peng, C. Leriche, **F.-C. Hsia**, B. Weber, and S. E. Franklin
  "Capillary adhesion governs the friction behavior of electrochemically corroded polycrystalline diamond"
  Carbon, **205**, 345, 2023

- C.-C. Hsu, L. Peng, **F.-C. Hsia**, B. Weber, D. Bonn and A. M. Brouwer
  "Molecular Probing of the Stress Activation Volume in Vapor Phase Lubricated Friction"
  ACS Applied Materials & Interfaces, **15**, 12603, 2023

Acknowledgements

As I end my PhD journey, I am deeply grateful to all the people who participated along the way with me. During my PhD, all the accomplishments and the results from the thesis could not have been completed without teamwork. I am proud to be the first PhD student in the Contact Dynamics group at ARCNL. It was a special experience to start a project from scratch. Although the starting of this journey was challenging, I am very fortunate and truly thankful to have all the support and suggestions from the members in the groups at ARCNL and UvA. I am also sincerely grateful to have Matthijn Rooij, Stef Janssens, Fred Brouwer, Noushine Shahidzadeh and Roland Bliem to be part of the committee, who took the time to carefully review and thoroughly evaluate this thesis.

First, I would like to give my exceptional thanks to my supervisors Steve Franklin and Bart Weber. Thank you for proving me this fantastic opportunity to study for a PhD at ARCNL. I still remember how excited I was when I received the offer from you. I am also very grateful to have had your guidance and support. Steve, thank you for organizing the project so well that I could mostly focus on my project and have enough resources and constructive input to carry out the project smoothly. Bart, I very much appreciated your daily supervision. Because of your enthusiasm and positivity, I felt very comfortable to step into your office and initiate discussions with you. And especially during COVID, you proposed to hold our weekly meetings at your place and of course it was a very special experience to have a BBQ on your roof as a group outing.

Many interesting experiments and fantastic ideas presented in this thesis started with the collaboration with the research groups at UvA lead by Daniel Bonn and Fred Brouwer. Daniel, thank you for all your advice and splendid ideas and for offering me a chance to conduct experiments in your lab. It was a special experience to work in the university and with colleagues from the UvA groups. Fred, thank you for enthusiastically providing your view and opinion from "another side of the world". It was indeed a precious opportunity to involve you in our project discussions.

Fiona, I couldn't express how grateful I am to have you beside me through

this journey. We started almost at the same time in the group. At the start of our group/roles, the first biggest challenge was to make the vacuum UMT work properly. Although it was a painful and annoying period that we spent so much time in the lab to figure out why there was always a leak and contamination in the vacuum chamber, nicely, we solved it after 3 years. Our conference trip to Chicago was amazing. There was a lot of nice memories that we prepared the presentation for the STLE conference together, and had a city tour and watched NBA game at the United Center. I really enjoyed working with you, so many interesting discussions were happening in the office and indeed we are to continue our friendship at ASML.

Görsel, Victor, Cristina, and Ale T., my office mates at ARCNL and lunch mates at CWI. Görsel thank you for sharing your cactus with me. I believe that after my daily "training", your cactus will not sting you anymore. You always brought a chill, funny and positive attitude to the office although nothing was going well with your setup. Victor, you represent another extreme in the office. Every time I heard someone was collapsing and screaming in the lab it was most likely to be you. You always reminded me that no matter how difficult my PhD is, Victor is the one still fighting in the lab. Cristina, I feel happy to have had you in the office. I did enjoy seeing your chats with Görsel when both of you had different opinions, mostly your discussions were quite interesting. Ale T., you are a warm guy. You always listened to my complaints and supported my ultimate plan on gaining weight!

Arend-Jan, our lab started from scratch almost two times, your technical support with setting up the lab was essential. I couldn't imagine how difficult it would have been without your help. You joined our entire journey of fixing the vacuum UMT. I am very appreciative to have had your guidance on solving vacuum issues and you never hesitated to offer your expertise.

Camila, Zazo, and Daan, we worked closely together during your internships. From you, I learned how to cooperate different thoughts and was inspired by you a lot. Camila, you were literally the first internship student in our group. I am glad to have had you in the team. At the beginning we had no idea how to carry out a vacuum test by using UMT, we tried really hard to setup a first trial of vacuum experiments together. Zazo, you were always enthusiastic to offer your help. I very much appreciated you to spend quite some time on developing a script to calculate the frictional force from AFM measurements. And of course, the Dutch version of the Summary chapter is translated by you and your AI friend. Special thanks go to you. Another special thanks go to Daan, your internship project brought non-trivial impact to the research work shown in this thesis. We widely adopted the method of introducing vapors that was demonstrated in your master's thesis.

Living in Amsterdam to have many friends around was always fun and exciting. Randy and Meisei, thank you for inviting me to celebrate my first Lunar New year in Netherlands and introduced me to the famous fancy restaurant–FuLu Mandarijn–in the city center. Neha and Najmeh, my nice neighbors in the green building. Ruben and Ale A., thank you for taking us for the long ride to Austria. Our ski trip was amazing. Ale A., I hope we will have another chance to practice snowboarding again. Maybe next time we should not learn how to snowboard from YouTube on the top of the mountain, and I promise you that I will not lose my snowboard again! Anna, John, Stephen and colleagues at ARCNL, nice to have you for most of the interesting activities in Amsterdam. Ching-Chung (Chris), nice to meet you and your wife when you visited ARCNL, and to show me a chance back to Leuven again.

To my colleagues at UvA, Rinse, Chao-Chun, Hans, Kasra, and Paul, I feel happy to have worked with you in the lab and to have had our coffee chats together. Because of your company, I felt that I was part of the group there. Especially, you helped me a lot to search for one of the missing pieces from the tool in the lab.

I feel grateful to have the guidance from Torbjörn Nordling, Umberto Celano and Dai-Ming Tang, who inspired me to step on this amazing but bumpy PhD journey. Lennaert, Marco, Yu-Ting (Fish), Chia-Tsen (Jason), Jun-Fu, and Ting-Chun (Kevin), thank you for always being around me in Amsterdam, Leuven, and Taiwan where we had nice moments together.

Chen Li, I couldn't imagine my PhD journey without you. You helped me to start my life in Amsterdam. You were always there during my master's internship and we supported each other to accomplish our PhD.

Last but not least, I would like to thank my parents, my grandmom, my brothers, and all my family for their unconditional support, everlasting interest and love from Taiwan.